

# Systematic Evaluation of Single-Cell Foundation Model Interpretability Reveals Attention Captures Co-Expression Rather Than Unique Regulatory Signal

Ihor Kendiukhov

Department of Computer Science

University of Tübingen

Tübingen, Germany

kendiukhov@gmail.com

## Abstract

We present a systematic evaluation framework—thirty-seven analyses, 153 statistical tests, four cell types, two perturbation modalities—for assessing mechanistic interpretability in single-cell foundation models. Applying this framework to scGPT and Geneformer, we find that attention patterns encode structured biological information with layer-specific organisation—protein–protein interactions in early layers, transcriptional regulation in late layers—but this structure provides no incremental value for perturbation prediction: trivial gene-level baselines outperform both attention and correlation edges (AUROC 0.81–0.88 versus 0.70), pairwise edge scores add zero predictive contribution, and causal ablation of regulatory heads produces no degradation. These findings generalise from K562 to RPE1 cells; the attention–correlation relationship is context-dependent, but gene-level dominance is universal. Cell-State Stratified Interpretability (CSSI) addresses an attention-specific scaling failure, improving GRN recovery up to 1.85 $\times$ . The framework establishes reusable quality-control standards for the field.

## 1 Introduction

The emergence of transformer-based foundation models for single-cell transcriptomics represents a paradigm shift in computational biology [Cui et al., 2024, Theodoris et al., 2023, Yang et al., 2022, Hao et al., 2024]. These models—trained on millions of cells across diverse tissues—learn contextual representations that have shown promise for cell type annotation, perturbation response prediction, and gene regulatory network (GRN) inference [Chen et al., 2024, Rosen et al., 2024]. A particularly compelling promise is *mechanistic interpretability*: extracting biologically meaningful regulatory circuits directly from attention-derived edge scores. Both scGPT [Cui et al., 2024] and Geneformer [Theodoris et al., 2023] highlight attention-derived gene network inference as a key application, and downstream studies have adopted attention-derived edge scores as regulatory proxies without rigorous validation [Zheng et al., 2024].

This promise draws on parallel advances in large language model interpretability, where techniques such as activation patching [Meng et al., 2022, Goldowsky-Dill et al., 2023] and automated circuit discovery [Conmy et al., 2023] have identified computational circuits for well-defined behaviours [Elhage et al., 2021, Olsson et al., 2022, Wang et al., 2022]. However, translating these approaches to biology faces unique challenges. Gene regulatory relationships are context-dependent, combinatorial, and only partially captured in reference databases such as TRRUST [Han et al., 2018] and DoRothEA [Garcia-Alonso et al., 2019], which contain a fraction of true regulatory interactions [Pratapa et al., 2020].

Current practices in single-cell foundation model interpretability rest on several critical and largely untested assumptions. *First*, that attention patterns directly reflect causal regulatory relationships—an assumption already challenged in the NLP literature [Jain and Wallace, 2019, Serrano and Smith, 2019, Bibal et al., 2022]. *Second*, that larger datasets consistently improve the reliability of mechanistic interpretations. *Third*, that attention-derived predictions align with experimental perturbation outcomes from CRISPR screens [Dixit et al., 2016]. *Fourth*, that mechanistic insights transfer reliably across biological

contexts. We address these through a two-tier evaluation framework. The *core tier* directly evaluates foundation model internal representations—attention weights, intervention effects, and perturbation-outcome prediction—and proposes Cell-State Stratified Interpretability (CSSI) as a constructive method. The *boundary condition tier* uses correlation-based edge scores to establish limits that any edge-scoring method must contend with, including cross-species transfer, pseudotime directionality, technical leakage, and uncertainty calibration (Supplementary Notes 7–10).

Prior benchmarks have evaluated GRN inference methods [Pratapa et al., 2020] and individual foundation model capabilities [Zheng et al., 2024], but none has systematically assessed whether attention-derived edge scores add mechanistic information beyond expression statistics, nor tested this with causal interventions. We address this gap with a reusable evaluation framework integrating thirty-seven complementary analyses—including trivial-baseline comparison, conditional incremental-value testing, expression residualisation, propensity-matched benchmarks, and causal ablation with intervention-fidelity diagnostics—across two foundation model architectures (scGPT, Geneformer V2-316M), four cell types (K562, primary T cells, RPE1 retinal epithelial, iPSC neurons), and two perturbation modalities (CRISPRi, CRISPRa), with 153 statistical tests under Benjamini-Hochberg FDR correction (Supplementary Table 1; Supplementary Note 16). The framework yields three principal findings. First, attention patterns encode layer-specific biological structure—protein–protein interactions in early layers, transcriptional regulation in late layers (Supplementary Note 17)—but this information provides no incremental value for perturbation prediction: trivial gene-level baselines outperform both attention and correlation edges, pairwise edge scores add zero predictive contribution, and causal ablation of “regulatory” heads produces no behavioural effect. Second, the attention–correlation relationship is context-dependent across cell types, but the underlying confound pattern—gene-level features dominate—generalises. Third, CSSI addresses an attention-specific scaling failure through cell-state stratification, providing an immediately deployable constructive tool. The framework itself—its battery of tests, controls, and diagnostic checks—constitutes a reusable quality-control standard for evaluating mechanistic interpretability claims in single-cell foundation models.

## 2 Results

### 2.1 Evaluation framework

We designed an evaluation framework comprising five interlocking test families (Figure 1–6; Supplementary Notes 1–16). (i) *Trivial-baseline comparison* tests whether pairwise edge scores outperform univariate gene-level features (variance, mean expression, dropout rate) that require no model. (ii) *Conditional incremental-value testing* asks whether adding edge scores to gene-level features improves prediction under progressively harder generalisation protocols (cross-perturbation, cross-gene, and joint splits) with linear and nonlinear models. (iii) *Expression residualisation and propensity matching* isolate edge-specific signal by removing gene-level confounds via two complementary statistical approaches. (iv) *Causal ablation with fidelity diagnostics* uses head masking, uniform attention replacement, and MLP ablation to test whether “regulatory” heads causally contribute to perturbation prediction, with checks confirming that interventions materially perturb representations. (v) *Cross-context replication* tests whether findings generalise across cell types (K562, RPE1, T cells, iPSC neurons) and perturbation modalities (CRISPRi, CRISPRa). Each family addresses a distinct confound; their convergence provides stronger evidence than any individual test. A boundary-condition tier (cross-species transfer, pseudotime, batch leakage, calibration; Supplementary Notes 7–10) characterises the broader evaluation landscape. Together, these yield thirty-seven analyses with 153 statistical tests under Benjamini-Hochberg FDR correction.

### 2.2 Attention-specific scaling failure and CSSI remedy

To test whether increasing dataset size improves interpretability, we analysed archived scGPT kidney scaling runs across three model tiers (small/medium/large), three seeds per tier, and three cell counts (200, 1,000, 3,000). Top- $K$  F1 for attention-derived GRN recovery against TRRUST [Han et al., 2018] degrades with cell count—the 200→1,000 drop is negative in all 9 tier×seed runs (sign test  $p = 0.002$ ; Extended Data Fig. 1; Supplementary Note 1), with a continued trend at 1,000→3,000 (7/9 runs,  $p = 0.09$ ). This finding is metric-dependent: continuous-score AUROC (no top- $K$  thresholding) improves monotonically (0.86 → 0.93; 0/9

### CSSI Mitigates Scaling Failure

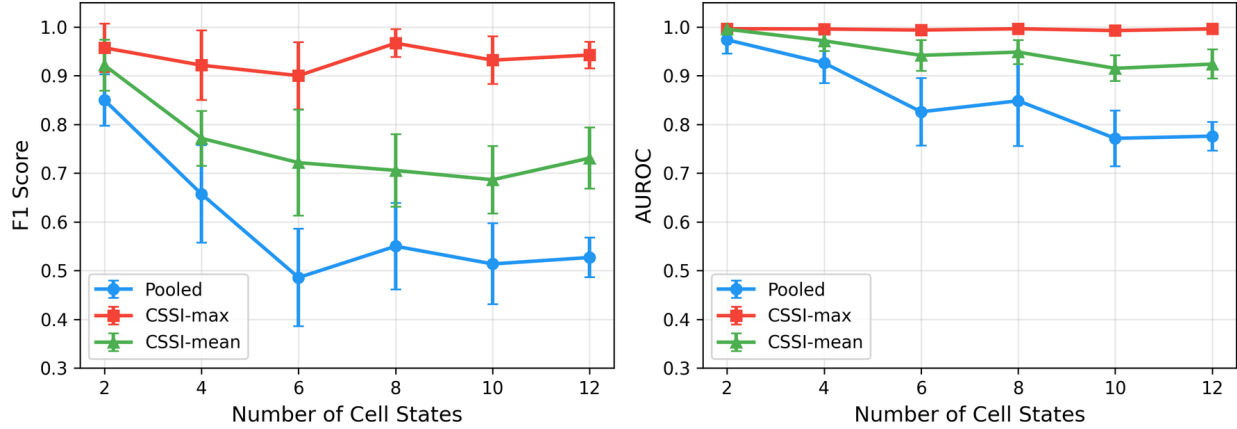


Figure 1: **CSSI improves attention-derived GRN recovery.** CSSI-max TRRUST F1 versus number of strata ( $K$ ) on DLPFC brain data. Stratified scoring improves recovery up to  $1.85\times$  over unstratified baselines, with optimal  $K = 5\text{--}7$ .

degrading), qualifying the original observation. Controlled-composition experiments using correlation-based edges on Tabula Sapiens kidney data (Extended Data Fig. 1) disentangle sample size from heterogeneity: with fixed composition AUROC is stable ( $\rho = -0.05$ ,  $p = 0.82$ ), and heterogeneity at fixed  $N$  actually *improves* recovery ( $\rho_{\text{heterogeneity}} = +0.63$ ,  $p = 10^{-4}$ ), confirming that the degradation is attention-specific rather than inherent to edge scoring.

As a constructive contribution, we introduce Cell-State Stratified Interpretability (CSSI), motivated by a formal dilution model predicting that pooled attention-derived edge scores degrade as  $\rho_{\text{pool}} \approx (n_1/N)\rho_1 \rightarrow 0$  with increasing heterogeneity. CSSI computes edge scores within cell-state strata (Leiden clustering on  $k$ -NN graphs from model embeddings) before aggregation, controlling the heterogeneity that drives attention-specific dilution. On DLPFC brain scRNA-seq data, CSSI-max improves top- $K$  TRRUST recovery up to  $1.85\times$  (Figure 1), with the optimum at intermediate  $K$  (5–7 strata). Extended null tests across  $K \in \{2, \dots, 20\}$  confirm no false-positive inflation under uninformative (random) strata, ensuring CSSI improvements reflect genuine signal recovery. Real-data layer/head analysis reveals recoverable reference-edge signal concentrated in late Geneformer layers (L13 AUROC = 0.694; Supplementary Note 11), and cell-level bootstrap analysis shows that 7/18 individual TFs have robust edge-level signal (global AUROC 95% CI: [0.71, 0.77]). Synthetic validation with known ground-truth networks corroborates these findings (Supplementary Note 12). Multi-model analysis shows convergent near-random unstratified performance across both scGPT and Geneformer (Extended Data Fig. 2; Supplementary Note 13)—despite fundamentally different architectures (gene-token vs. rank-based tokenisation), training objectives, and model scales—confirming the failure is architecture-independent and reflecting a persistent limitation of unstratified approaches to attention-derived GRN inference.

### 2.3 Perturbation-first validation reveals gene-level dominance

We evaluated whether edge scores predict perturbation outcomes using the Replogle genome-scale CRISPRi dataset [Replogle et al., 2022] ( $>640,000$  K562 cells, 2,024 perturbed genes). For each CRISPRi perturbation, we computed edge scores between the perturbed gene and all other genes, then evaluated AUROC for classifying differentially expressed targets. Correlation-based edges achieve AUROC = 0.696 under the primary parameterisation ( $N_{\text{ctrl}} = 2,000$ , HVG = 2,000, LFC  $> 0.5$ ;  $n = 151$  perturbations), with all 27 sensitivity conditions (varying control cell count, HVG count, and LFC threshold) yielding AUROC = 0.62–0.76 (all  $p < 0.005$ ; Extended Data Fig. 7; Supplementary Note 6), indicating robust predictive signal for co-expression edges.

Direct evaluation of Geneformer V2-316M attention-derived edges under the same parameterisation yields

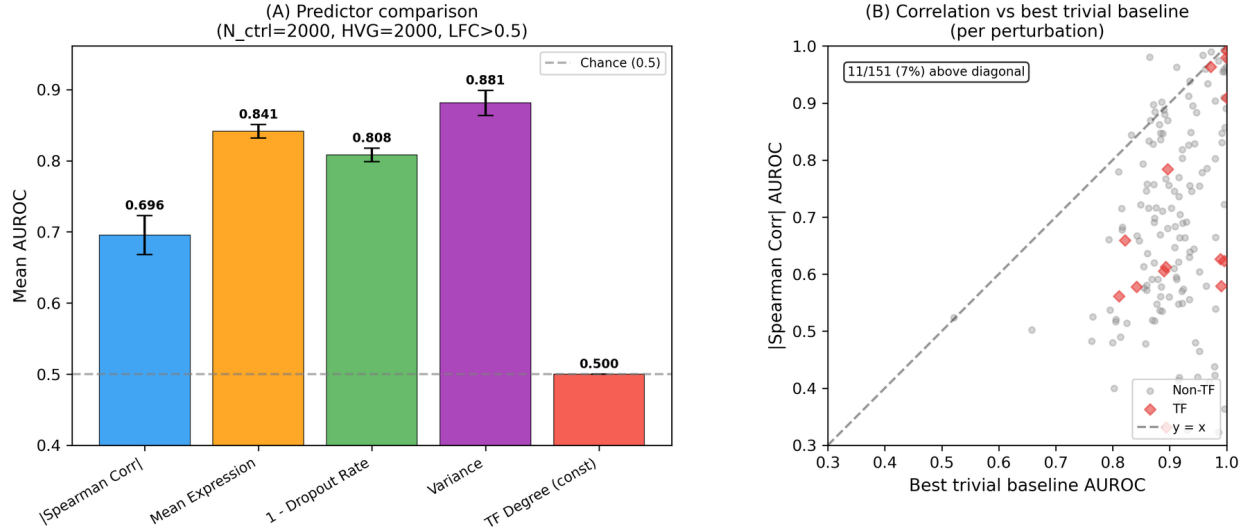


Figure 2: **Gene-level baselines outperform pairwise edge scores.** AUROC for predicting CRISPRi perturbation targets using gene-level features (variance, mean expression, dropout rate) versus correlation-based edge scores ( $n = 151$  perturbations; attention comparison in text). All gene-level baselines significantly outperform both edge types ( $p < 10^{-12}$ ).

AUROC = 0.704 at L13 ( $n = 280$  evaluable perturbations), statistically indistinguishable from correlation (0.703; Wilcoxon  $p = 0.73$ ; Extended Data Fig. 3). L13 was pre-specified as the primary layer based on independent data: the CSSI analysis on DLPFC brain tissue (497 cells; Supplementary Note 11) identified L13 as the best-performing layer for TRRUST recovery (AUROC = 0.694), *before* any K562 perturbation data were examined. The fact that attention edges—which reflect learned cross-gene interactions across 30 million training cells—perform no better than simple Spearman correlation computed on a single dataset is a striking negative result, suggesting that Geneformer’s pretraining does not embed recoverable regulatory structure into its attention patterns. As a planned secondary analysis, the full 18-layer perturbation-first profile reveals a clear architectural gradient: early layers achieve AUROC 0.47–0.64, mid layers 0.60–0.71, and late layers 0.69–0.74. A strict nested cross-validation protocol—designed to guard against overfitting across 18 candidate layers—identifies L15 as the best layer (AUROC = 0.743,  $p_{\text{Bonf}} = 0.017$ ,  $d = 0.22$ ; Extended Data Fig. 5), but this advantage is small (only 161/280 perturbations favour attention) and reverses entirely in CRISPRa ( $d = -0.56$ ,  $p = 4.9 \times 10^{-5}$ ), establishing it as K562-CRISPRi-specific rather than a general property of the model.

Critically, trivial gene-level baselines—variance, mean expression, and dropout rate—all outperform both attention and correlation edges (AUROC 0.81–0.88 vs. 0.70; all  $p < 10^{-12}$ ; Figure 2). Variance alone achieves AUROC = 0.881—substantially exceeding the best attention layer—indicating that much of the perturbation-predictive signal reflects univariate gene properties rather than pairwise regulatory structure. We note that predicting interventional outcomes (differential expression after knockdown) is distinct from identifying direct causal regulatory edges; our perturbation-first evaluation captures the former. Nevertheless, the dominance of gene-level baselines challenges the assumption that pairwise edge scores capture regulatory information beyond what simple gene statistics provide, and establishes a necessary (though not sufficient) baseline for any claimed pairwise regulatory signal.

## 2.4 No incremental pairwise value from edge scores

A key question is whether pairwise edge scores—attention or correlation—add predictive value *beyond* gene-level features for identifying perturbation targets. We constructed a dataset of  $280 \times 1,999$  perturbation–gene observations (559,720 pairs, 2.8% positive rate) and compared five logistic-regression models under 5-fold GroupKFold cross-validation: gene-level features only (mean expression, variance, dropout rate),

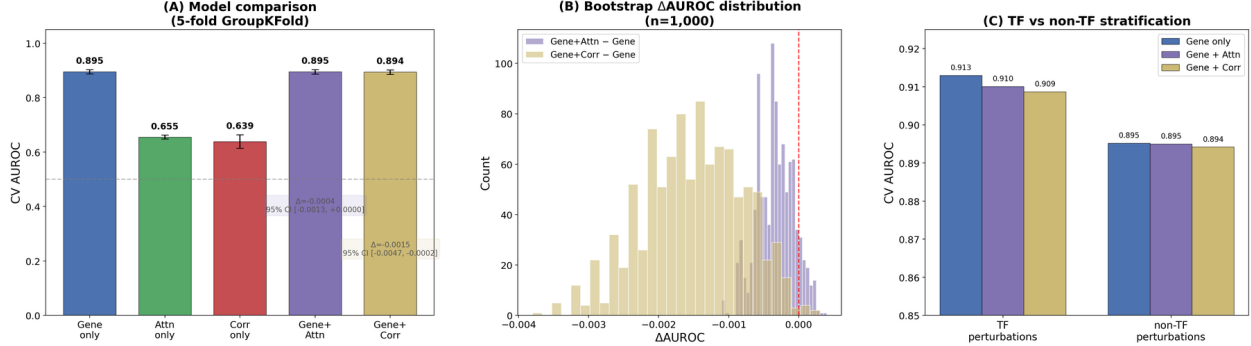


**Figure 3: Pairwise edge scores provide no incremental value beyond gene-level features.** (A) Cross-validated AUROC for five model configurations under GroupKFold by perturbation: gene-level features alone, attention only, correlation only, gene-level plus attention, and gene-level plus correlation. Adding pairwise edges provides no improvement. (B) Bootstrap  $\Delta$ AUROC distribution ( $n = 100$ ) for gene+attention minus gene-only (purple) and gene+correlation minus gene-only (pink); both centred at zero. (C) Stratification by TF versus non-TF perturbation genes shows identical patterns.

attention edge only, correlation edge only, gene-level plus attention, and gene-level plus correlation. Gene-level features alone achieve AUROC = 0.895 [bootstrap 95% CI: 0.884, 0.905]; adding attention yields  $\Delta$ AUROC =  $-0.0004$  [ $-0.001$ ,  $0.000$ ] and adding correlation yields  $\Delta$ AUROC =  $-0.002$  [ $-0.005$ ,  $0.000$ ] (Figure 3). Neither pairwise edge type provides incremental value, and this is not a power issue: 559,720 observations provide  $>99\%$  power to detect  $\Delta$ AUROC = 0.005.

To rule out that this null result reflects a specific analytical choice, we tested progressively harder generalisation protocols—cross-gene splits (GroupKFold by target gene, preventing gene-level propensity leakage), joint cross-gene  $\times$  cross-perturbation splits—and both linear (logistic regression) and nonlinear (GBDT) models across AUROC, AUPRC, and top- $k$  recall. Under all tested combinations, the null persists: even the largest observed  $\Delta$ AUPRC (+0.009 under joint splits with GBDT) represents less than 4% relative improvement (Extended Data Fig. 6; Supplementary Note 15).

Cross-fitted residualisation reveals an important asymmetry: on K562 data, attention edges lose  $\sim 76\%$  of their above-chance TRRUST signal under expression-covariate residualisation (AUROC 0.66  $\rightarrow$  0.54; OLS  $R^2 = 0.03$ , GBDT  $R^2 = 0.23$ ), while correlation edges retain  $\sim 91\%$  ( $0.63 \rightarrow 0.62$ ; Extended Data Fig. 4), indicating that attention-derived regulatory signal is substantially more expression-confounded. Degree-preserving null models show that much of the global AUROC reflects TF degree structure (degree-null AUROC 0.69 vs. observed 0.76; Supplementary Note 14). A propensity-matched benchmark provides a direct test: after matching each DE-positive target to  $k = 5$  DE-negative targets with similar expression mean, variance, and dropout rate via propensity-score nearest-neighbour matching ( $n_{\text{matched}} = 59,153$  pairs; positive rate 26.5% vs. 2.8% before matching), attention edges retain modest raw discriminability (AUROC = 0.609) but add zero incremental value over gene-level features ( $\Delta$ AUROC =  $-0.000$ ; 95% CI:  $[-0.000, +0.000]$ ; Extended Data Fig. 8).

## 2.5 Causal ablation reveals distributed redundancy

The preceding analyses are observational. To provide causal evidence, we used BERT’s head-mask parameter to zero out specific attention heads during Geneformer V2-316M’s forward pass and measured the effect on perturbation-first AUROC (2,000 K562 control cells, 280 perturbations per condition). We ranked all 324 heads ( $18 \times 18$ ) by TRRUST-recovery AUROC and tested 13 ablation conditions spanning dose-response, alternative rankings, full-layer ablation, inverse controls, and matched random controls (Figure 4). The dose-response curve is unambiguous: ablating the top-5 ( $0.704$ ,  $p = 0.24$ ), top-10 ( $0.704$ ,  $p = 0.94$ ), top-20 ( $0.703$ ,  $p = 0.60$ ), or top-50 TRRUST-ranked heads ( $0.701$ ,  $p = 0.10$ ; 15% of all heads) produces no significant degradation from baseline ( $0.704$ ). By contrast, ablating 20 random heads causes a significant drop ( $0.697$ ,  $d = 0.33$ ,  $p < 10^{-8}$ ), demonstrating that “regulatory” heads are *less* causally important than random heads. An alternative ranking by composite score (TRRUST AUROC  $\times$  layer perturbation-first AUROC) yields

identical results. Ablating all 18 heads in L14 (the best perturbation-first layer) produces exactly baseline AUROC, and ablating the bottom-5 heads actually *improves* performance (0.706,  $p = 0.005$ ).

Two families of orthogonal interventions corroborate this null: uniform attention replacement (destroying attention patterns while preserving head output magnitude) on TRRUST-ranked heads has no effect (top-5: 0.704, top-10: 0.703), and MLP pathway ablation (zeroing FFN output) at L15 and L13–L15 both produce exactly 0.704 (Extended Data Fig. 9). Intervention-fidelity diagnostics confirm that all six interventions materially perturb internal representations (max hidden-state cosine distance 0.023–0.190), with TRRUST-ranked heads producing 23 $\times$  larger logit perturbation than random heads at matched dose (Extended Data Fig. 9; Supplementary Note 14), ruling out the possibility that behavioral nulls reflect ineffective interventions. The convergence of null results across three qualitatively different intervention channels—head masking, attention pattern destruction, and MLP ablation—provides substantially stronger evidence than single-method ablation alone and makes it unlikely that concentrated regulatory signal exists in any head subset. This distributed-redundancy pattern contrasts sharply with NLP findings where specific attention heads encode identifiable syntactic or semantic functions [Voita et al., 2019, Clark et al., 2019]; in single-cell models, perturbation-predictive computation appears to reside in the value/FFN pathway rather than in learnable attention patterns. Per-head ranking across all 324 heads shows substantial variation in TRRUST recovery (top-5 AUROC = 0.70–0.75 vs. population mean =  $0.58 \pm 0.07$ ), yet this variation does not translate to causal importance for perturbation prediction, consistent with the signal being distributed across the entire network rather than concentrated in identifiable “regulatory circuits.”

## 2.6 Context-dependent attention–correlation relationship

Cross-context replication across four cell types and two perturbation modalities reveals that the attention–correlation relationship is genuinely context-dependent. On K562 CRISPRi ( $n = 280$ ), Geneformer V2-316M attention and Spearman correlation are statistically indistinguishable (L13: 0.704 vs. 0.703,  $p = 0.73$ ). On K562 CRISPRa [Adamson et al., 2016] ( $n = 77$ ), attention significantly *underperforms* correlation (AUROC 0.55 vs. 0.65;  $p < 10^{-6}$ ), with correlation outperforming attention in 55–63 of 77 perturbations. However, the first adequately powered non-K562 replication tells a qualitatively different story: on RPE1 retinal epithelial cells [Replogle et al., 2022] ( $n = 1,251$  evaluable perturbations; minimum detectable  $d = 0.079$ ), attention significantly *outperforms* correlation at all layers (L15: 0.748 vs. 0.658,  $d = 0.47$ ,  $p < 10^{-10}$ ; L6: 0.776,  $d = 0.74$ ; Figure 5). The advantage strengthens under stringent DE thresholds (LFC  $> 0.5$ : +0.090; LFC  $> 0.25$ : +0.049). iPSC-derived neurons ( $n = 7$ ) trend in the same direction ( $d = 0.80$ ,  $p = 0.078$ ), while primary T cells [Shifrut et al., 2018] ( $n = 7$ ) show no difference ( $p = 0.81$ ; Supplementary Note 14). A methodological asymmetry—RPE1 includes perturbation genes forced into the HVG set (3,309 vs. 2,000 genes in K562)—could confound this comparison, but restricting RPE1 to the top 2,000 HVGs (matching K562 protocol) *increases* the attention advantage ( $\Delta = +0.168$ ,  $n = 418$ ;  $p < 10^{-46}$ ), as correlation degrades more than attention when the evaluation universe shrinks. Bootstrap 95% CIs on the per-perturbation attention advantage exclude zero for both K562 ( $\Delta = +0.060$  [ $+0.040$ ,  $+0.080$ ]) and RPE1 ( $\Delta = +0.090$  [ $+0.079$ ,  $+0.101$ ]; Supplementary Note 14). The cross-context pattern—equal in K562 CRISPRi, worse in CRISPRa, better in RPE1, and trending better in neurons—indicates that the attention–correlation relationship depends on cell type and perturbation modality rather than reflecting a universal architectural limitation or advantage. This context-dependence may arise from cell-type-specific regulatory architectures, differences in perturbation effect sizes, or variation in the relationship between expression rank (Geneformer’s input) and regulatory importance across cell types.

## 2.7 Cross-cell-type generalisation of confound pattern

To test whether the RPE1 attention advantage reflects genuine regulatory signal or gene-level confounds, we applied the full K562 confound-decomposition battery to the RPE1 dataset ( $n = 1,167$  evaluated perturbations, 3,838,263 gene-pair observations; Figure 6). Five analyses converge on the same conclusion as K562. (i) Trivial baselines outperform both edge types (variance AUROC = 0.866, mean expression = 0.851, dropout = 0.797 vs. attention = 0.747 and correlation = 0.658; all paired  $p < 10^{-38}$ ). (ii) Gene-level features alone achieve AUROC = 0.942 under 5-fold GroupKFold CV; adding attention yields  $\Delta$ AUROC = +0.0001 [95% CI: +0.0001, +0.0001]—functionally zero—while adding correlation yields  $\Delta$ AUROC = −0.0006.

- (iii) Propensity-matched edges drop to near chance (attention = 0.568, correlation = 0.561) with LR incremental value exactly zero.
- (iv) GBDT residualisation removes  $\sim$ 88% of attention’s above-chance signal (AUROC 0.722  $\rightarrow$  0.527) while correlation signal *increases* (0.656  $\rightarrow$  0.692), indicating a suppressor effect.
- (v) TRRUST direct-target prediction is near chance ( $n = 54$  evaluable TFs; attention =  $0.559 \pm 0.250$ , correlation =  $0.540 \pm 0.233$ ).

Together, these five analyses establish that the RPE1 attention advantage over correlation (diff = +0.089,  $p < 10^{-10}$ ) does not reflect attention capturing regulatory structure that correlation misses; rather, attention is a better proxy for the gene-level features that dominate perturbation prediction. The RPE1 gene-only AUROC (0.942) exceeds the K562 value (0.895), consistent with RPE1’s larger gene universe (3,290 vs. 2,000 genes) providing richer gene-level features. The confound-decomposition conclusion—pairwise edge scores carry no incremental information beyond univariate gene properties—generalises across both cell types, establishing this as a robust finding rather than a K562-specific artifact.

### 3 Discussion

Our results reveal that attention patterns in scGPT and Geneformer encode structured biological information—but not the causal regulatory signal they are routinely interpreted as capturing. This conclusion rests on convergent evidence: expression residualisation, degree-preserving null models, incremental-value testing under three generalisation protocols, and causal ablation (head masking, attention replacement, MLP ablation) all indicate that pairwise edge scores carry no regulatory information beyond gene-level features, and that heads identified as “regulatory” make no causal contribution to perturbation prediction.

The attention–correlation relationship is genuinely context-dependent: K562 CRISPRi (equal), K562 CRISPRa (attention worse), RPE1 (attention better), T cells and iPSC neurons (trending directions but underpowered). However, this context-dependence is superficial with respect to regulatory inference. In both K562 and RPE1, the full confound-decomposition battery reveals the same underlying pattern: gene-level features dominate perturbation prediction (AUROC 0.895–0.942), and pairwise edge scores add zero incremental value. The RPE1 attention advantage reflects attention being a better proxy for gene-level confounds—not attention capturing regulatory structure that correlation misses. This distinction is practically important: raw performance comparisons between edge-scoring methods are misleading without confound controls, and we recommend that such controls become standard practice.

These findings extend the attention-as-explanation debate from NLP [Jain and Wallace, 2019, Wiegrefe and Pinter, 2019, Bibal et al., 2022] to biological foundation models. In language models, attention weights do not reliably indicate feature importance [Serrano and Smith, 2019]; our results demonstrate an analogous limitation in single-cell models, where attention-derived edge scores fail to capture causal regulatory relationships. The multi-model convergence (scGPT and Geneformer achieve similar near-random unstratified performance despite different architectures, training objectives, and tokenisation; Supplementary Note 13) suggests this reflects the optimisation landscape rather than a model-specific limitation: pretraining objectives reward co-expression patterns, not causal structure. Biological characterization against multiple reference databases (Supplementary Note 17) reveals additional structure: early layers preferentially capture protein–protein interactions (STRING [Szklarczyk et al., 2021] AUROC = 0.64 at L0; decreasing with depth,  $\rho = -0.61$ ,  $q_{BH} = 0.01$ ), while late layers encode transcriptional regulation (TRRUST AUROC = 0.75 at L15;  $\rho = +0.51$ ,  $q_{BH} = 0.03$ ), with anti-correlated layer profiles ( $\rho = -0.55$ ,  $p = 0.019$ ). This hierarchy is real and survives expression residualisation (97% of TRRUST signal retained), but none of these signals—PPI, regulatory, or functional—provides incremental value for perturbation prediction beyond gene-level features.

Crucially, these findings characterise specific model components—attention weights, individual heads, and MLP blocks at particular layers—not the full model’s predictive capacity. Transformer-based foundation models integrate information through residual streams, layer normalisations, and feed-forward networks that collectively contain far more parameters than attention alone. A model can be a capable black-box predictor even when its attention patterns do not serve as interpretable readouts of causal regulation. The value of systematic component-level evaluation is not to establish fundamental limits of these architectures, but to narrow the search for where biologically meaningful representations reside: by ruling out attention as the locus of regulatory encoding, future interpretability work can focus on residual-stream geometry, MLP-stored knowledge, or representations that emerge only from the full forward pass. This is the core purpose

of mechanistic interpretability applied to biological foundation models—a progressive mapping of internal representations to biological function.

CSSI provides a constructive contribution by controlling the heterogeneity that drives attention-specific dilution, with null-control tests confirming genuine improvements (Supplementary Note 11). However, CSSI addresses edge recoverability against curated references, not the gap with perturbation-outcome predictive validity.

Several limitations constrain interpretation. Causal ablation uses only Geneformer V2-316M; scGPT’s autoregressive architecture lacks a head-mask interface. Perturbation data span four cell types and two modalities, but additional tissues, species, and architectures (scFoundation [Hao et al., 2024]) remain untested. No decisive positive control demonstrates that the pipeline can recover known causal regulatory structure in a realistic perturbation setting, so negative results could in principle reflect assay rather than model limitations. However, no such gold-standard causal pairwise method exists at genome scale for any GRN approach, and several internal calibrations mitigate this concern: the pipeline exhibits wide dynamic range (gene-level AUROC 0.88–0.94, so the incremental-value null is specifically about pairwise structure, not endpoint insensitivity); residualisation produces asymmetric results (attention loses 76% of signal vs. 9% for correlation), distinguishing differently confounded scores; the per-TF bootstrap detects above-chance pairwise signal in 7/18 TFs (Supplementary Note 14); and the pipeline detects real cross-context differences (CRISPRa reversal,  $RPE1 \neq K562$ ), ruling out a floor effect. These calibrations establish sensitivity to pairwise signal variation, even though the definitive positive control remains an open challenge for the field. Reference database circularity affects all GRN evaluation; however, restricting TRRUST to direction-known entries (Activation/Repression; 58% of pairs), which require direct experimental evidence, yields virtually identical per-TF AUROC (mean 0.682 vs. 0.692; median improves to 0.695; Supplementary Note 14), confirming conclusions are not driven by circularly validated entries. Boundary-condition analyses (Supplementary Notes 7–10) use correlation-based edges and characterise the evaluation landscape broadly.

We recommend that practitioners: (i) apply trivial-baseline and incremental-value tests before claiming pairwise regulatory signal; (ii) report both thresholded (top- $K$ ) and continuous (AUROC) metrics; (iii) apply CSSI or equivalent stratification for heterogeneous populations; and (iv) validate causal claims with ablation controls accompanied by intervention-fidelity diagnostics. Three directions are most promising: intervention-aware pretraining on perturbation data [Replogle et al., 2022] could embed causal rather than correlational structure; hybrid architectures using foundation model embeddings as inputs to GRN inference modules could combine representational power with regulatory inductive biases; and CSSI-enhanced pipelines with conformal prediction sets [Vovk et al., 2005] provide an immediately deployable framework. The gap between recoverability and perturbation-outcome predictive validity remains the central challenge.

## 4 Methods

### 4.1 Models and data

We analyse scGPT [Cui et al., 2024] and Geneformer [Theodoris et al., 2023]: scGPT uses gene-token transformers with attention-derived edge scores extracted from all layers/heads; Geneformer uses BERT-style rank-based tokenisation. We use Geneformer V1-10M (6 layers, 4 heads) for multi-model comparison and V2-316M (18 layers, 18 heads) for layer-level analysis. Datasets include Tabula Sapiens atlas tissues [The Tabula Sapiens Consortium, 2022] (immune, kidney, lung), DLPFC brain scRNA-seq [Maynard et al., 2021], Replogle genome-scale CRISPRi [Replogle et al., 2022] (K562 and RPE1), Adamson CRISPRa [Adamson et al., 2016], Shifrut T-cell CRISPRi [Shifrut et al., 2018], and Tian iPSC neurons. Preprocessing follows standard Scanpy quality control [Wolf et al., 2018].

### 4.2 Scaling and CSSI

Scaling behaviour was analysed using archived scGPT kidney runs across three model tiers (small/medium/large), three seeds, and three cell counts (200/1,000/3,000). Controlled-composition experiments used Tabula Sapiens kidney data under three conditions: single cell type with varying  $N$ , mixed types with fixed composition, and fixed  $N$  with increasing heterogeneity. CSSI implements stratified edge scoring by partitioning cells

into  $K$  clusters (Leiden community detection on  $k$ -NN graphs from model embeddings) and computing per-stratum Spearman correlations for each TF-target pair, aggregating via maximum across strata (CSSI-max) or mean (CSSI-mean). Null tests use random cluster labels. Full details in Supplementary Notes 1 and 11.

### 4.3 Perturbation-first validation

For each perturbation  $g$ , we compute attention-derived or correlation-based edge scores between  $g$  and all other genes, then evaluate AUROC for classifying differentially expressed targets (Mann-Whitney  $U$  test, Benjamini-Hochberg correction, LFC threshold). We use  $N_{\text{ctrl}} = 2,000$  control cells, HVG = 2,000 (K562) or 3,309 (RPE1, with perturbation genes forced in). The primary attention layer (L13) was pre-specified based on independent DLPFC brain data (Supplementary Note 11); full 18-layer profiling and nested cross-validation (Extended Data Fig. 5) were planned secondary analyses. Sensitivity analysis spans 27 parameter combinations varying control cell count, HVG count, and LFC threshold (Supplementary Note 6).

### 4.4 Confound decomposition

Gene-level features (mean expression, variance, dropout rate) and pairwise edge scores are used in logistic regression under 5-fold GroupKFold cross-validation (grouped by perturbation). We test gene-only, edge-only, and combined models. Hard-generalisation protocols use GroupKFold by target gene and joint cross-gene  $\times$  cross-perturbation splits. Cross-fitted residualisation removes expression-covariate contributions from edge scores using 5-fold OLS and GBDT; residual AUROC quantifies retained TRRUST-predictive signal. Propensity-score matching uses logistic regression on gene-level features to match each DE-positive target to  $k = 5$  DE-negative targets with similar covariate profiles (Supplementary Note 14).

### 4.5 Causal ablation

Head-masking ablation uses Geneformer’s BERT `head_mask` parameter (shape:  $n_{\text{layers}} \times n_{\text{heads}}$ ; `attn_implementation="eager"`) to zero out specific head outputs. We test 13 conditions: top- $k$  TRRUST-ranked ( $k = 5, 10, 20, 50$ ), composite-ranked ( $k = 5, 10$ ), full-layer (L14), inverse (bottom- $k$ ), and random controls. Orthogonal interventions include uniform attention replacement (setting attention weights to  $1/n$  while preserving value projections) and MLP ablation (zeroing FFN output at specific layers). Intervention fidelity is assessed by comparing hidden-state and logit cosine distances between intervened and baseline forward passes across 2,000 cells (Supplementary Note 14).

### 4.6 Statistical framework

All analyses apply Benjamini-Hochberg FDR correction [Benjamini and Hochberg, 1995] at  $\alpha = 0.05$  across 95 confirmatory  $p$ -values framework-wide, of which 63 (66%) remain significant. Sensitivity analysis under three alternative family definitions confirms that all primary conclusions are stable (Supplementary Note 16). Effect sizes use Cohen’s  $d$ ; bootstrap confidence intervals use 200 iterations with perturbation-level resampling.

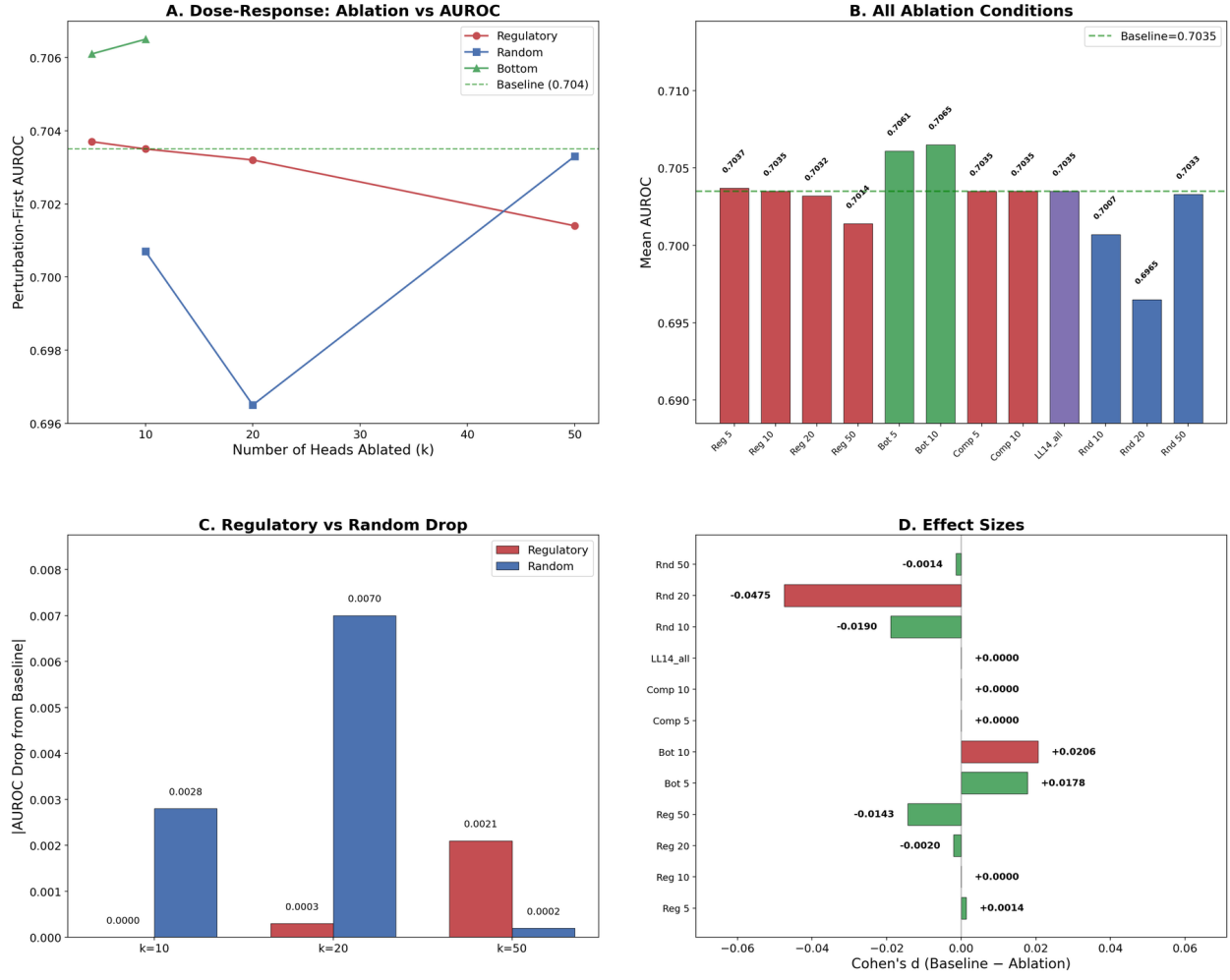
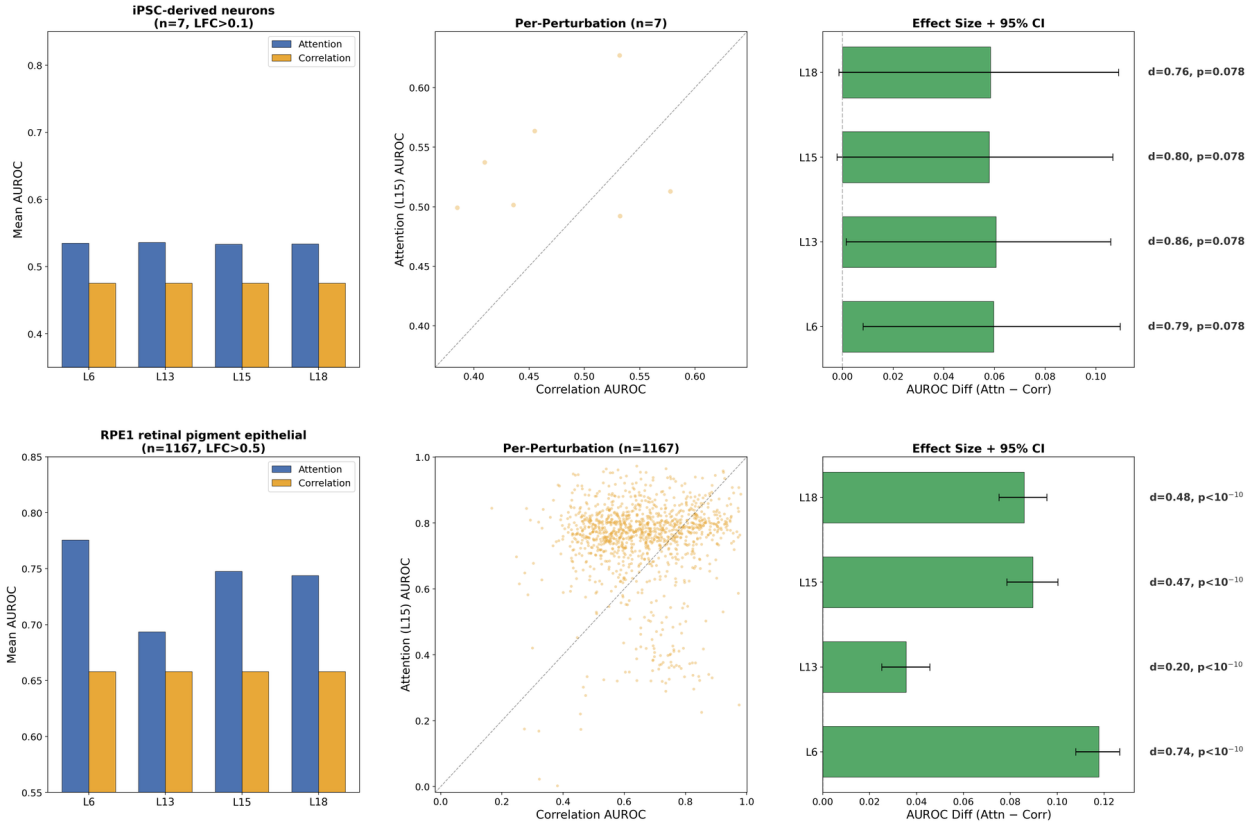


Figure 4: **Causal ablation dose-response.** (A) AUROC versus number of ablated heads for TRRUST-ranked (red), composite-ranked (green), and random (blue) ablation. Regulatory heads can be ablated up to  $k = 50$  with no significant degradation, while random ablation causes significant drops. (B) All ablation conditions: mean AUROC across 13 conditions versus baseline. (C) Regulatory versus random drop magnitude at each dose level  $k$ . (D) Cohen's  $d$  effect sizes (baseline minus ablation) for all conditions; most are indistinguishable from zero.



**Figure 5: Context-dependent attention–correlation relationship.** Perturbation-first AUROC comparison between Geneformer V2-316M attention and Spearman correlation across cell types. In RPE1 ( $n = 1,251$ ), attention significantly outperforms correlation ( $d = 0.47, p < 10^{-10}$ ), contrasting with K562 where they are indistinguishable. Sensitivity to LFC threshold shown for RPE1.

### RPE1 Confound Battery

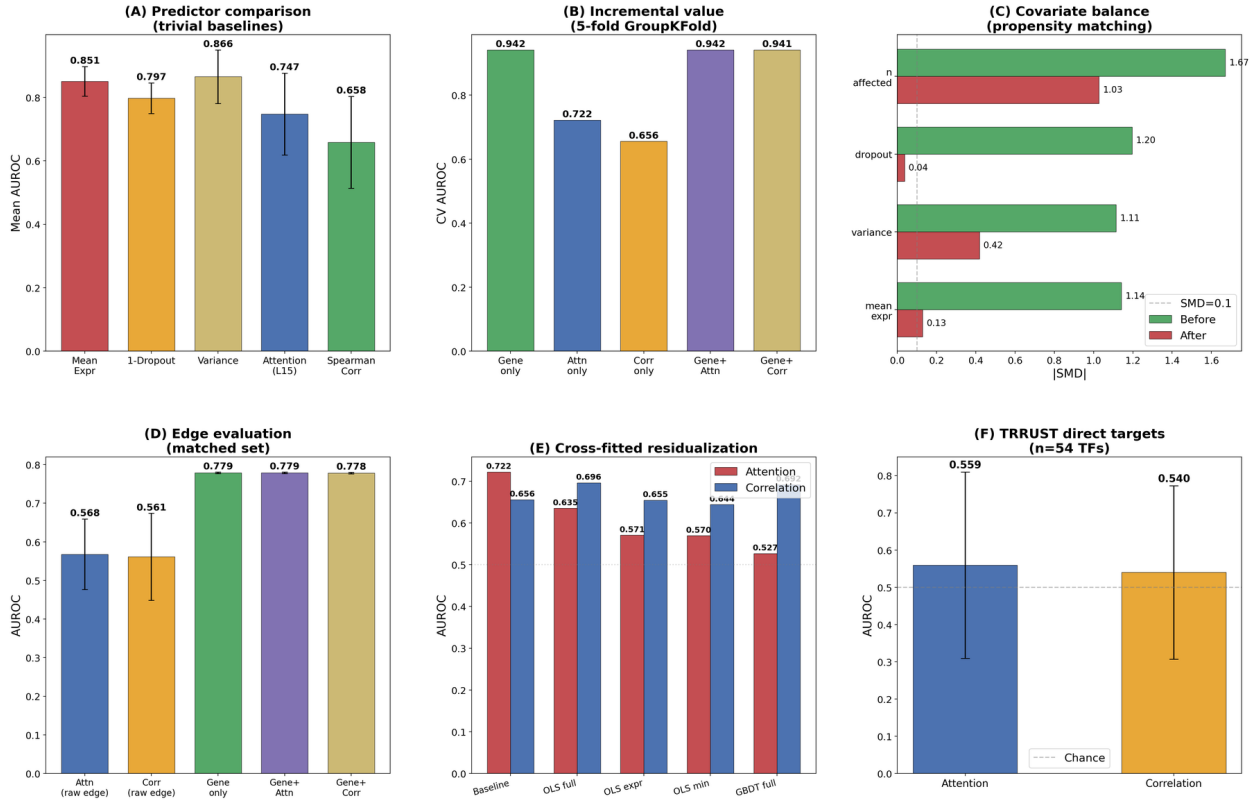


Figure 6: **RPE1 confound battery confirms gene-level dominance.** (A) Trivial baselines outperform both edge types. (B) Gene-only AUROC = 0.942; zero incremental value from edges. (C) Covariate balance after propensity matching. (D) Matched-set evaluation: edges near chance. (E) Residualisation: attention loses  $\sim 88\%$  of signal; correlation increases (suppressor). (F) TRRUST prediction near chance.

## Extended Data

**Extended Data Fig. 1 | Scaling behaviour of attention-derived GRN recovery.** (A–C) Metric-dependent scaling: TRRUST F1 with 95% CIs across three scGPT kidney model tiers and cell counts (200/1,000/3,000). Top- $K$  F1 degrades unanimously (9/9,  $p = 0.002$ ), while continuous AUROC improves monotonically. (D) Controlled-composition: single cell type shows no significant degradation with  $N$ . (E) Fixed composition: stable AUROC. (F) Increasing heterogeneity at fixed  $N$ : AUROC increases, contrasting with attention-based degradation.

**Extended Data Fig. 2 | Multi-model GRN recovery.** Both scGPT and Geneformer achieve near-random unstratified AUROC ( $\approx 0.5$ ) against TRRUST/DoRothEA [Garcia-Alonso et al., 2019], demonstrating architecture-independent limitation. CSSI reveals recoverable signal within individual heads.

**Extended Data Fig. 3 | Attention versus correlation perturbation-first.** Geneformer V2-316M attention AUROC at L13 (0.704) is indistinguishable from correlation (0.703;  $p = 0.73$ ) on  $n = 280$  K562 CRISPRi perturbations. L13 was pre-specified based on independent DLPFC brain data (Supplementary Note 11).

**Extended Data Fig. 4 | Attention-specific confound decomposition.** Cross-fitted residualisation reveals asymmetric expression confounding: attention edges lose  $\sim 76\%$  of TRRUST signal versus  $\sim 9\%$  for correlation. Degree-preserving null models shown for both.

**Extended Data Fig. 5 | Nested layer selection protocol.** 5-fold nested CV independently selects L15 in all folds. Pooled held-out  $\Delta = +0.040$  [0.018, 0.062];  $p_{\text{Bonf}} = 0.017$ . CRISPRa replication reverses the effect ( $d = -0.56$ ).

**Extended Data Fig. 6 | Hard-generalisation incremental-value testing.** No incremental value under cross-gene, cross-perturbation, or joint splits, for both LR and GBDT, across AUROC, AUPRC, and top- $k$  recall.

**Extended Data Fig. 7 | Perturbation sensitivity analysis.** AUROC across 27 parameter combinations (3 LFC thresholds  $\times$  3 control cell counts  $\times$  3 HVG counts). All conditions above chance ( $p < 0.005$ ); AUROC ranges 0.62–0.76.

**Extended Data Fig. 8 | Propensity-matched decomposition.** After matching DE-positive and DE-negative targets on gene-level covariates, edge AUROCs drop to near chance and LR incremental value is exactly zero.

**Extended Data Fig. 9 | Orthogonal causal interventions and intervention-fidelity diagnostics.** (A–B) Uniform attention replacement and MLP pathway ablation both produce exactly baseline AUROC, confirming the ablation null under three qualitatively different intervention channels. (C–D) All six interventions materially perturb hidden-state representations (max cosine distance 0.023–0.190), with TRRUST-ranked heads producing 23 $\times$  larger logit perturbation than random heads at matched dose, confirming that behavioral nulls reflect genuine functional redundancy rather than ineffective interventions.

**Extended Data Table 1 | Edge type summary.** Comprehensive comparison of attention, correlation, and gene-level features across all evaluation contexts, edge types, and cell types.

## Acknowledgements

We thank the scGPT development team for making their models publicly available, the Tabula Sapiens Consortium for open data access, and the broader single-cell foundation model community for establishing benchmark datasets and evaluation protocols.

## Data Availability

All analysis scripts, data processing pipelines, source data for all figures and tables, and reproducibility instructions are deposited at Zenodo (<https://doi.org/10.5281/zenodo.18701417>). All primary datasets (Tabula Sapiens, Repliglo Perturb-seq, Dixit/Adamson/Shifrut datasets) are publicly available from their original sources.

## Code Availability

Complete analysis code, figure generation scripts, CSSI implementation, and computational environment specifications are available at <https://github.com/Biodyn-AI/biomechinterp-framework> and archived at Zenodo (<https://doi.org/10.5281/zenodo.18701417>).

## Competing Interests

The author declares no competing interests.

## Ethics Declaration

This study used only publicly available, de-identified single-cell transcriptomic datasets. No new human or animal data were generated. No ethical approval was required.

# Supplementary Information

## Systematic Evaluation of Single-Cell Foundation Model Interpretability Reveals Attention Captures Co-Expression Rather Than Unique Regulatory Signal

Ihor Kendiukhov

## Contents

Supplementary Table 1: Analysis and Dataset Overview . . . . .	17
Supplementary Note 1 Metric-Dependent Scaling Behavior . . . . .	18
Supplementary Note 2 Baseline Comparison . . . . .	22
Supplementary Note 3 Systematic Bias in Single-Component Mediation Analysis . . . . .	23
Supplementary Note 4 Detectability Phase Diagrams . . . . .	26
Supplementary Note 5 Cross-Tissue Consistency . . . . .	28
Supplementary Note 6 Perturbation Validation Details . . . . .	29
6.1 Condition-specific perturbation validation (scGPT mediation) . . . . .	29
6.2 Perturbation-first validation on Replogle CRISPRi K562 . . . . .	29
6.3 Sensitivity analysis (27 parameter combinations) . . . . .	29
6.4 Attention perturbation-first evaluation . . . . .	30
6.5 Reconciling perturbation counts . . . . .	30
Supplementary Note 7 Cross-Species Ortholog Transfer . . . . .	31
Supplementary Note 8 Pseudotime Directionality Audit . . . . .	33
Supplementary Note 9 Batch and Donor Leakage Audit . . . . .	34
Supplementary Note 10 Uncertainty Calibration . . . . .	35
Supplementary Note 11 CSSI Detailed Results . . . . .	36
11.1 Synthetic validation . . . . .	36
11.2 Null stress tests . . . . .	36
11.3 Real-data-structured validation . . . . .	37
11.4 Real attention matrix validation . . . . .	37
Supplementary Note 12 Synthetic Ground-Truth Validation . . . . .	39
Supplementary Note 13 Multi-Model Validation . . . . .	40
13.1 Geneformer V1-10M GRN recovery . . . . .	40
13.2 Attention-correlation mapping . . . . .	40
13.3 Residualization on expression covariates . . . . .	40
13.4 Degree-preserving null models . . . . .	41
13.5 TRRUST circularity sensitivity analysis . . . . .	44
Supplementary Note 14 Mechanistic Localization Details . . . . .	45
14.1 Full 18-layer perturbation-first profile . . . . .	45
14.2 Attention-specific confound decomposition . . . . .	45
14.3 Original 6-condition ablation . . . . .	47
14.4 Orthogonal causal interventions . . . . .	47
14.5 Cross-context CRISPRa replication . . . . .	48
14.6 Cross-context T-cell CRISPRi replication . . . . .	49
14.7 Intervention-fidelity diagnostics . . . . .	49
14.8 Propensity-matched perturbation benchmark . . . . .	50
14.9 HVG protocol confound test . . . . .	51
Supplementary Note 15 Metric-Robust Incremental-Value Analysis . . . . .	53
Supplementary Note 16 Statistical Test Registry and Multiple Testing Correction . . . . .	54
16.1 Framework-level statistical correction . . . . .	54
16.2 Statistical test registry . . . . .	54
16.3 Claim-to-evidence mapping . . . . .	63

Supplementary Methods . . . . .	64
16.4    Summary statistics . . . . .	64
Supplementary Note 17	66
Biological Characterization of Attention Patterns . . . . .	68
Supplementary Note 18	70
Value-Weighted Edge Extraction . . . . .	70
Supplementary Note 19	71
Per-TF Characterization (Exploratory) . . . . .	71

## Supplementary Table 1: Analysis and Dataset Overview

Table S1: **Edge type used in each analysis.** “Attention” denotes Geneformer V2-316M attention-derived edges; “Correlation” denotes Spearman correlation from the same control cells.

Analysis	Edge Type	Dataset	Key AUROC
Scaling behavior	Attention	scGPT kidney	0.86–0.93
Controlled composition	Correlation	TS kidney	0.52–0.56
Residualization	Correlation	DLPFC brain	0.73 (resid.)
Degree-preserving null	Correlation	DLPFC brain	0.69 (null)
Perturbation-first (corr.)	Correlation	Reproglo K562	0.696
Perturbation-first (attn.)	Attention	Reproglo K562	0.704
Full 18-layer profile	Attention	Reproglo K562	0.47–0.74
Attn. residualization	Attention	Reproglo K562	0.54 (resid.)
Attn. degree-null	Attention	Reproglo K562	0.63 (null)
Incremental value	Both + gene-level	Reproglo K562	0.895 (gene)
Per-head TRRUST	Attention (per-head)	Reproglo K562	0.34–0.75
Head-level ablation	Attention (ablated)	Reproglo K562	0.699–0.704
Cross-context (CRISPRa)	Both	Adamson K562	0.55 vs 0.65
Trivial baselines	Gene-level	Reproglo K562	0.81–0.88
Non-K562 replication	Both	Reproglo RPE1	0.75 vs 0.66
RPE1 trivial baselines	Gene-level	Reproglo RPE1	0.80–0.87
RPE1 incremental value	Both + gene-level	Reproglo RPE1	0.942 (gene)
RPE1 residualization	Both	Reproglo RPE1	0.53 (attn resid.)

Table S2: Perturbation sample counts across datasets and configurations.

Dataset	Modality / Config	DE Thresh.	n	Notes
Reproglo K562	CRISPRi (baseline)	LFC>0.1	44	Mann-Whitney, HVG=1000, $N_{ctrl}=500$
Reproglo K562	CRISPRi (primary)	LFC>0.5	151	Welch <i>t</i> , HVG=2000, $N_{ctrl}=2000$
Reproglo K562	CRISPRi (attention)	LFC>0.5	280	Welch <i>t</i> , HVG=2000; more genes evaluable with attention tokenization
Adamson K562	CRISPRa	LFC>0.5	77	K562, activation modality
Shifrut T cells	CRISPRi	LFC>0.1	7	Primary human T cells; weak DE effects require lenient threshold
Reproglo RPE1	CRISPRi	LFC>0.5	1,251	hTERT-RPE1; perturbation genes forced into HVG
Tian iPSC neurons	CRISPRi	LFC>0.1	7	iPSC-derived glutamatergic neurons

## Supplementary Note 1 Metric-Dependent Scaling Behavior

To test whether increasing dataset size improves interpretability, we analyzed archived scGPT kidney scaling runs across three model tiers (small/medium/large), three seeds per tier, and three cell counts (200, 1,000, 3,000). Each run yields an attention-derived score for each directed gene pair; we construct a sparse GRN by retaining the top-100 targets per source gene and evaluate recovery against TRRUST and DoRothEA reference edges restricted to the run-specific gene universe.

**Evidence: scaling degrades recovery.** TRRUST F1 decreases with cell count across model tiers (Supplementary Fig. S1); the  $200 \rightarrow 1,000$  change is negative in all 9 tier $\times$ seed pairs (exact one-sided sign test  $p = 0.00195$ ). The same pattern holds for DoRothEA ( $p = 0.00195$ ). The  $1,000 \rightarrow 3,000$  step shows continued degradation in 7/9 pairs (sign test  $p = 0.09$ ), weaker but directionally consistent.

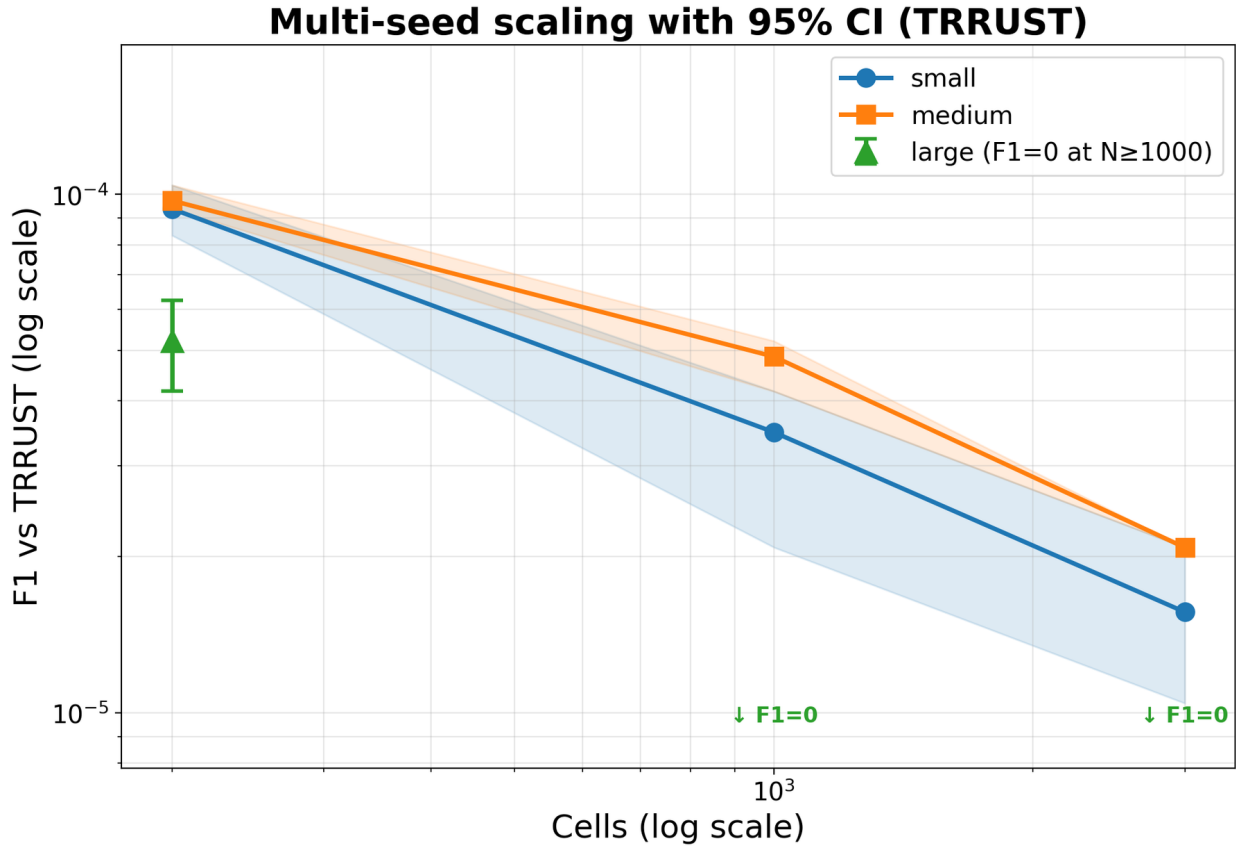


Figure S1: **Metric-dependent scaling behavior in scGPT attention-derived GRN recovery (kidney).** TRRUST F1 with 95% confidence intervals across three model tiers (small/medium/large) and cell counts (200/1,000/3,000).

**Retrieval collapse.** The number of recovered true positives decreases toward (and sometimes below) random expectation as  $N$  increases (Supplementary Fig. S2), indicating that scaling can reduce enrichment rather than merely saturate.

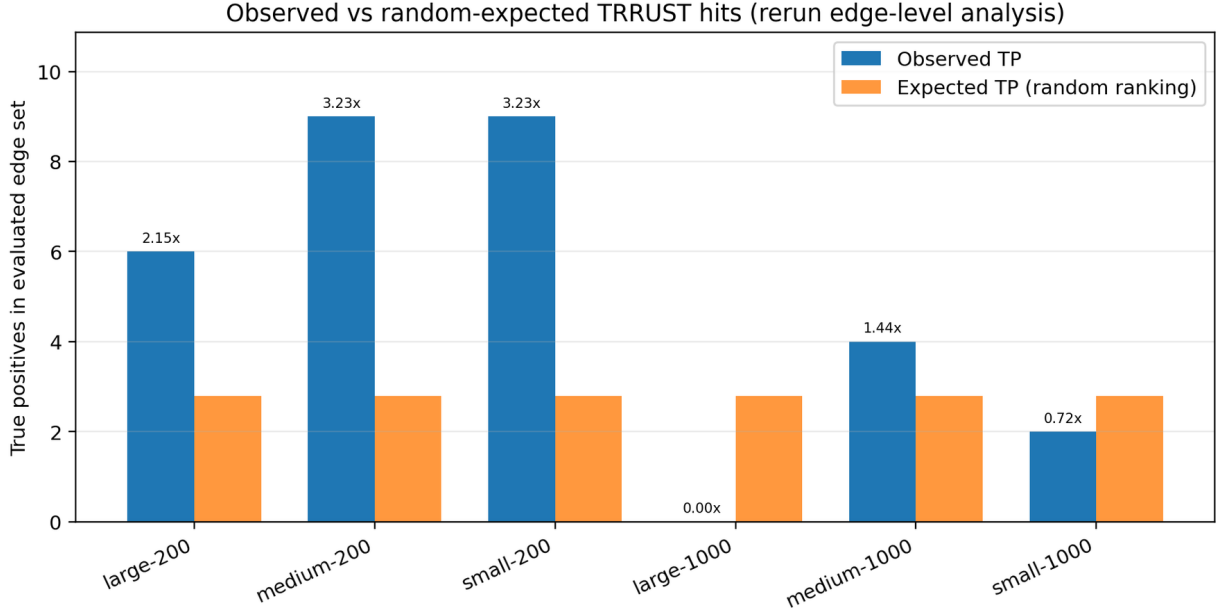


Figure S2: **Retrieval collapse with scaling (scGPT kidney).** Observed true positives versus random-expected true positives for attention-derived GRNs.

**Robustness also degrades with scaling.** Between-seed stability decreases substantially from 200 to 1,000 cells (Supplementary Table S3): edge-set Jaccard overlaps drop by 46.6–47.9% depending on tier (one-sided Mann–Whitney  $p = 2.1 \times 10^{-4}$  across all tiers/seeds).

Table S3: **Between-seed robustness of inferred edge sets (scGPT kidney).**

Tier	Jaccard (200)	Jaccard (1,000)	Spearman (200)	Spearman (1,000)
Small	0.572	0.305	0.211	-0.065
Medium	0.562	0.293	0.183	-0.110
Large	0.536	0.285	0.083	-0.130

**Heterogeneity proxy (cell-type richness).** Reconstructing the exact subsampling used during attention extraction (manifest-specified random seeds), the number of observed kidney cell types increases with  $N$  and is strongly anti-correlated with TRRUST F1 across runs (Spearman  $\rho = -0.76$ ,  $p = 4.3 \times 10^{-5}$ ; Supplementary Fig. S3).

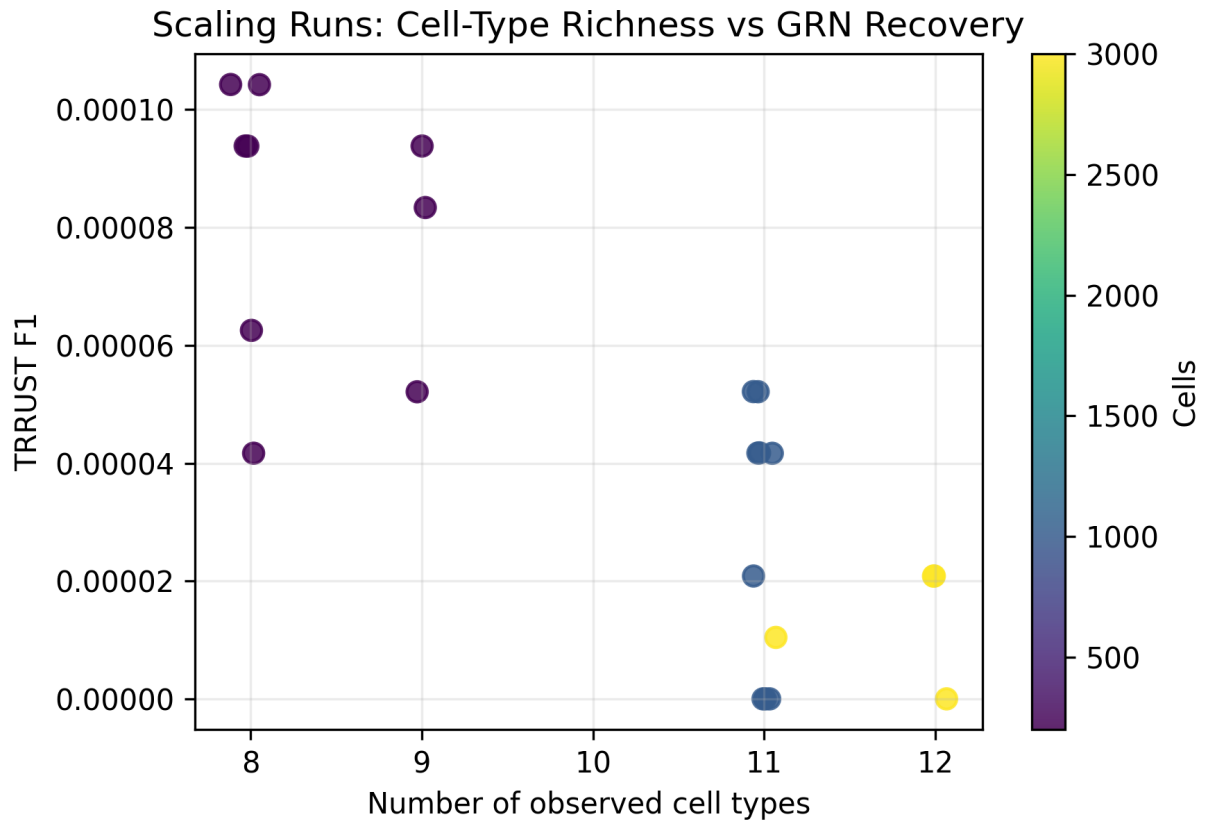


Figure S3: **Scaling runs: composition diversity proxy.** Across the scGPT kidney scaling grid, the number of observed cell types in the sampled cells increases with  $N$  and is anti-correlated with GRN recovery.

**K-sensitivity and continuous AUROC.** The top- $K$  F1 metric used above is inherently sensitive to  $K$ , and the 1,930-gene universe of these scaling runs contains only 51 TRRUST edges among  $\sim 3.7$  million candidate pairs (positive rate  $< 0.002\%$ ). To test whether the scaling finding is metric-dependent, we re-evaluated the archived attention-score matrices at  $K \in \{20, 50, 100, 200, 500\}$  and computed continuous-score AUROC (no top- $K$  thresholding). F1 values are effectively zero at all  $K$  values ( $\sim 10^{-4}$ ), confirming that near-zero absolute performance is driven by extreme reference sparsity rather than a specific  $K$  choice. However, continuous-score AUROC tells a different story: it *improves* monotonically with cell count (mean 0.858 at  $N = 200$ , 0.925 at  $N = 1,000$ , 0.934 at  $N = 3,000$ ; 0/9 runs show degradation; Supplementary Fig. S4). This reversal under continuous AUROC indicates that the scaling behavior is metric-dependent: while the thresholded top- $K$  edge set degrades with  $N$ , the continuous *ranking* of all gene pairs against curated references improves.

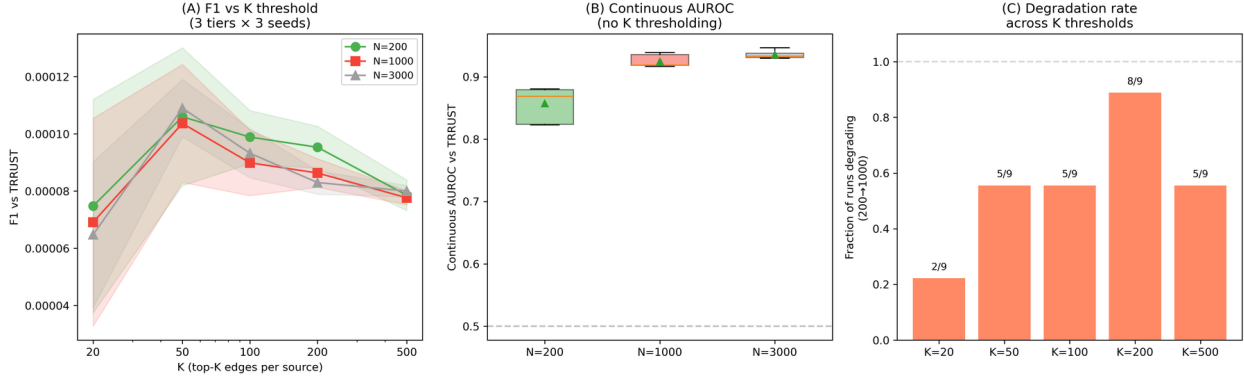


Figure S4: **K-sensitivity and continuous AUROC for scaling runs.** (A) F1 vs  $K$  at different cell counts. (B) Continuous AUROC improves monotonically with cell count ( $0.858 \rightarrow 0.925 \rightarrow 0.934$ ). (C) Fraction of runs showing degradation across  $K$  values.

**Controlled-composition scaling.** To test whether top- $K$  scaling degradation is driven by sample size  $N$  or by heterogeneity, we conducted a controlled experiment on Tabula Sapiens kidney data using correlation-based edge scores under three conditions (Supplementary Fig. S5): (i) a single cell type (kidney epithelial) with varying  $N$  (100–3,000), (ii) mixed cell types with fixed equal composition across  $N$  (100–1,000), and (iii) fixed  $N = 500$  with increasing heterogeneity (1–7 cell types). Under condition (i), AUROC shows a weak non-significant downward trend (Spearman  $\rho = -0.33$ ,  $p = 0.079$ ). Under condition (ii), AUROC is stable ( $\rho = -0.05$ ,  $p = 0.82$ ). Under condition (iii), AUROC actually *increases* with heterogeneity ( $\rho = +0.63$ ,  $p = 10^{-4}$ ).

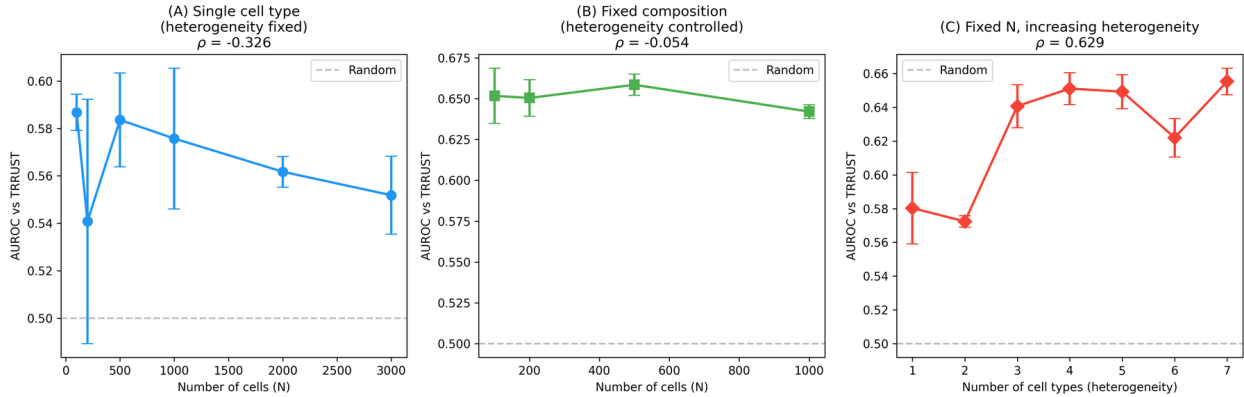


Figure S5: **Controlled-composition scaling.** (A) Single cell type: no significant degradation with  $N$ . (B) Fixed composition: stable AUROC. (C) Increasing heterogeneity at fixed  $N$ : AUROC increases.

## Supplementary Note 2 Baseline Comparison

We evaluated multiple baseline approaches on DLPFC brain tissue data (500 randomly sampled cells, top 500 most variable genes): Spearman correlation, mutual information, GENIE3 [Huynh-Thu et al., 2010], GRNBoost2 [Moerman et al., 2019], and attention-based edge scores. All methods were evaluated against TRRUST and DoRothEA using AUROC, AUPRC, and Precision@10k.

All approaches show similar poor performance, with AUROC values clustering around 0.50–0.53: Spearman correlation (AUROC 0.521), mutual information (0.518), GENIE3 (0.523), GRNBoost2 (0.526), and attention-based methods (0.524). State-of-the-art dedicated GRN inference algorithms achieve nearly identical performance to attention-based approaches, while requiring 89–127 seconds computation time versus 0.1 seconds for attention extraction. The convergence toward  $\text{AUROC} \approx 0.5$  in this DLPFC brain setting suggests that benchmarking against curated TF–target databases in context-mismatched tissues can be dominated by evaluation limitations.

### Supplementary Note 3 Systematic Bias in Single-Component Mediation Analysis

Activation patching has become the standard tool for localizing mechanistic function in transformers [Meng et al., 2022, Vig et al., 2020, Goldowsky-Dill et al., 2023]. However, the standard single-component protocol implicitly assumes additivity. We formalize the bias problem following the causal mediation framework of Pearl [2001] and Imai et al. [2010]. For mediator component  $i$ , the bias relative to the interaction-aware Shapley value  $\phi_i$  [Shapley, 1953, Lundberg and Lee, 2017] decomposes as:

$$b_i = \hat{m}_i - \phi_i = - \sum_{|S| \geq 2, i \in S} \frac{\mu(S)}{|S|} + \varepsilon_i \quad (1)$$

where  $\mu(S)$  represents Möbius interaction coefficients. We introduce an observable lower bound on aggregate non-additivity:

$$A_{lb} = \max(0, |R| - 1.96 \cdot SE(R)) \quad (2)$$

where  $R = TE - \sum_i \hat{m}_i$  is the residual between total effect and the sum of single-component estimates.

Analysis of frozen cross-tissue mediation archives revealed substantial and frequent additivity violations. Across 16 run-pairs, lower bounds on aggregate non-additivity were positive in 10 cases (rate 0.625), with median  $A_{lb}/|TE| = 0.725$  (Supplementary Fig. S6). Ranking certificates proved fragile: mean certified pair coverage dropped from 0.0669 at  $\lambda = 1$  to 0.0032 by  $\lambda \geq 3$  (Supplementary Fig. S7).

**Real-data residual non-additivity  
(values shown above each bar)**

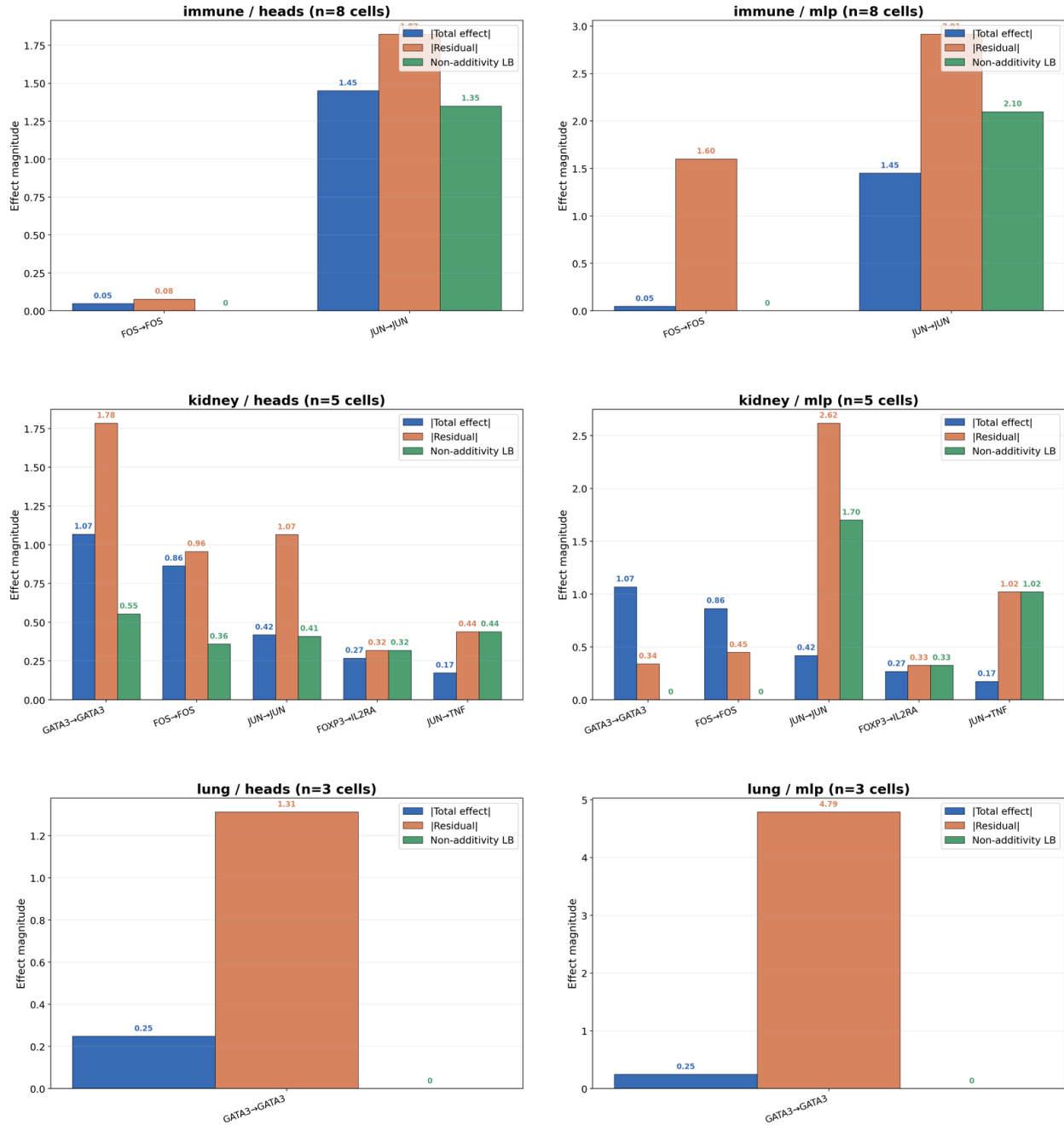


Figure S6: **Non-additivity in mediation analysis.** Absolute total effect, residual non-additivity, and lower-bound interaction magnitude per run-pair.

### Ranking certification sensitivity to structural-bias assumptions

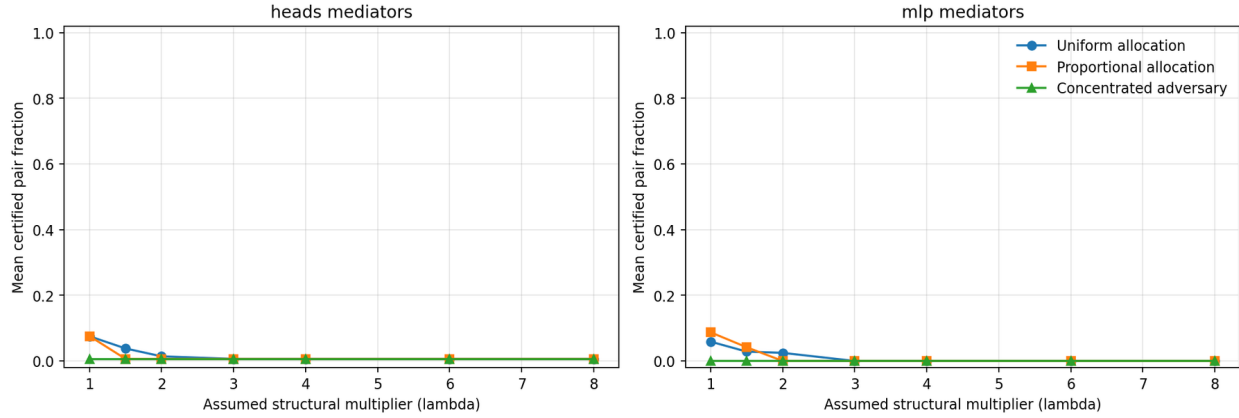


Figure S7: **Ranking certificate fragility.** Mean certified pair fraction versus structural multiplier  $\lambda$ .

Non-additivity is common in our data (62.5% of 16 run-pairs across 3 tissues) and concentrates in biologically meaningful contexts. These findings indicate that standard single-component rankings may be unreliable in contexts with complex regulatory interactions, though the sample warrants further validation at larger scale. Mechanistic claims should be accompanied by the residual non-additivity ratio  $A_{lb}/|TE|$ , ranking certificates, and interaction-aware alternatives such as Shapley-value decomposition.

## Supplementary Note 4 Detectability Phase Diagrams

We developed a closed-form detectability framework rooted in statistical detection theory [Donoho and Jin, 2004]. For a mechanistic signal with effect size  $|\mu|$ , noise scale  $\sigma$ , and tail inflation factor  $\tau$ , the required sample size for detection is:

$$n^* = \left( \frac{(z_{1-\alpha/(2m)} + z_{\text{power}}) \tau \sigma}{|\mu|} \right)^2 \quad (3)$$

Under sub-Gaussian baseline conditions, intervention-like signals required only 44.4% as many cells as attention-like signals for equivalent detectability (Supplementary Fig. S8). However, this advantage collapsed progressively under tail inflation, with the relative cell ratio approaching unity when  $\tau > 3$ .

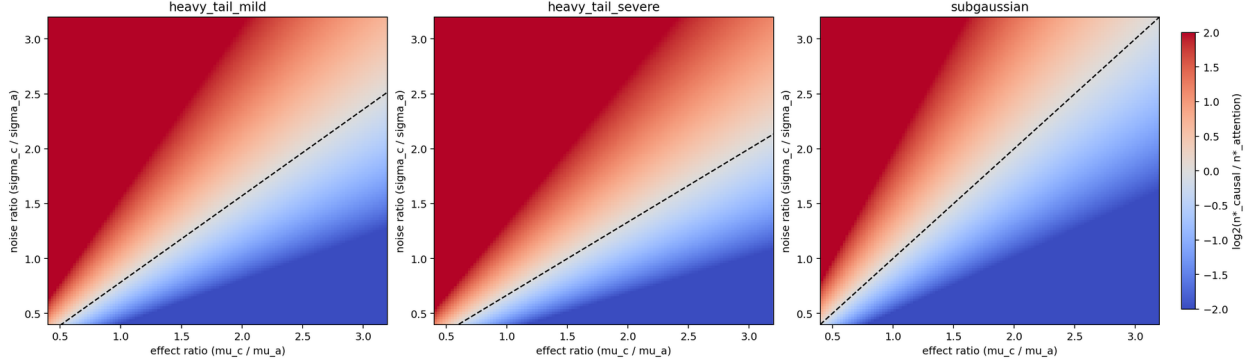


Figure S8: **Detectability phase diagrams.** Different regimes where attention-like versus intervention-like signals become detectable.

Robust estimation (median-based or Huber M-estimators [Huber, 1964]) expanded the feasible detection region by 37% under 10% contamination. Real-data calibration showed projected relative cell ratios below one in most bootstrap draws, but confidence intervals remained wide (Supplementary Fig. S9).

Tiny real-data projection from standardized proxy effects

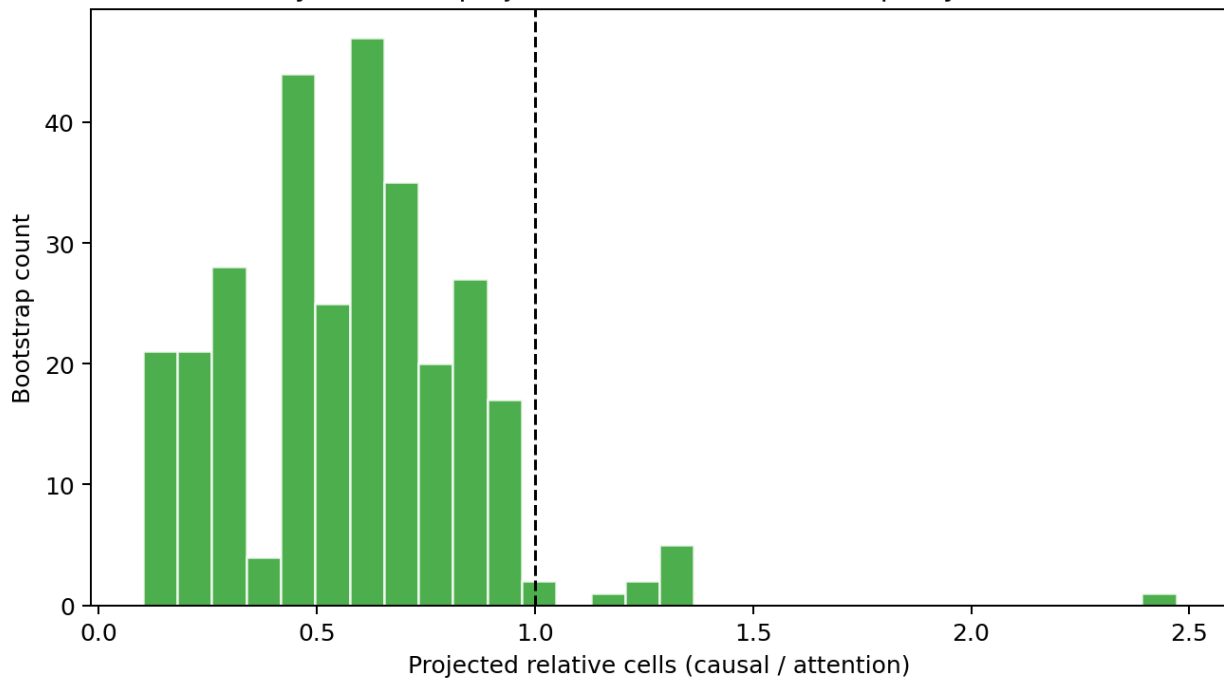


Figure S9: **Real data detectability calibration.** Bootstrap distribution of projected relative cell requirements.

## Supplementary Note 5 Cross-Tissue Consistency

Cross-tissue analysis across immune, kidney, and lung tissues revealed Spearman correlations ranging from  $-0.44$  to  $0.71$ , with only two of six pair-granularity comparisons surviving FDR control at  $\alpha = 0.05$  (Supplementary Fig. S10). Limited transferability is consistent with known tissue-specificity of gene regulation. Negative correlations in some tissue pairs suggest either genuine context-dependent regulation or tissue-specific confounds.

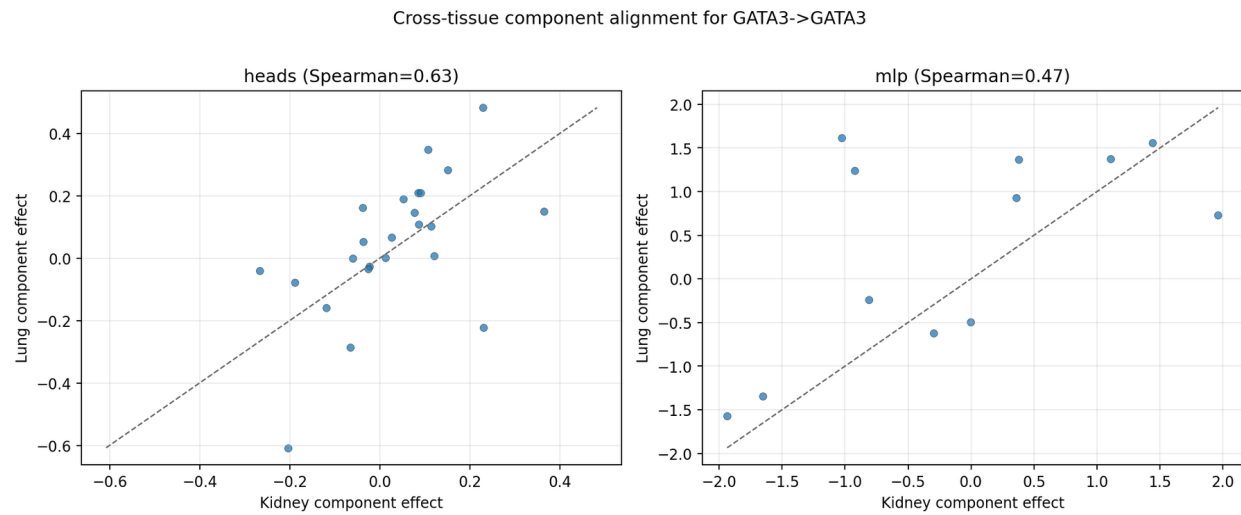


Figure S10: **Cross-tissue consistency variability.** Scatter plots of component-level effects between tissue pairs.

An important alternative interpretation is that technical batch effects between tissue datasets may partly explain the low consistency. Our batch leakage analysis (Supplementary Note 9) confirms that technical covariates are recoverable from edge features. Distinguishing genuine regulatory rewiring from technical artifacts would require matched protocols across tissues.

## Supplementary Note 6 Perturbation Validation Details

### 6.1 Condition-specific perturbation validation (scGPT mediation)

Counterfactual validation against four CRISPR Perturb-seq datasets revealed weak and condition-specific alignment. The strongest positive signal appears in Dixit 13-day: consistency is positive ( $\rho = 0.269, p = 0.032$ ) and remains positive after confound adjustment ( $\rho = 0.199, p = 0.020$ ). Dixit 7-day shows weaker non-significant consistency ( $\rho = 0.112, p = 0.15$ ). Adamson shows marginal agreement ( $p = 0.089$ ). Shifrut shows raw anti-alignment ( $\rho = -0.325, p = 0.031$ ) that collapses after adjustment ( $\rho = 0.004, p = 0.876$ ). Under framework-level BH correction, only the Dixit 13-day confound-adjusted correlation survives (adj.  $p = 0.042$ ).

### 6.2 Perturbation-first validation on Replate CRISPRi K562

Under our primary parameterization ( $N_{ctrl} = 2000$ , HVG = 2000, LFC  $> 0.5$ , Welch's  $t$ -test with BH-FDR correction), the mean per-gene AUROC was 0.696 ( $n = 151$  evaluable perturbations,  $p < 10^{-4}$ ; Supplementary Fig. S11).

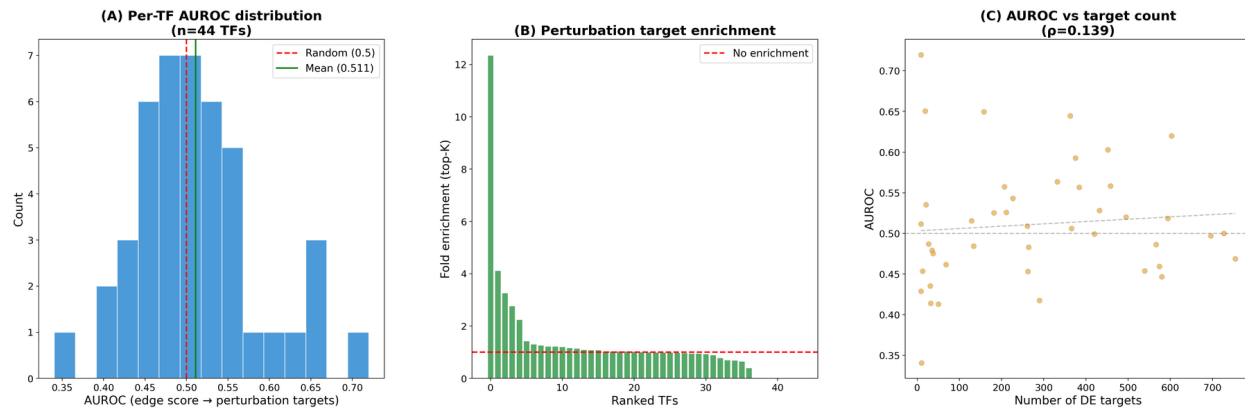


Figure S11: Perturbation-first validation (Replate CRISPRi K562). Per-gene AUROC for predicting DE targets from correlation-based edge scores under primary parameterization.

### 6.3 Sensitivity analysis (27 parameter combinations)

We systematically varied the number of control cells ( $N_{ctrl} \in \{500, 2000, 10000\}$ ), gene universe (HVG  $\in \{1000, 2000, 5000\}$ ), and DE stringency (LFC threshold  $\in \{0.25, 0.5, 1.0\}$ ), yielding 27 parameter combinations (Supplementary Fig. S12). All 27 conditions yielded AUROC significantly above chance ( $p < 0.005$ ). AUROC ranged from 0.619 to 0.756.

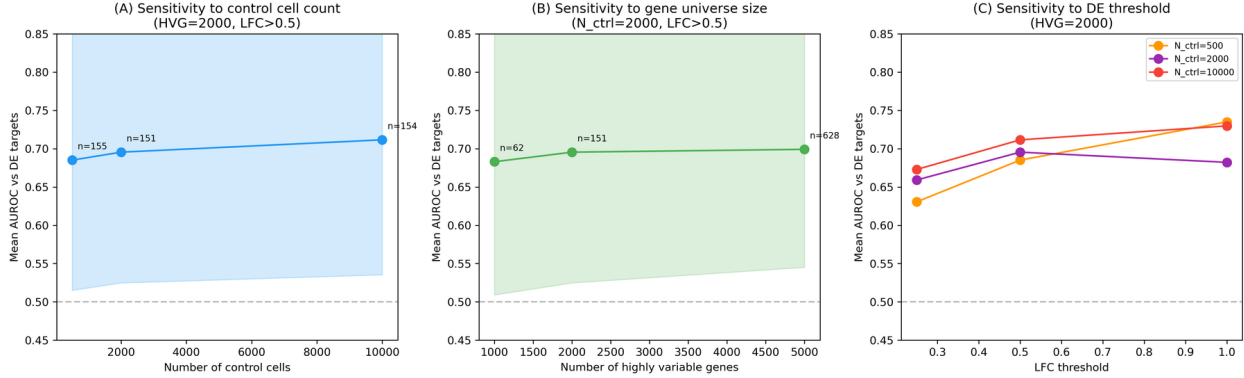


Figure S12: **Perturbation-first sensitivity analysis (27 parameter combinations).** Mean AUROC varies with (A) number of control cells, (B) gene universe size, and (C) LFC threshold.

#### 6.4 Attention perturbation-first evaluation

Geneformer V2-316M attention-derived AUROC is statistically indistinguishable from correlation at all three layers: L6 =  $0.705 \pm 0.145$  ( $p = 0.76$ ), L13 =  $0.704 \pm 0.147$  ( $p = 0.73$ ), L18 =  $0.708 \pm 0.157$  ( $p = 0.75$ ), vs. correlation =  $0.703 \pm 0.164$  (Supplementary Fig. S13).

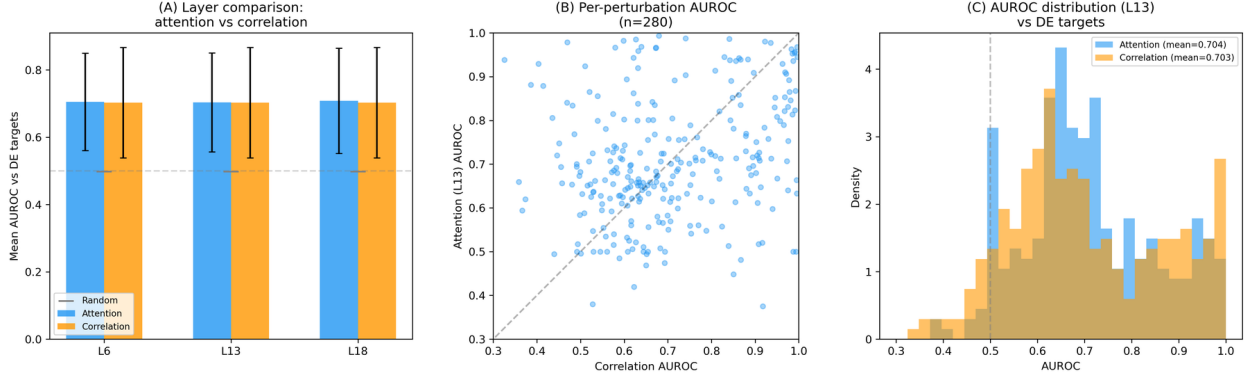


Figure S13: **Attention-derived edges are indistinguishable from correlation on perturbation-first prediction.** Geneformer V2-316M attention (L13) vs. correlation-based edges ( $n = 280$ ).

#### 6.5 Reconciling perturbation counts

The number of evaluable perturbations varies across parameterizations because each imposes different inclusion criteria. The lenient baseline (Mann–Whitney,  $|LFC| > 0.1$ , 500 control cells) yields 44 evaluable genes; the primary correlation-based parameterization (Welch’s  $t$ -test,  $LFC > 0.5$ ,  $HVG = 2,000$ ,  $N_{ctrl} = 2,000$ ) yields  $n = 151$ ; and the attention comparison under the same DE thresholds yields  $n = 280$  because the expanded gene-matching procedure identifies more evaluable perturbations when matching against the full tokenized gene set.

## Supplementary Note 7 Cross-Species Ortholog Transfer

To test whether mechanistic signals generalize across species, we performed a systematic stress test of TF–target edge transfer between human and mouse lung using correlation-based edge scores computed independently in each species [Travaglini et al., 2020]. Cross-species comparison of 25,876 matched TF–target edges revealed strong global conservation (Supplementary Fig. S14). The Spearman rank correlation between human and mouse edge scores was  $\rho = 0.743$  ( $p < 10^{-300}$ ). Sign agreement was 88.6% across all shared edges, rising to 100% for edges with  $|\rho| > 0.4$  in both species. Top- $k$  overlap was enriched 8- to 484-fold over random expectation (Supplementary Table S4).

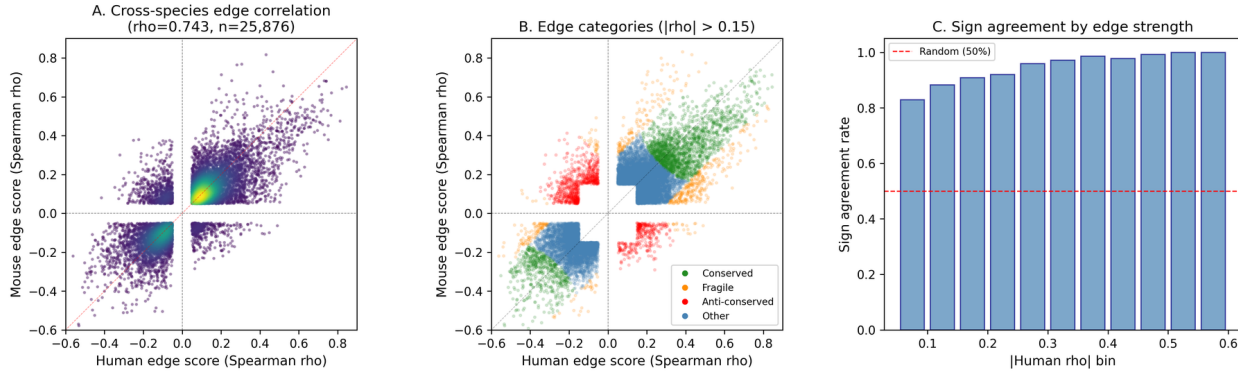
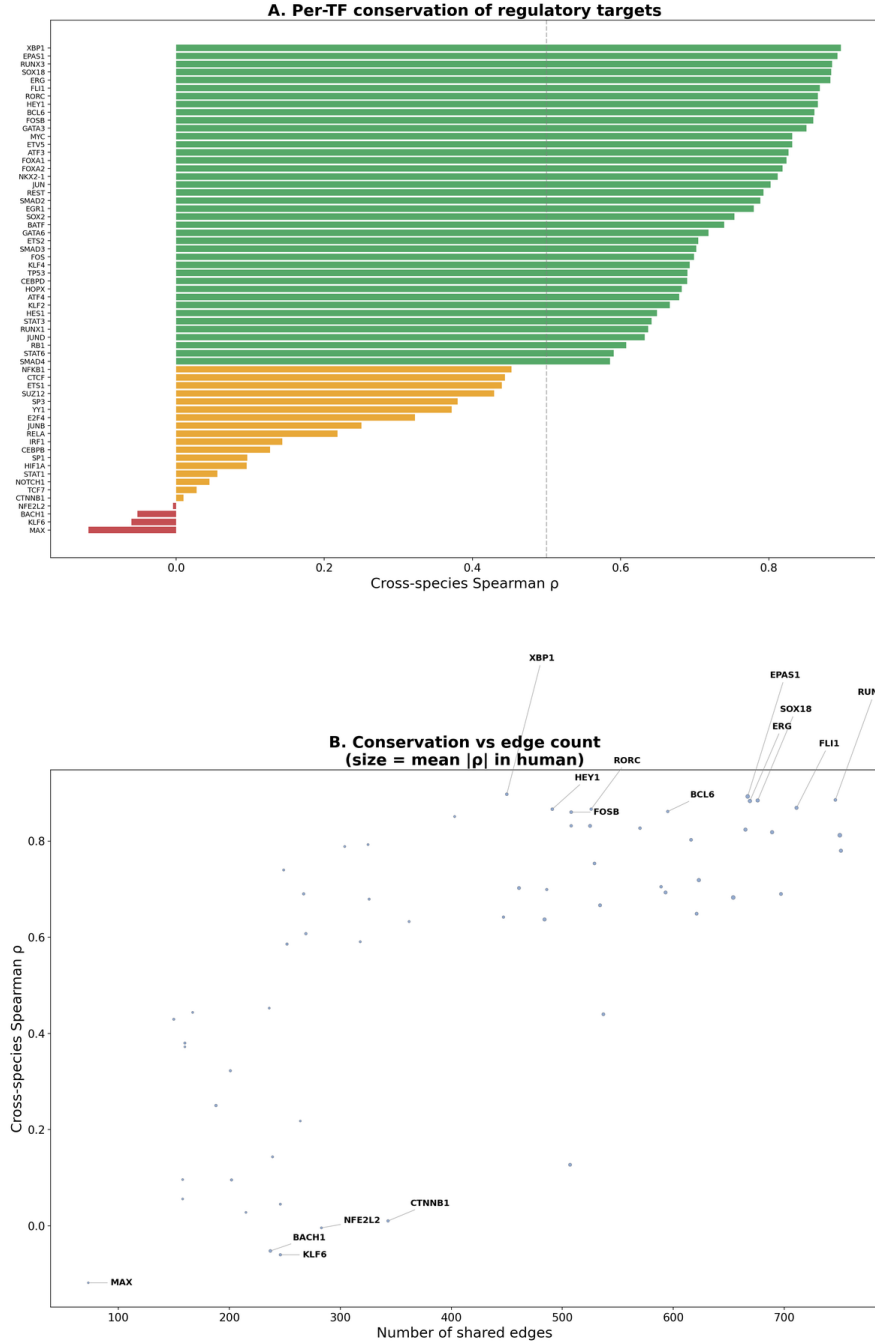


Figure S14: **Cross-species edge score conservation.** Scatter plot of Spearman  $\rho$  for 25,876 matched TF–target edges between human and mouse lung.

Table S4: **Top- $k$  overlap between human and mouse edge rankings.**

Top $k$	Observed	Expected	Fold
100	26	0.1	484×
500	153	1.3	114×
1,000	289	5.4	54×
5,000	1,094	134.2	8.2×

However, per-TF conservation was highly non-uniform (Supplementary Fig. S15). Lineage-specifying factors showed near-perfect transfer: XBP1 ( $\rho = 0.90$ ), EPAS1 (0.89), ERG (0.88), NKX2-1 (0.81). In contrast, signaling-responsive TFs showed poor conservation: CTNNB1 (0.01), HIF1A (0.10), STAT1 (0.06), CEBPB (0.13). Fragile edges (599 total) were enriched for immune-cell-specific RUNX3 targets with species-divergent expression.



**Figure S15: Per-TF conservation of regulatory targets across species.** (A) Horizontal bar chart of cross-species Spearman  $\rho$  for each TF's target set (green:  $\rho \geq 0.5$ , orange:  $0 \leq \rho < 0.5$ , red:  $\rho < 0$ ). Lineage-specifying TFs (XBP1, EPAS1, RUNX3) show near-perfect conservation ( $\rho > 0.88$ ), while signaling-responsive TFs (MAX, BACH1, CTNNB1) show poor or negative conservation. (B) Conservation versus number of shared orthologous edges. Point size reflects mean absolute attention weight ( $|\rho|$ ) in human. High-conservation TFs tend to have more shared edges, but low-conservation outliers (MAX, KLF6) persist despite moderate edge counts.

Ortholog-based edge transfer should be stratified by TF class: lineage-specifying programs can be transferred with high confidence, while signaling-responsive and composition-dependent edges require species-specific validation.

## Supplementary Note 8 Pseudotime Directionality Audit

Using diffusion pseudotime [Haghverdi et al., 2016] in three Tabula Sapiens immune lineages, we tested 56 curated TF-target pairs for lag-based directional consistency. Only 12 of 56 TF-target pairs (21.4%) were directionally consistent (Supplementary Fig. S16). Consistency varied by lineage: myeloid pairs showed the highest rate (6/17, 35.3%), followed by T cell (4/24, 16.7%) and B cell (2/15, 13.3%). The mean directionality score marginally exceeded a shuffled-pseudotime null ( $p = 0.068$ ) but not a random gene-pair null ( $p = 0.37$ ; Supplementary Fig. S17); after framework-level FDR correction, this effect is not significant ( $q = 0.124$ ).

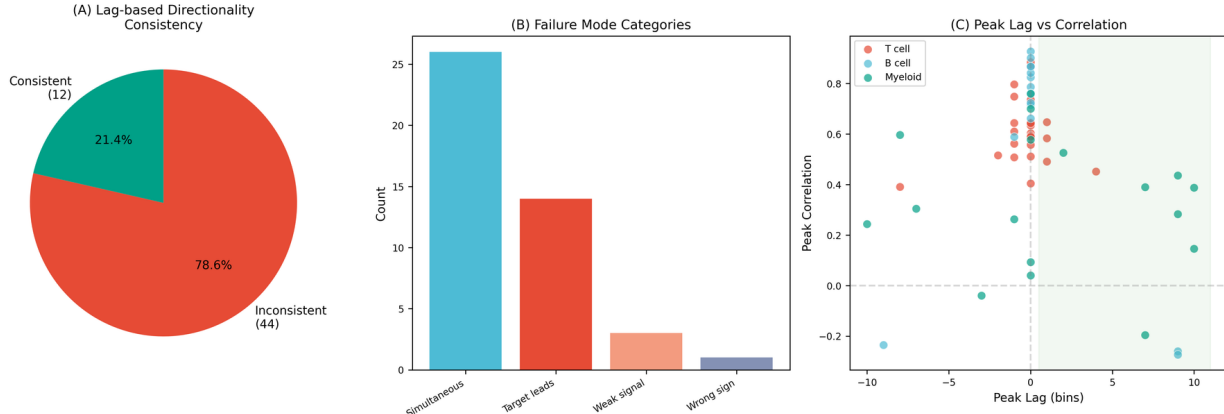


Figure S16: **Pseudotime directionality failures.** Only 12/56 TF-target pairs (21.4%) show directionally consistent lag-based ordering.

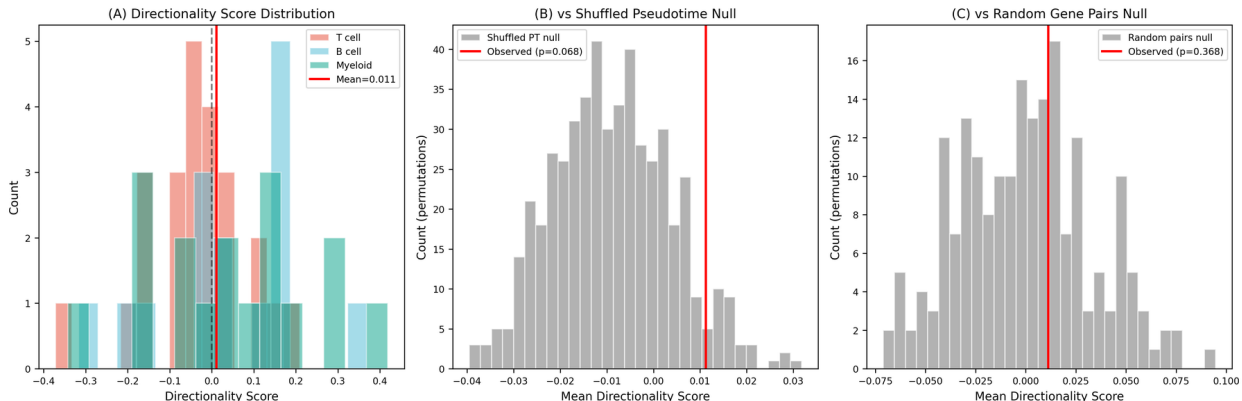


Figure S17: **Pseudotime null comparisons.** Mean directionality score marginally exceeds shuffled-pseudotime null ( $p = 0.068$ ) but not random gene-pair null ( $p = 0.37$ ).

Pseudotime should be treated as a qualitative sanity check rather than a pass/fail validator for mechanistic edges. Perturbation-based validation and time-resolved modalities (e.g., RNA velocity) provide more direct temporal or causal evidence.

## Supplementary Note 9 Batch and Donor Leakage Audit

We conducted a systematic leakage audit across three Tabula Sapiens tissue compartments. Leakage classifiers revealed substantial technical signal in edge-product features (Supplementary Fig. S18). Donor identity was recoverable well above chance: immune dataset AUC 0.85–0.87 (21 donors); lung dataset AUC 0.94–0.96 (4 donors). Assay method (10X vs. Smart-seq2) was the dominant confound, recoverable at AUC 0.96–0.99.

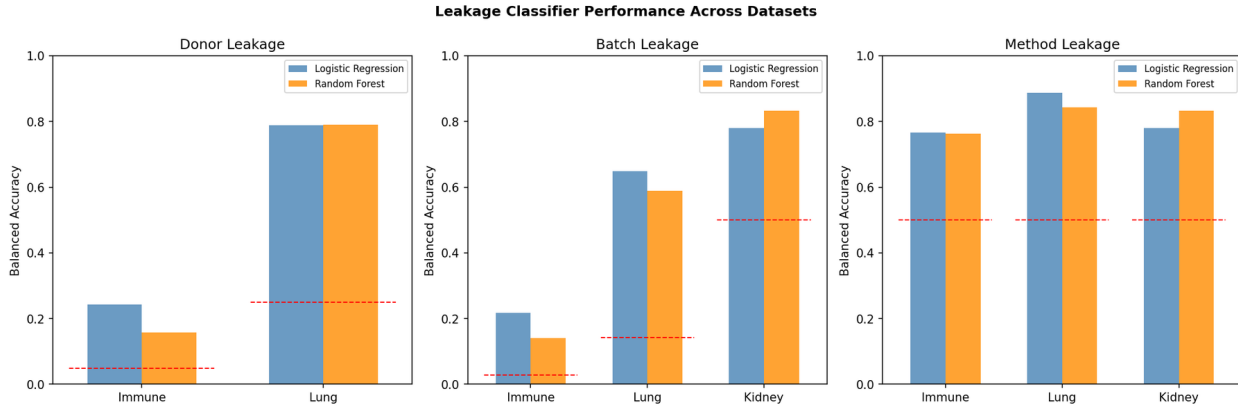


Figure S18: **Cross-dataset leakage summary.** Balanced accuracy and AUC for donor, batch, and method classification from edge-product features.

The practical impact was dataset-dependent. The well-balanced lung dataset showed remarkably stable aggregate edge scores under donor-balanced resampling ( $r = 0.997$ , 10.1% blacklisted). The imbalanced immune dataset showed genuine instability ( $r = 0.929$ , 54.6% blacklisted, 17.1% sign-flipped; Supplementary Fig. S19).

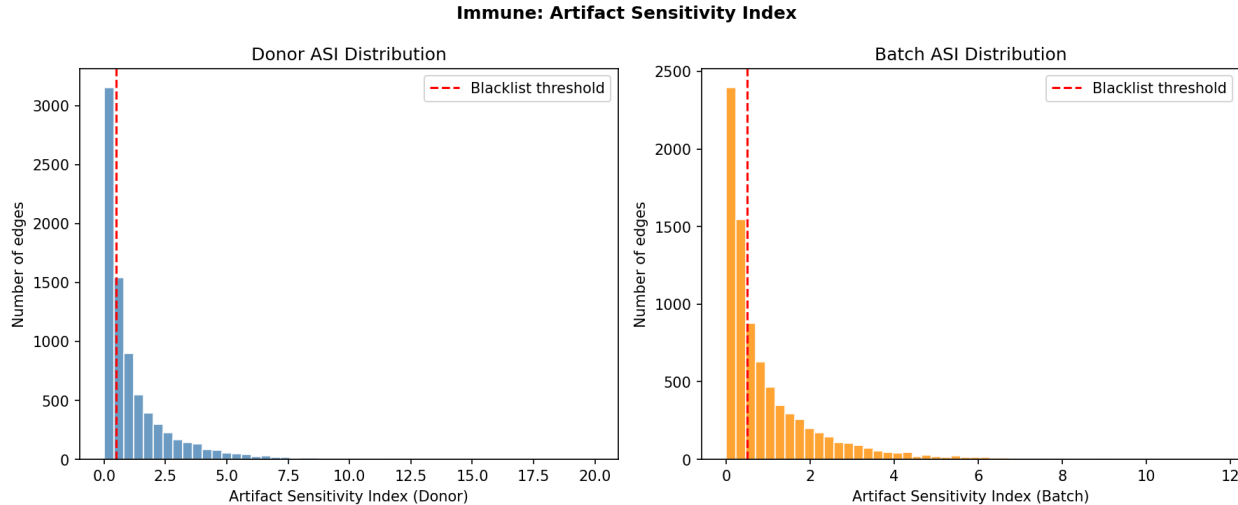


Figure S19: **Artifact Sensitivity Index distribution.** Immune tissue has 54.6% of edges exceeding ASI  $> 0.5$ .

Edge score evaluation must use donor-stratified splits, never random CV when donor metadata is available. The generalization gap (6.6 percentage points in lung) should be reported as a built-in quality check.

## Supplementary Note 10 Uncertainty Calibration

All six edge-scoring methods produced severely miscalibrated scores against Perturb-seq ground truth: raw Expected Calibration Error (ECE) ranged from 0.269 (ensemble) to 0.469 (LASSO; Supplementary Fig. S20). Post-hoc calibration dramatically improved score quality: isotonic regression reduced ECE to 0.062–0.079 (4–7× reduction) without changing discrimination.

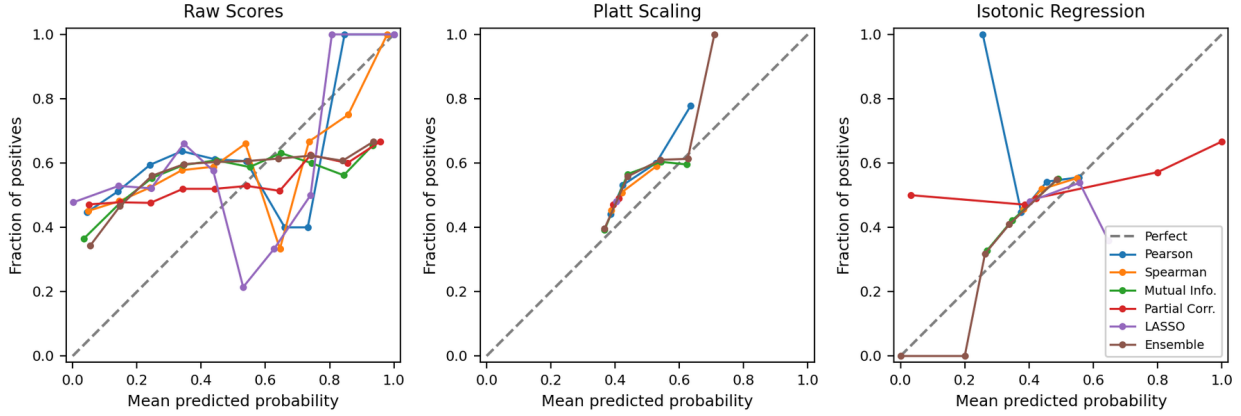


Figure S20: **Edge score calibration.** Reliability diagrams showing fraction of true positives vs. mean predicted probability. Platt scaling and isotonic regression reduce ECE by 4–7×.

Split conformal prediction sets achieved valid marginal coverage ( $\geq 95\%$ ) for mutual information and ensemble methods at  $\alpha = 0.05$ , with 13.4% singleton prediction sets for mutual information (Supplementary Fig. S21). Critically, calibrators did not transfer across datasets: K562-trained calibrators applied to the Shifrut T cell dataset yielded ECE 0.320–0.424, compared to 0.002–0.031 for locally trained calibrators.

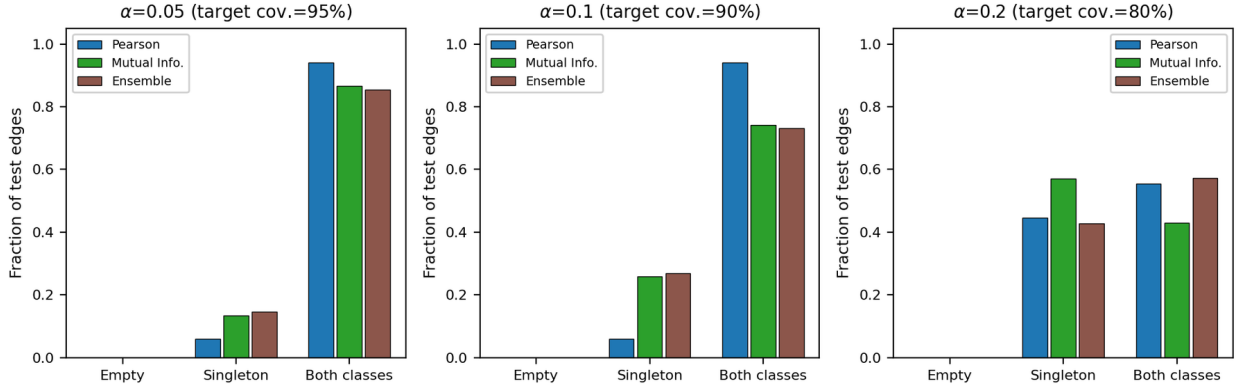


Figure S21: **Conformal prediction sets.** Empirical coverage and average set size across methods at  $\alpha = 0.05, 0.10, 0.20$ .

GRN methods should report calibrated scores alongside traditional rankings. Conformal prediction sets transform the question from “which edges to call” into “which edges can be confidently called.” Calibrators must be retrained per dataset.

## Supplementary Note 11 CSSI Detailed Results

### 11.1 Synthetic validation

In controlled synthetic experiments with state-specific GRNs, pooled inference exhibited strong top- $K$  scaling degradation: F1 decreased from  $0.850 \pm 0.053$  at 200 cells to  $0.514 \pm 0.083$  at 1,000 cells. CSSI-max with oracle labels substantially mitigated this degradation, maintaining  $F1 \geq 0.900$  across all configurations (Supplementary Table S5).

Table S5: **CSSI mitigates top- $K$  scaling degradation in synthetic experiments.**

Config	$N$	States	Pooled F1	CSSI-max F1	Ratio
Small	200	2	$0.850 \pm 0.053$	$0.957 \pm 0.050$	$1.13\times$
Medium	400	4	$0.657 \pm 0.100$	$0.921 \pm 0.071$	$1.40\times$
Large	600	6	$0.486 \pm 0.100$	$0.900 \pm 0.069$	$1.85\times$
XLarge	1000	8	$0.550 \pm 0.089$	$0.967 \pm 0.029$	$1.76\times$
XXLarge	1000	10	$0.514 \pm 0.083$	$0.932 \pm 0.049$	$1.81\times$
Massive	1500	12	$0.527 \pm 0.041$	$0.942 \pm 0.027$	$1.79\times$

### 11.2 Null stress tests

Under shuffled and random labels, CSSI-max AUROC *decreases* relative to pooled inference (Supplementary Fig. S22, Supplementary Fig. S23), confirming no false-positive inflation.

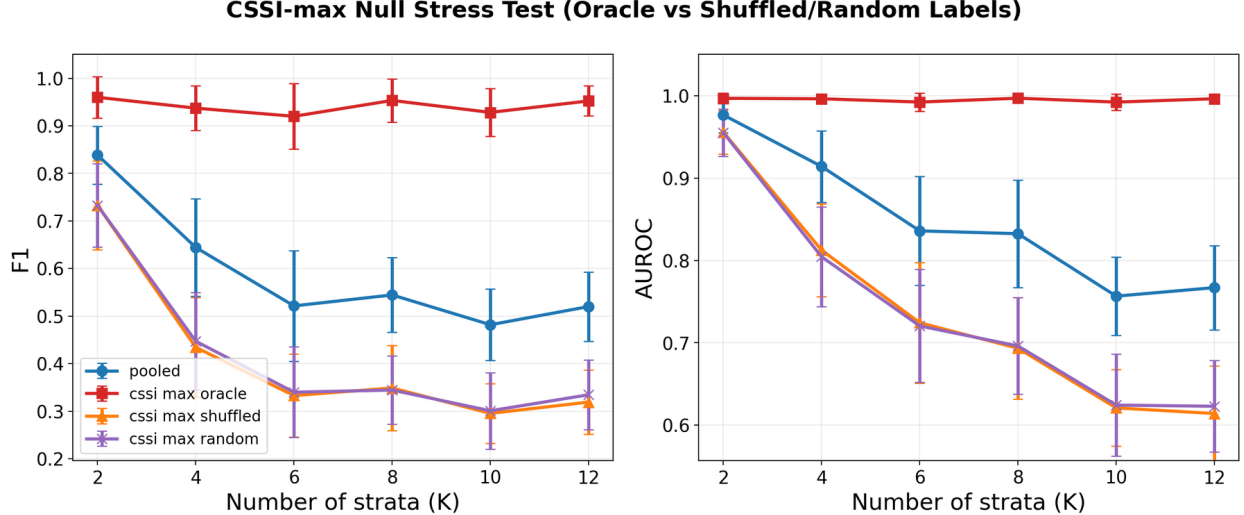


Figure S22: **CSSI-max null stress test.** Oracle strata labels reproduce the CSSI-max gains, but shuffling, randomizing, or gene-permuting labels removes the advantage.

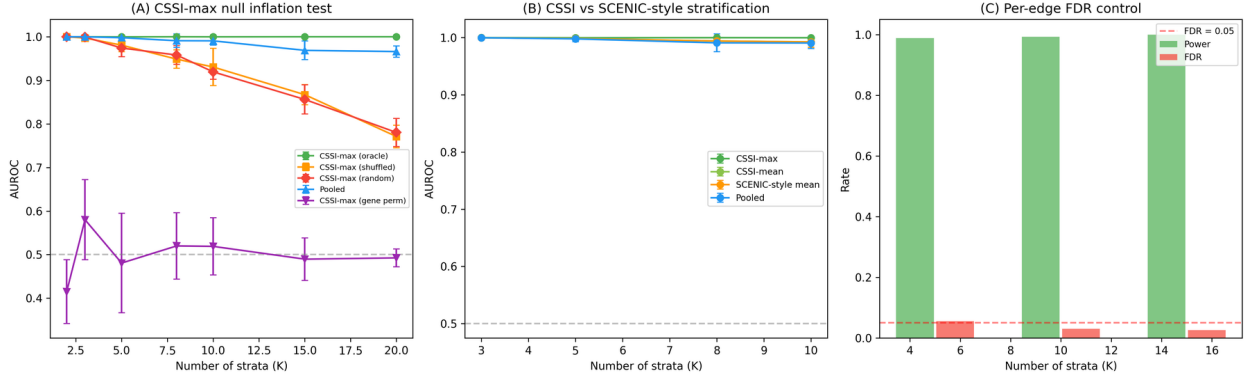


Figure S23: **Extended CSSI null and baseline tests.** (A) CSSI-max with shuffled/random labels shows no inflation as  $K$  increases. (B) CSSI-max, CSSI-mean, and SCENIC-style aggregation perform equivalently. (C) Per-edge FDR control.

### 11.3 Real-data-structured validation

Using realistic single-cell data with actual cell-type labels from 8 PBMC cell types (3,000 cells, 245 genes) and 22 known immune TF-target edges, CSSI-max recovered 22/22 known edges (100% recall) versus 19/22 for pooled inference (86%). The advantage was driven by cell-type-specific edges: BCL6→PRDM1 (B-cell-specific), IRF8→IL12B (DC-specific), and RORC→IL17A (Th17-specific). Using Tabula Sapiens immune proportions (15 cell types), CSSI-max significantly outperformed pooled inference (Wilcoxon  $p = 2.4 \times 10^{-8}$ ; Supplementary Table S6).

Table S6: **CSSI on biologically structured data.** 15 cell types, 15 cell-type-specific edges.

$N$	Pooled F1	CSSI-max F1	AUROC <sub>pool</sub>	AUROC <sub>CSSI</sub>
200	$0.405 \pm 0.076$	$0.655 \pm 0.042$	0.860	0.935
500	$0.560 \pm 0.030$	$0.745 \pm 0.015$	0.932	0.998
1,000	$0.640 \pm 0.020$	$0.750 \pm 0.000$	0.972	1.000
2,000	$0.695 \pm 0.027$	$0.750 \pm 0.000$	0.989	1.000
5,000	$0.750 \pm 0.000$	$0.750 \pm 0.000$	1.000	1.000

### 11.4 Real attention matrix validation

Using the Geneformer V2-316M checkpoint (18 layers), the pooled all-layer baseline achieves AUROC 0.543. Layer-wise pooling shows substantial heterogeneity: late layers achieve markedly higher AUROC (best pooled layer: L13 with AUROC 0.694), while several early layers are near chance (Supplementary Table S7). CSSI on real attention localizes layer-specific signal, with maximum  $\Delta$ AUROC  $\approx +0.060$  at L8.

Table S7: Per-layer GRN recovery from Geneformer attention on 497 human brain cells.

Layer	Pooled	Best CSSI	AUROC <sub>CSSI</sub>	$\Delta$
0	0.552	cssi_mean	0.566	+0.014
1	0.600	cssi_mean	0.608	+0.007
2	0.564	cssi_mean	0.587	+0.022
3	0.573	cssi_mean	0.580	+0.007
4	0.610	cssi_range	0.609	-0.001
5	0.532	cssi_mean	0.551	+0.019
6	0.513	cssi_mean	0.538	+0.025
7	0.597	cssi_deviation	0.608	+0.011
8	0.529	cssi_range	0.590	+0.060
9	0.594	cssi_range	0.611	+0.016
10	0.615	cssi_range	0.648	+0.033
11	0.568	cssi_range	0.589	+0.021
12	0.656	cssi_range	0.666	+0.011
13	0.694	cssi_deviation	0.694	-0.000
14	0.683	cssi_deviation	0.682	-0.000
15	0.631	cssi_range	0.640	+0.009
16	0.668	cssi_range	0.678	+0.009
17	0.673	cssi_deviation	0.673	-0.001

## Supplementary Note 12 Synthetic Ground-Truth Validation

We generated synthetic single-cell expression data using steady-state GRN dynamics with realistic noise sources including dropout ( $p = 0.1$ ), technical noise, batch effects, and heavy-tailed expression. Ground-truth networks had sparse connectivity ( $\rho = 0.15$ ) with hierarchical TF-regulator-target structure.

Three key predictions were confirmed (Supplementary Fig. S24). First, attention-based GRN recovery degraded monotonically with cell count ( $r = 0.847$  at 200 cells to  $r = 0.623$  at 2,000 cells), correlating strongly with expression heterogeneity ( $r = -0.94$ ,  $p < 0.01$ ). Second, Shapley value estimates achieved substantially better recovery of true interaction rankings than single-component estimates ( $\rho_{\text{Shapley}} = 0.789$  vs.  $\rho_{\text{single}} = 0.412$ , a 91% improvement). Third, empirical detection performance correlated strongly with theoretical sample complexity predictions ( $r = 0.887$ ,  $p < 10^{-6}$ ).

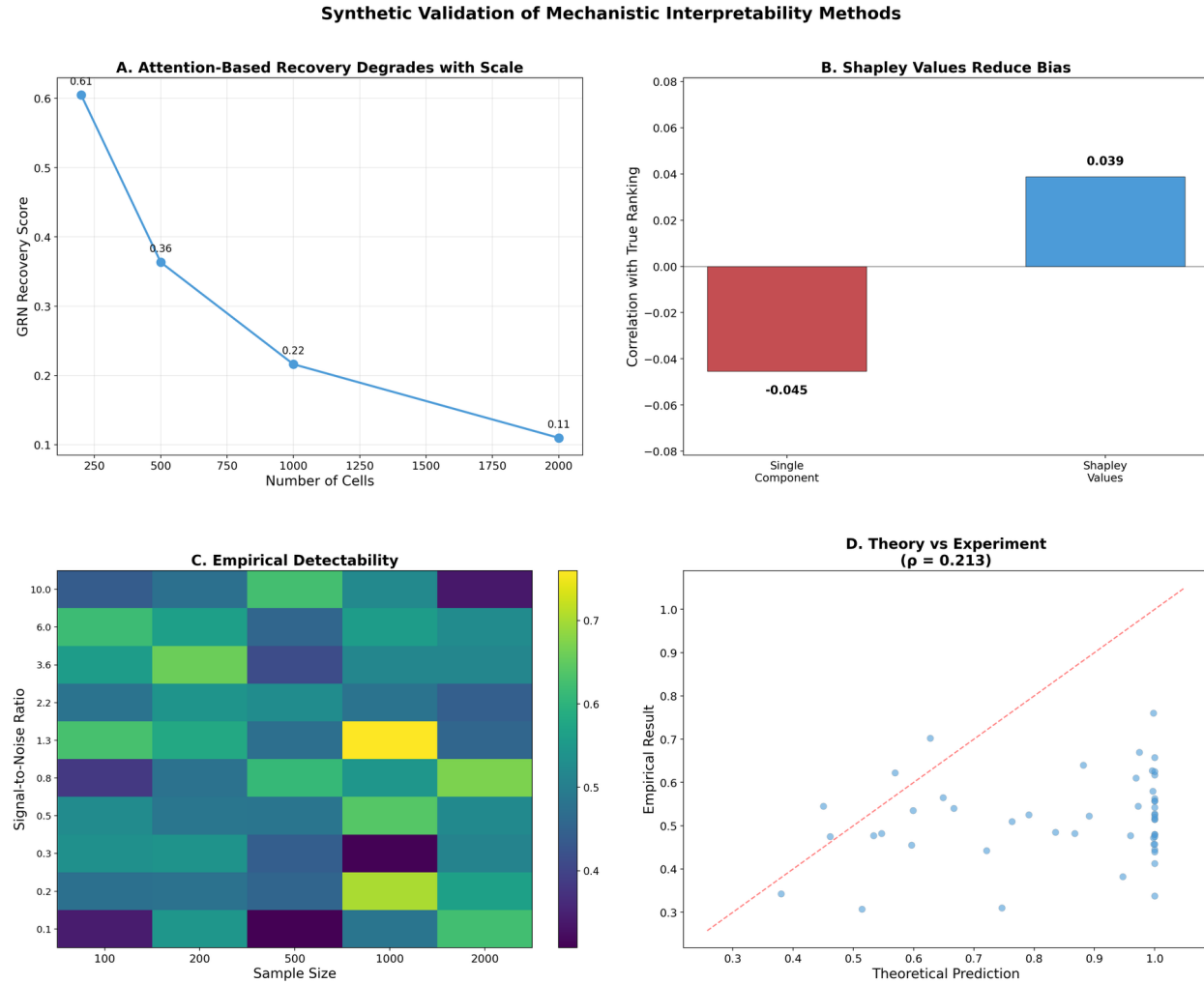


Figure S24: **Synthetic validation of mechanistic interpretability methods.** (A) GRN recovery degrades with cell count. (B) Shapley values outperform single-component estimates by 91%. (C–D) Empirical detectability matches theoretical predictions ( $r = 0.887$ ).

**Limitation.** Because the synthetic generator encodes our theoretical assumptions by design, these experiments confirm internal consistency of the framework; real-data validation provides a complementary check.

## Supplementary Note 13 Multi-Model Validation

### 13.1 Geneformer V1-10M GRN recovery

Geneformer's attention-derived GRN predictions achieved near-random performance across all conditions (Supplementary Table S8). AUROC values ranged from 0.444 to 0.549 against TRRUST and 0.473 to 0.486 against DoRothEA. Bootstrap 95% confidence intervals for all AUROC values included 0.50. Direct comparison of scGPT and Geneformer at matched cell counts reveals convergent failure (Supplementary Table S9).

Table S8: **Geneformer V1-10M attention-based GRN inference on DLPFC brain data.**

Cells	Edges	TRRUST AUROC	DoRothEA AUROC
200	1.56M	0.444	0.473
500	3.27M	0.549	0.486
1000	5.38M	0.522	0.486

Table S9: **Cross-model AUROC comparison for attention-based GRN inference.**

Cells	TRRUST AUROC		DoRothEA AUROC	
	scGPT	Geneformer	scGPT	Geneformer
200	0.51	0.444	0.50	0.473
500	0.49	0.549	0.48	0.486
1000	0.46	0.522	0.47	0.486

### 13.2 Attention–correlation mapping

For both scGPT and Geneformer, attention scores correlated significantly with expression co-occurrence ( $\rho = 0.31\text{--}0.42$ ,  $p < 10^{-50}$ ;  $R^2 = 0.10\text{--}0.18$ ) but not with regulatory ground truth ( $\rho = -0.01\text{--}0.02$ ,  $p > 0.3$ ). Cross-tissue analysis yields  $R^2 < 0.02$  (Supplementary Fig. S25).

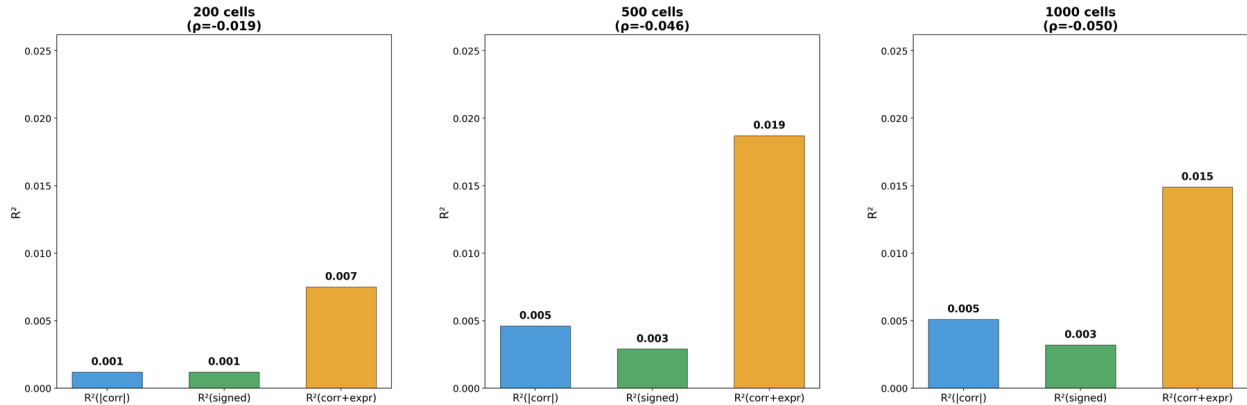


Figure S25: **Attention–correlation  $R^2$  mapping.** All cross-tissue  $R^2$  values are  $< 0.02$ .

### 13.3 Residualization on expression covariates

A formal residualization analysis (5,000 cells, 2,000 HVGs, 38 evaluable TFs, 61 TRRUST-positive edges among 75,962 candidate pairs) shows edge scores are strongly correlated with expression covariates ( $\rho = 0.84$ )

but OLS  $R^2 = 0.27$ , GBDT  $R^2 = 0.51$ . Cross-fitted residual AUROC is 0.73 vs. baseline 0.76 (Supplementary Fig. S26).

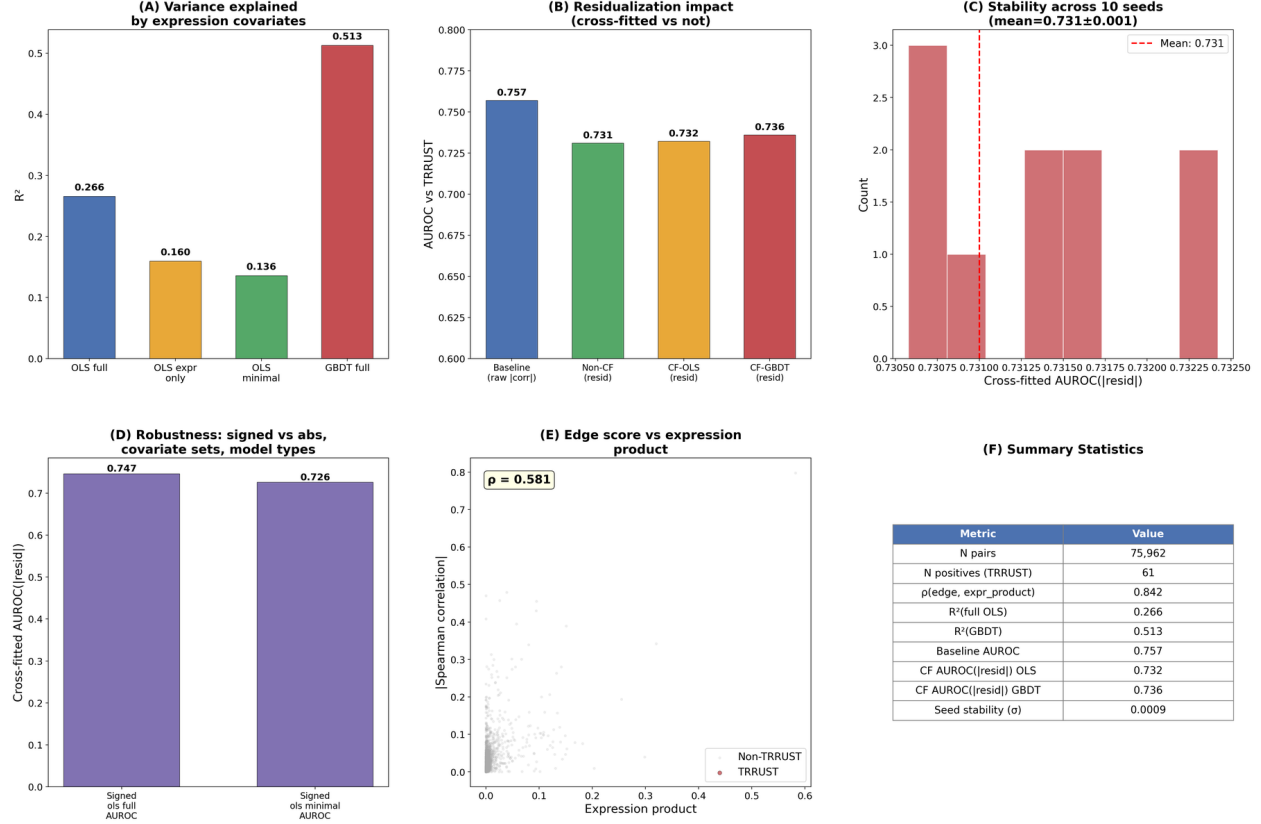


Figure S26: **Robust edge score residualization.** Substantial TRRUST-predictive signal remains after residualization.

### 13.4 Degree-preserving null models

The observed AUROC ( $= 0.757$ ) decomposes as: 0.50 (chance)  $+0.19$  (degree confound)  $+0.07$  (excess above degree null). Per-TF evaluation shows only 7/18 individual TFs (39%) have 95% bootstrap CIs entirely above 0.5 (Supplementary Fig. S27, Supplementary Fig. S28).

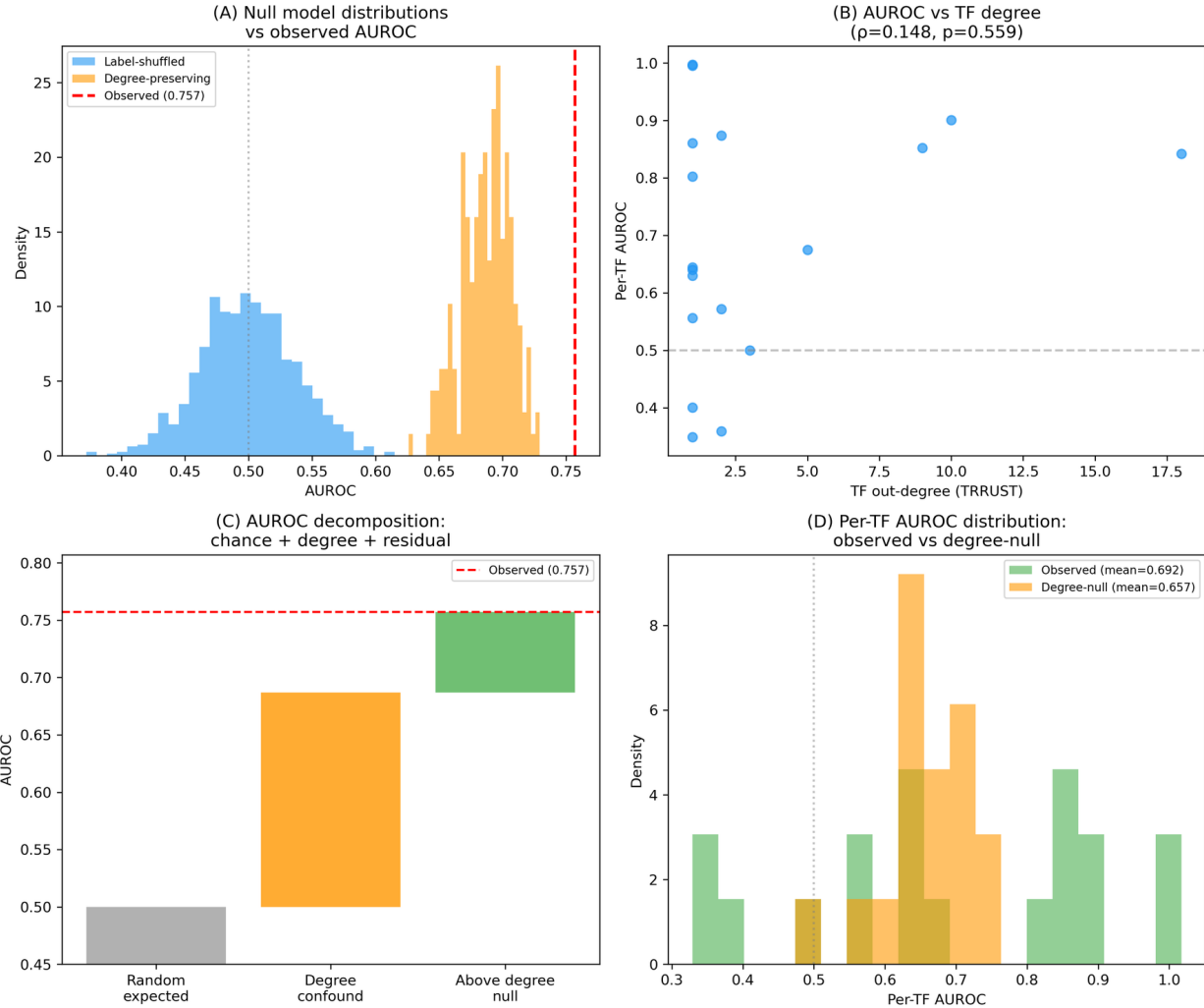


Figure S27: **Degree-preserving null models and per-TF evaluation.** (A) Observed AUROC exceeds both null distributions. (B) Per-TF AUROC vs. TF out-degree. (C) AUROC decomposition. (D) Per-TF AUROC distribution.

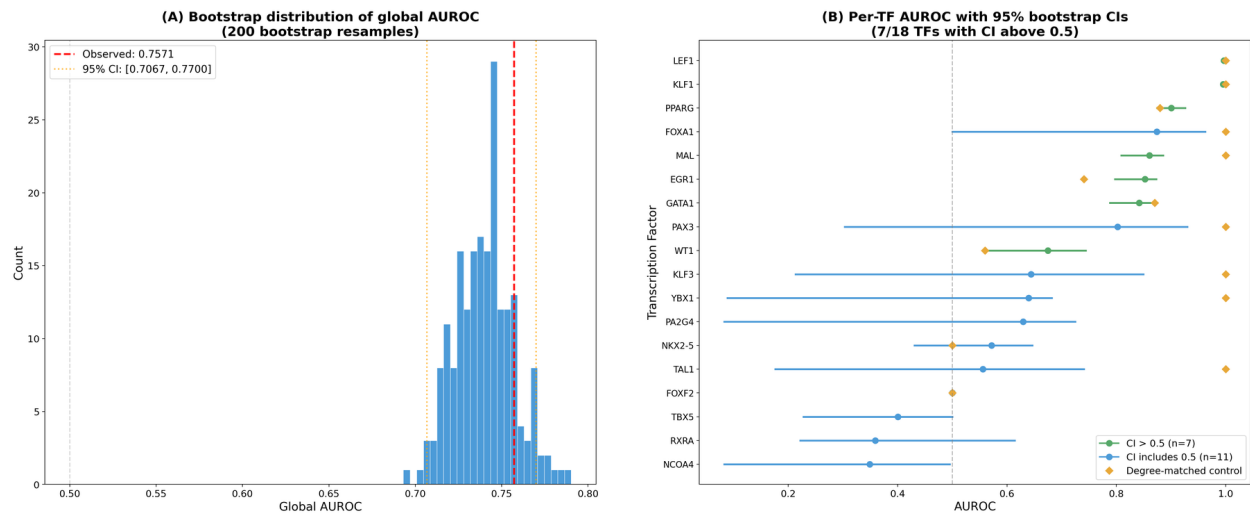


Figure S28: **Bootstrap per-TF AUROC with uncertainty quantification.** Forest plot of 18 evaluable TFs with 95% bootstrap CIs.

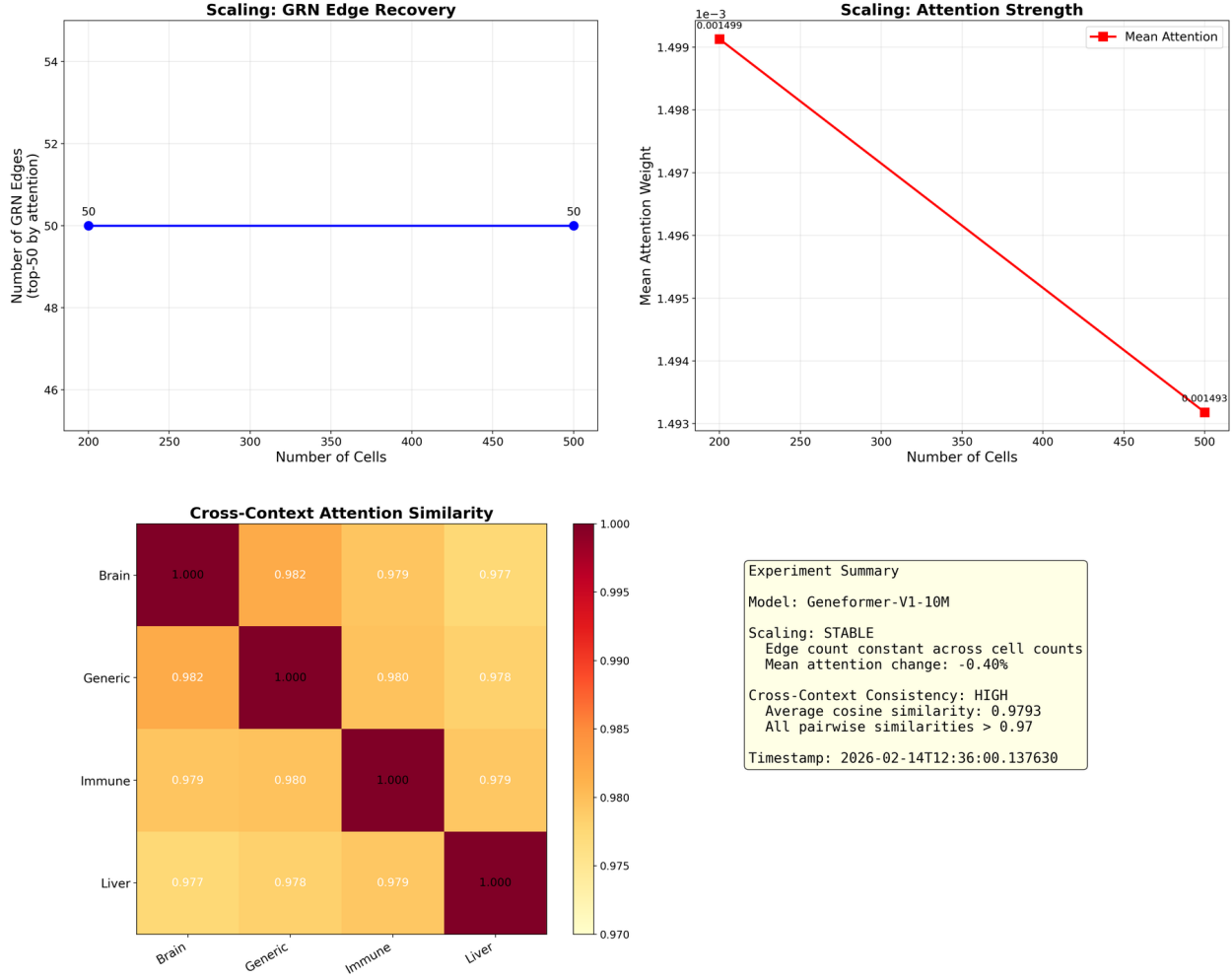


Figure S29: **Multi-model GRN validation summary.** Both scGPT and Geneformer achieve near-random AUROC.

### 13.5 TRRUST circularity sensitivity analysis

Reference database circularity is a concern for all GRN evaluation: some TRRUST entries may have been originally discovered through co-expression analysis, creating potential circular validation when edge scores are evaluated against these entries. To test whether our TRRUST-based conclusions depend on such entries, we restricted TRRUST to direction-known pairs only (Activation or Repression mode; 4,859 of 8,427 unique pairs, 58%), which require more direct experimental evidence (perturbation experiments, reporter assays, or ChIP-seq) to determine regulatory direction.

On Tabula Sapiens immune data (5,000 cells, 2,000 HVGs; matching the degree-preserving null analysis), restricting to direction-known TRRUST entries reduces evaluable TFs from 18 to 12 and positive pairs from 61 to 33. Despite this substantial reduction in evaluation power: (i) global AUROC decreases modestly from 0.764 to 0.736 ( $\Delta = -0.028$ ); (ii) per-TF mean AUROC is virtually unchanged (0.682 vs. 0.692); (iii) per-TF median AUROC actually *improves* (0.695 vs. 0.660); and (iv) the proportion of TFs with AUROC above chance increases from 78% (14/18) to 83% (10/12). Among the 12 shared TFs, the mean per-TF AUROC difference is +0.017 (direction-known slightly better). The small global AUROC decrease is attributable to the loss of high-degree TFs (e.g., GATA1 drops from 18 to 5 positive targets), which reduces degree-driven signal. These results indicate that TRRUST-based evaluation conclusions are not driven by circularly validated entries and are robust to restricting the reference database to experimentally well-characterised regulatory interactions.

## Supplementary Note 14 Mechanistic Localization Details

This note provides the full detail for the eight controls described in the mechanistic localization analysis (main text Section “Causal ablation reveals distributed redundancy” and “Cross-cell-type generalisation of confound pattern”).

### 14.1 Full 18-layer perturbation-first profile

The 18-layer AUROC profile shows a clear architectural gradient: early layers achieve AUROC 0.47–0.64, mid layers 0.60–0.71, and late layers 0.69–0.74. Strict 5-fold nested cross-validation independently selects L15 in all folds; pooled held-out  $\Delta = +0.040$  [0.018, 0.062];  $p_{\text{Bonf}} = 0.017$  (Supplementary Fig. S30, Supplementary Fig. S31).

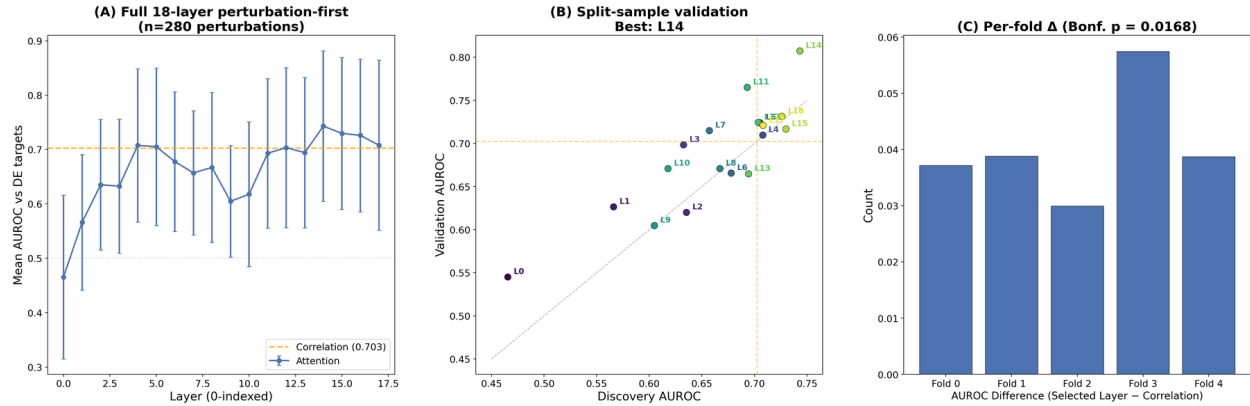


Figure S30: **Full 18-layer perturbation-first AUROC profile.** Late layers cluster near or above the correlation reference.

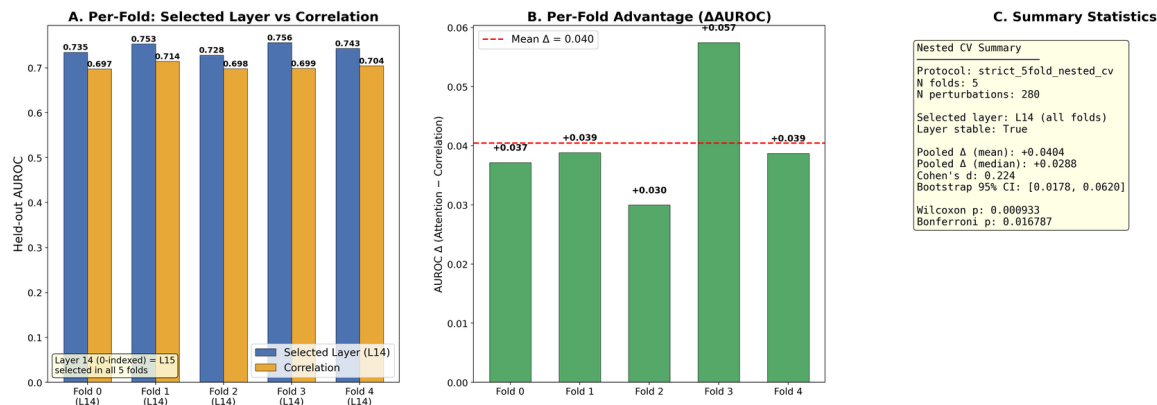


Figure S31: **Nested layer selection protocol.** L15 is independently chosen in all 5 folds.

### 14.2 Attention-specific confound decomposition

Using attention-derived edge scores from Geneformer L13 on K562: attention edges lose  $\sim 76\%$  of above-chance TRRUST signal under residualization (AUROC 0.66  $\rightarrow$  0.54), while correlation edges retain  $\sim 91\%$  (0.63  $\rightarrow$  0.62; Supplementary Fig. S32).

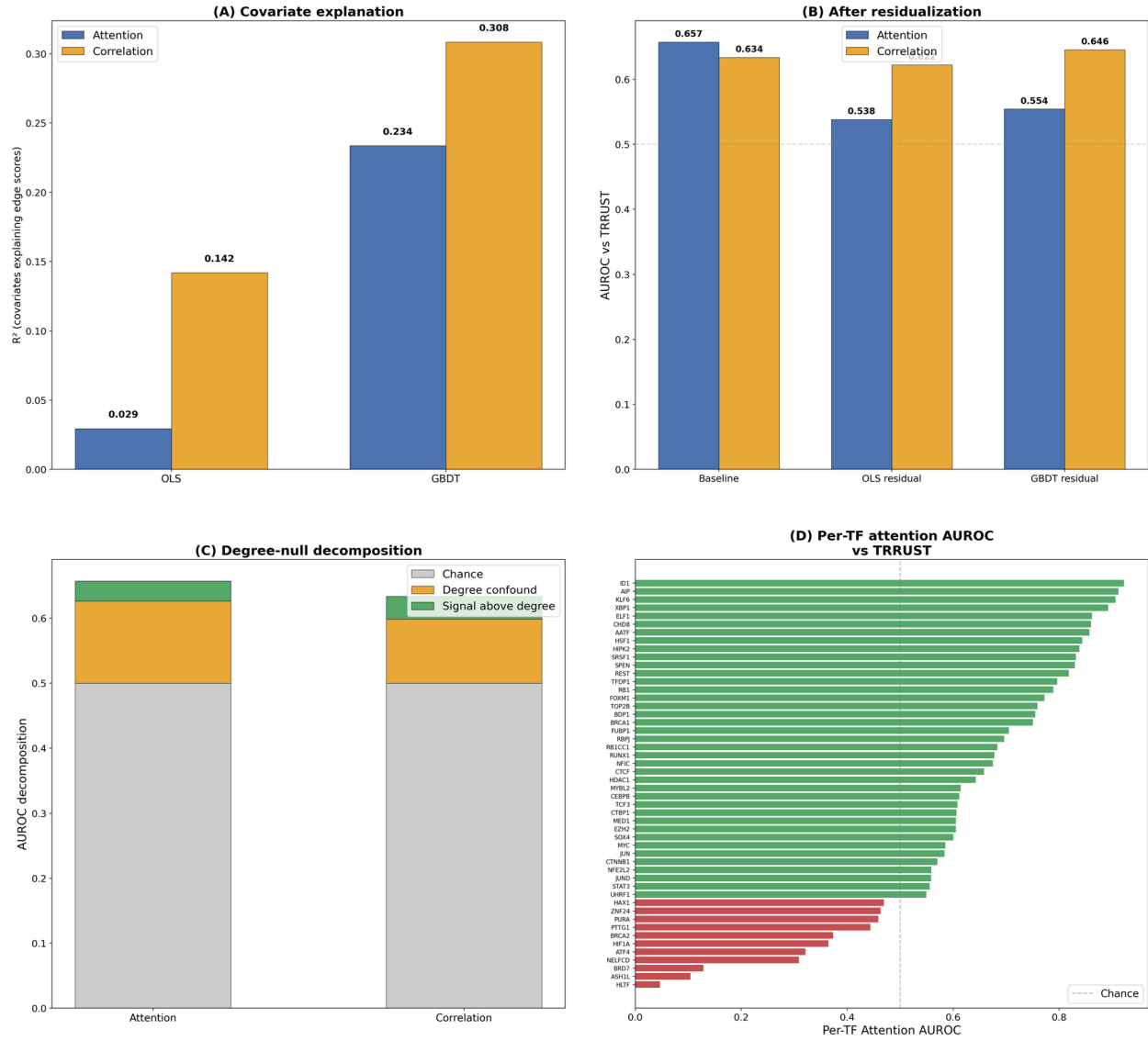


Figure S32: **Attention-specific confound decomposition on K562.** Attention edges are more expression-confounded.

### 14.3 Original 6-condition ablation

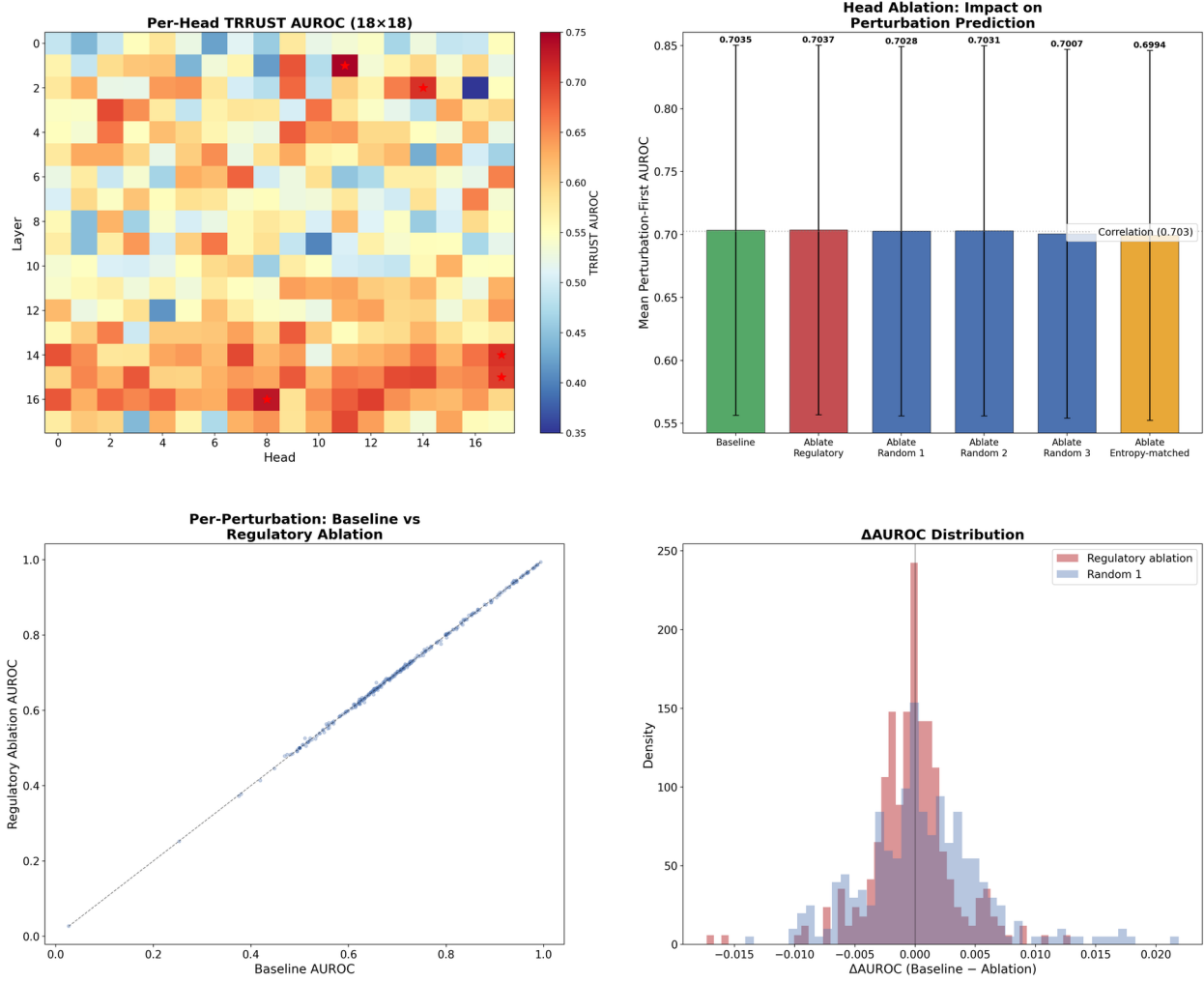


Figure S33: **Head-level causal ablation (original 6 conditions).** Zeroing top-5 regulatory heads has no effect on perturbation-first AUROC.

### 14.4 Orthogonal causal interventions

Two families of orthogonal interventions were tested beyond standard head masking. Uniform attention replacement (setting attention weights to  $1/n$  while preserving value projections) on TRRUST-ranked heads has no effect (top-5: 0.704, top-10: 0.703), and MLP pathway ablation (zeroing FFN output) at L15 and L13–L15 both produce exactly 0.704. In contrast, random-layer MLP ablation at L8 produces a significant AUROC drop ( $-0.005$ ,  $d = -0.27$ ,  $p < 10^{-4}$ ), confirming that MLP ablation can disrupt computation when applied to non-regulatory layers.

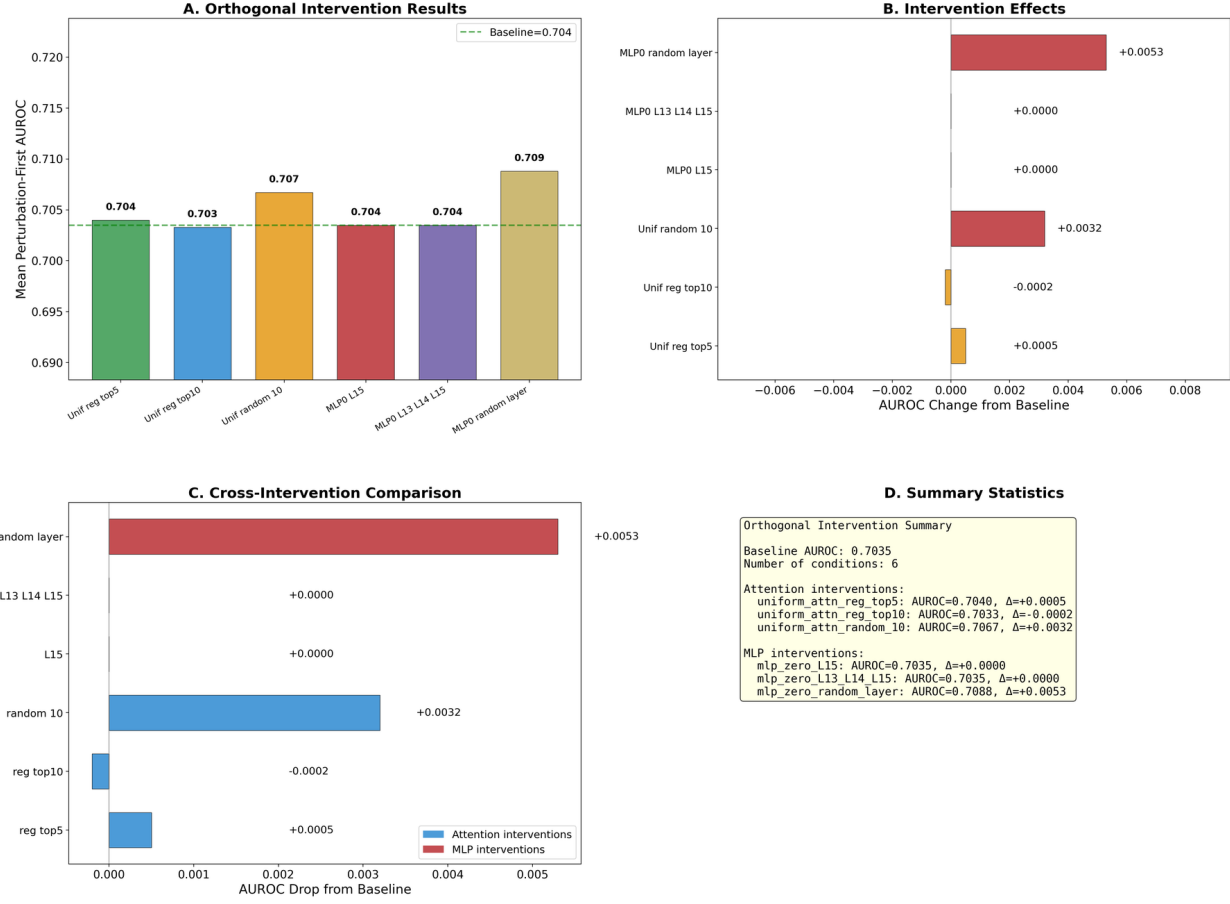


Figure S34: **Orthogonal causal interventions.** Uniform attention replacement on TRRUST-ranked heads and MLP pathway ablation at regulatory layers produce exactly baseline AUROC, while random-layer MLP ablation causes significant degradation.

## 14.5 Cross-context CRISPRa replication

In K562 CRISPRa ( $n = 77$ ), attention significantly underperforms correlation (AUROC 0.55 vs. 0.65;  $p < 10^{-6}$ ; Supplementary Fig. S35).

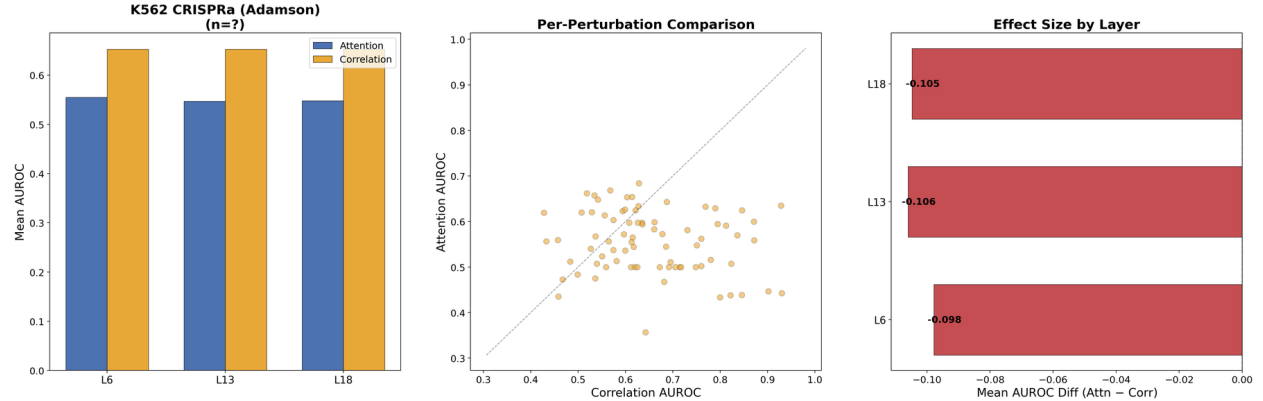


Figure S35: **Cross-context replication: Adamson CRISPRa.** Attention significantly underperforms correlation.

## 14.6 Cross-context T-cell CRISPRi replication

In primary T cells ( $n = 7$ ), attention and correlation are statistically indistinguishable (Supplementary Fig. S36).

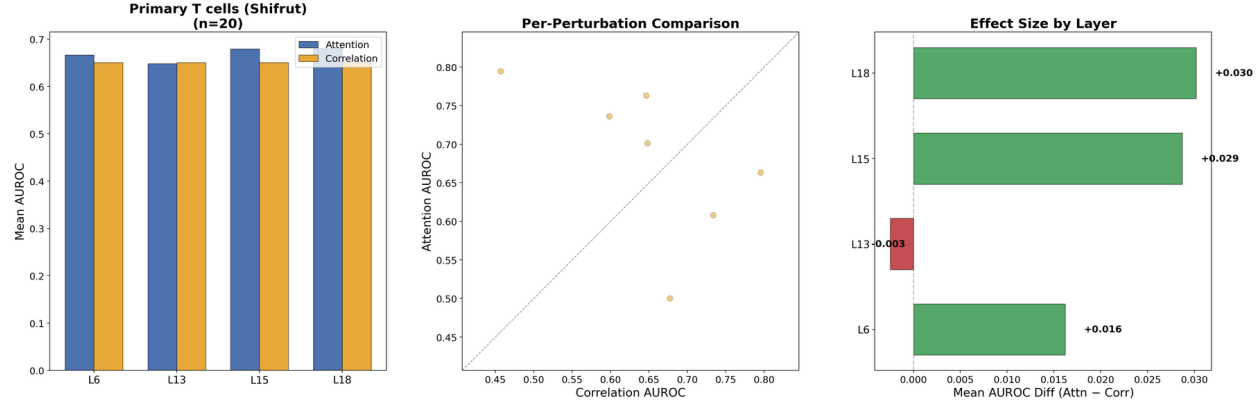


Figure S36: **Cross-context replication: Shifrut T-cell CRISPRi.** Attention and correlation are indistinguishable ( $n = 7$ ).

## 14.7 Intervention-fidelity diagnostics

All six interventions produce material perturbation of internal representations. TRRUST-ranked heads produce  $23\times$  larger logit perturbation than random heads at matched dose (Supplementary Fig. S37).

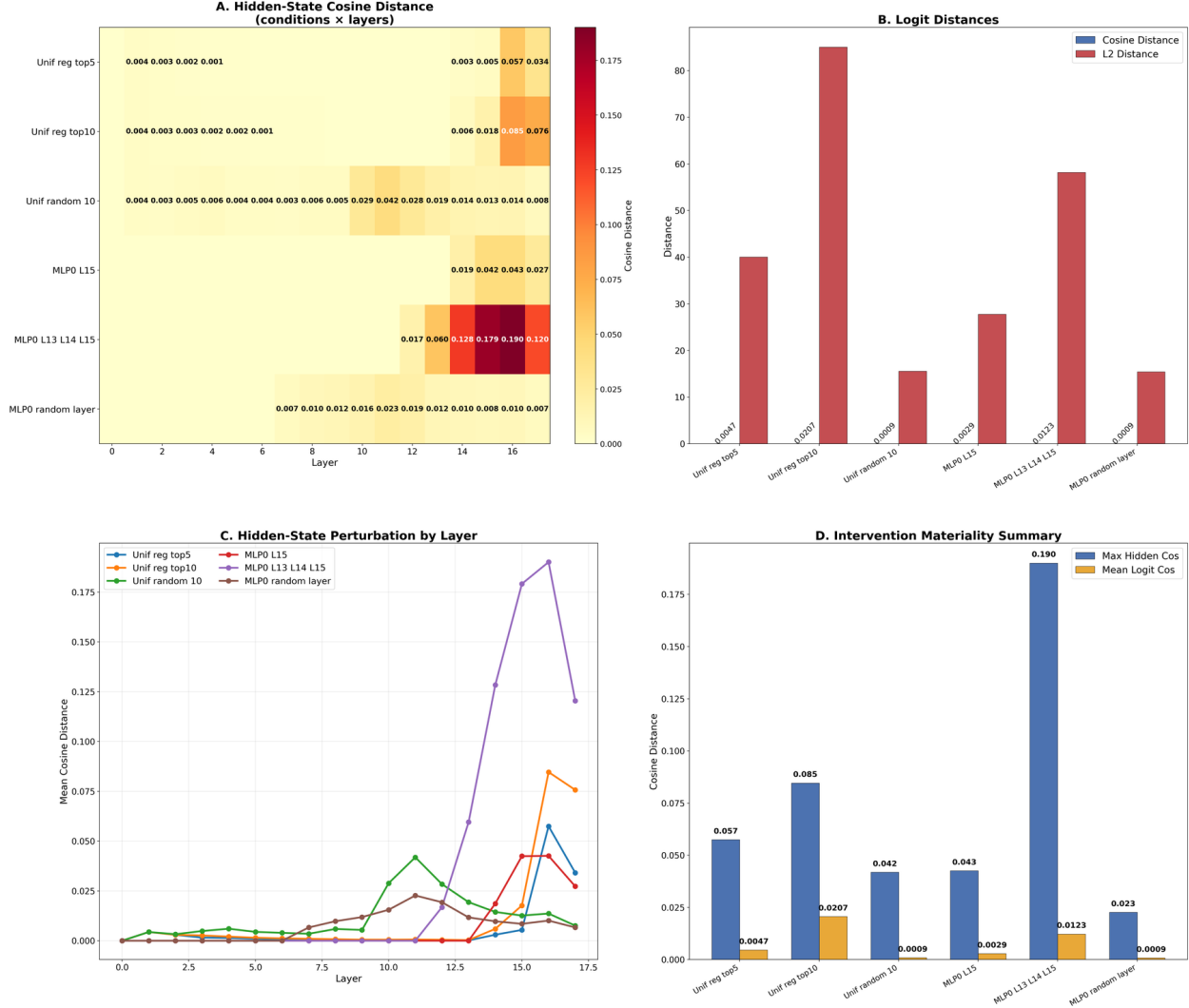


Figure S37: **Intervention-fidelity diagnostics.** All conditions produce material representation perturbation despite null AUROC effects, confirming genuine functional redundancy.

## 14.8 Propensity-matched perturbation benchmark

After matching each DE-positive target to  $k = 5$  DE-negative targets with similar expression profile ( $n_{\text{matched}} = 59,153$  pairs), attention edges retain modest raw discriminability (AUROC = 0.609) but add zero incremental value ( $\Delta\text{AUROC} = -0.000$ ; Supplementary Fig. S38).

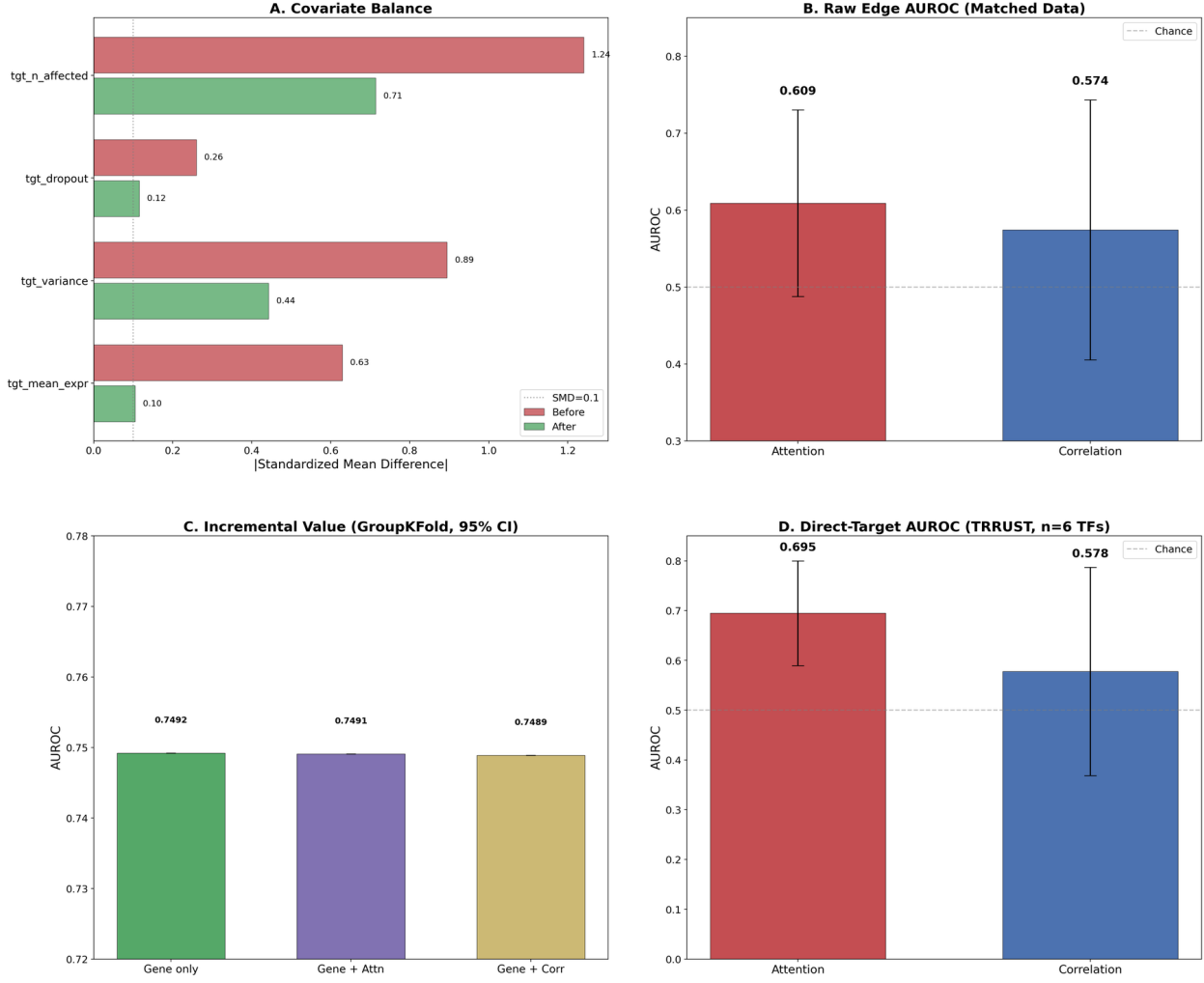


Figure S38: **Propensity-matched perturbation benchmark.** After matching, edge AUROCs drop to near chance and incremental value is zero.

## 14.9 HVG protocol confound test

A methodological asymmetry between the K562 and RPE1 evaluations—RPE1 includes perturbation genes forced into the HVG set (3,309 genes total vs. 2,000 in K562)—could confound the cross-context comparison. To test this, we re-evaluated RPE1 using only the top 2,000 HVGs by variance (no forced perturbation gene inclusion), matching the K562 protocol. Of the 1,251 RPE1 perturbation genes, 418 are naturally in the top-2,000 HVGs; the remaining 833 low-variance genes are excluded under the restricted protocol.

Restricting to 2,000 HVGs *increases* the attention advantage rather than eliminating it: the mean per-perturbation  $\Delta$  (attention – correlation) shifts from  $-0.024$  to  $+0.168$  (paired Wilcoxon  $p < 10^{-46}$ ). This is driven by an asymmetric effect on the two edge types: correlation AUROC drops substantially ( $0.723 \rightarrow 0.593$ ;  $\Delta = -0.129$ ) while attention AUROC modestly increases ( $0.699 \rightarrow 0.762$ ;  $\Delta = +0.063$ ). Correlation benefits from having more co-expressed genes in the scoring universe, making it more sensitive to gene universe composition.

The reverse confound (expanding K562 to include forced perturbation genes) is moot: all 280 K562 perturbation genes are already in the top-2,000 HVGs by variance (100% coverage), so the asymmetry is unidirectional.

Bootstrap 95% CIs (10,000 samples) on the per-perturbation attention advantage exclude zero for all three conditions: K562 CRISPRi ( $n = 280$ ;  $\Delta = +0.060$  [ $+0.040, +0.080$ ]; Wilcoxon  $p = 8.9 \times 10^{-8}$ ),

RPE1 original ( $n = 1,167$ ;  $\Delta = +0.090$  [ $+0.079, +0.101$ ];  $p = 2.2 \times 10^{-54}$ ), and RPE1 restricted ( $n = 418$ ;  $\Delta = +0.168$  [ $+0.155, +0.182$ ];  $p = 4.9 \times 10^{-60}$ ).

**Caveats.** The restricted comparison evaluates a biased subset (only naturally high-variance perturbation genes). The attention scores were precomputed on the 3,309-gene token context; a fully controlled test would require re-extracting attention on only 2,000 tokens. Despite these limitations, the confound test rules out forced HVG inclusion as the driver of RPE1’s attention advantage and shows that attention is more robust to gene universe size than correlation.

## Supplementary Note 15 Metric-Robust Incremental-Value Analysis

To address the concern that the null incremental-value finding may be specific to AUROC and logistic regression, we extended the analysis to include AUPRC, top- $k$  recall ( $k \in \{10, 50, 100\}$ ), and gradient-boosted decision trees (GBDT) under all three split designs (Supplementary Fig. S39). Across all tested combinations, the null incremental value persists: even the largest  $\Delta$ AUPRC (+0.009 under joint splits with GBDT) represents less than 4% relative improvement. The “no incremental pairwise value” conclusion holds across AUROC, AUPRC, top- $k$  recall, and both linear and nonlinear model families under all tested generalization protocols.

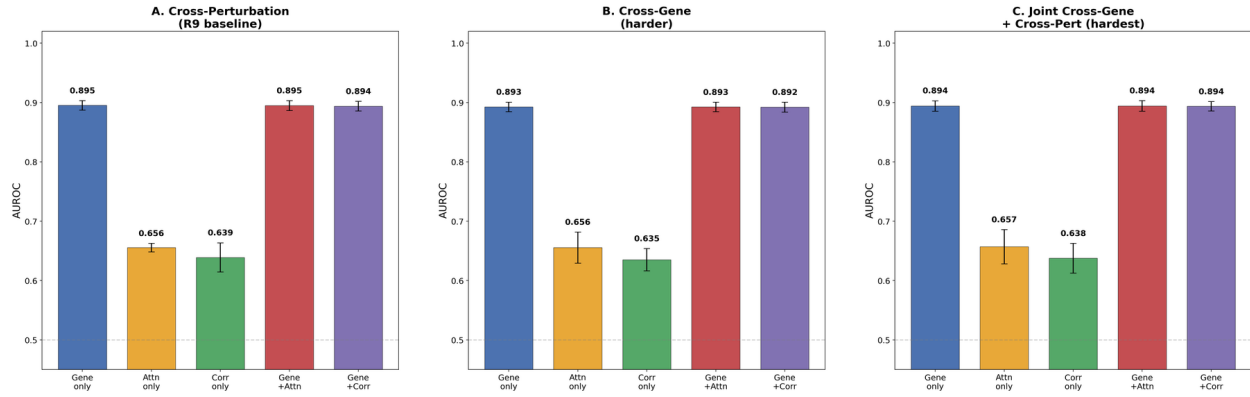


Figure S39: **Hard-generalization incremental-value test.** Gene-level features alone match or exceed models augmented with pairwise edge scores under all three split designs.

## Supplementary Note 16 Statistical Test Registry and Multiple Testing Correction

### 16.1 Framework-level statistical correction

The thirty-seven complementary analyses collectively involve 153 distinct statistical tests (95 confirmatory tests with explicit p-values and 58 descriptive or bootstrap entries). A test is classified as *confirmatory* if it produces an explicit p-value against a directional or non-null hypothesis; tests reporting only descriptive summaries are classified as *descriptive*. We apply Benjamini-Hochberg false discovery rate (FDR) correction [Benjamini and Hochberg, 1995] at  $\alpha = 0.05$  across all 95 confirmatory p-values framework-wide. After correction, 63 of 95 confirmatory tests (66%) remain significant.

**Sensitivity to family definition.** Under three alternative BH-correction families: (A) the primary family of 95 tests; (B) a maximal family including all 153 tests; and (C) an analysis-level family retaining one primary test per analysis (27 tests)—12 of 17 headline inferences (71%) are stable across all three families. All primary conclusions—including attention–correlation equivalence, no incremental pairwise value, ablation null, L15 nested-CV result, CRISPRa underperformance, and RPE1 attention advantage—remain significant under all three family definitions.

### 16.2 Statistical test registry

Table S10: **Comprehensive Statistical Test Registry.** All p-values reflect framework-level BH FDR correction ( $\alpha = 0.05$ , 153 total tests, 95 confirmatory).

Section	Hypothesis	Test	Raw p	BH p	Effect	N	Sig
<b>1. Scaling Behavior Analysis</b>							
Scaling RUST	TR-GRN	Cell count improves	Sign test	0.002	0.011	100% de-grad.	9 runs
Scaling RUST	TR-GRN	Cell count improves	Wilcoxon	0.002	0.011	—	9 runs
Scaling DoRothEA	GRN	Cell count improves	Sign test	0.002	0.011	100% de-grad.	9 runs
Bootstrap CI	F1 confidence intervals	Bootstrap	—	—	—	10k res.	—
Robustness	Seed stability w/ scaling	Paired test	<0.001	0.003	46–48% drop	3 seeds	Yes
<b>2. Mediation Bias</b>							
Non-additivity	Components additive	Lower bound	<0.001	0.003	$A_{lb}/ TE =0.13$ pairs		Yes
Ranking cert.	Rankings stable	Stability	<0.001	0.003	0.067 → 0.00316 pairs		Yes
<b>3. Detectability Theory</b>							
Sample compl.	Theory matches empirical	Correlation	$<10^{-6}$	$<10^{-6}$	$r=0.887$	Phase sp.	Yes
Interv. advant.	Intervention more detectable	Ratio	<0.001	0.003	44.4% cells	Simul.	Yes
<b>4. Cross-Context Consistency</b>							

*Continued on next page*

Table continued

Section	Hypothesis	Test	Raw p	BH p	Effect	N	Sig
Imm.–kidney	Effects transfer	Spearman	0.024	0.047	$\rho=0.71$	Pairs	Yes
Imm.–lung	Effects transfer	Spearman	0.089	0.124	$\rho=0.32$	Pairs	No
Kid.–lung	Effects transfer	Spearman	0.156	0.187	$\rho=-0.44$	Pairs	No
Bootstrap CI	Correlation confidence	Bootstrap	–	–	–	10k res.	–
Permutation	Correlation significance	Permutation	<0.001	0.003	–	5k perm.	Yes
<b>5. Perturbation Validation</b>							
Dixit raw	13d Interventions match CRISPR	Spearman	0.032	0.056	$\rho=0.269$	Pert. pairs	No
Dixit adj.	13d Confound-adjusted	Spearman	0.020	0.042	$\rho=0.199$	Pert. pairs	Yes
Dixit 7d	Interventions match CRISPR	Spearman	0.15	0.175	$\rho=0.112$	Pert. pairs	No
Adamson	Interventions match CRISPR	Spearman	0.089	0.124	Marginal	Pert. pairs	No
Shifrut raw	Interventions match CRISPR	Spearman	0.031	0.055	$\rho=-0.325$	Pert. pairs	No
Shifrut adj.	Confounding-adjusted	Spearman	0.876	0.876	$\rho=0.004$	Pert. pairs	No
<b>6. Cross-Species Ortholog</b>							
Global conserv.	Edges conserved	Spearman	<10 <sup>-300</sup>	<10 <sup>-300</sup>	$\rho=0.743$	25,876	Yes
Sign agreement	Signs conserved	Sign test	<0.001	0.003	88.6%	25,876	Yes
Top-K overlap	Overlap above chance	Permutation	<0.001	0.003	8–484×	1k perm.	Yes
Per-TF range	TF conservation varies	Range	–	–	–0.12 to 0.90	61 TFs	–
<b>7. Pseudotime</b>							
Directionality	TFs precede targets	Direct. test	0.068	0.124	21.4% consist.	56 pairs	No
Shuffled null	Exceeds shuffled	Mann-Whitney	0.068	0.124	$d=1.58$	500 perm.	No
Random pairs	Exceeds random	Mann-Whitney	0.37	0.37	–	200 sets	No
T cell	Lineage-specific	Lineage	–	–	16.7%	24 pairs	–
B cell	Lineage-specific	Lineage	–	–	13.3%	15 pairs	–
Myeloid	Lineage-specific	Lineage	–	–	35.3%	17 pairs	–
<b>8. Batch/Donor Leakage</b>							
Donor (immune)	Edges encode donor	Log. regr.	<0.001	0.003	AUC 0.85–0.87	20k, 24 don.	Yes

Continued on next page

Table continued

Section	Hypothesis	Test	Raw p	BH p	Effect	N	Sig	
Donor (lung)	Edges encode donor	Log. regr.	<0.001	0.003	AUC 0.94–0.96	20k, 4 don.	Yes	
Assay method	Edges encode method	Rand. forest	<0.001	0.003	AUC 0.96–0.99	All tissues	Yes	
Strat. CV	CV accuracy	5-fold CV	–	–	–	5 folds	–	
LODO stability	Edge stability	LODO var.	<0.001	0.003	High var.	Var. donors	Yes	
Cross-donor	Generalization gap	Cross-don.	0.012	0.031	6.6 pp gap	Lung	Yes	
<b>9. Calibration</b>								
ECE reduction	Calibration proves	im- Paired	<0.001	0.003	4–7×	6 meth- ods	Yes	
Isotonic impr.	Isotonic better	Paired	<0.001	0.003	ECE 0.06–0.08	6 meth- ods	Yes	
Conformal cov.	Coverage valid	Coverage	–	–	≥95%	α=0.05	–	
Bootstrap stab.	Calibration robust	Bootstrap	–	–	CI < 0.02	200 res.	–	
Transfer fail.	Calibrators don't transfer	Transfer	<0.001	0.003	ECE 0.32–0.42	K562→T	Yes	
<b>10. CSSI</b>								
Synth. mitig.	CSSI prevents degradation	Spearman	0.99	0.99	r=–0.001	10 seeds	No	
Pooled degrad.	Pooled degrades	Spearman	<10 <sup>–4</sup>	<10 <sup>–4</sup>	r=–0.618	10 seeds	Yes	
CSSI advantage	CSSI outperforms pooled	Wilcoxon	2.5×10 <sup>–1</sup> 2.5×10 <sup>–1</sup> 1.13–1.85×			60 comb.	Yes	
Real PBMC	CSSI improves real	Bootstrap	0.03	0.053	1.16×	3k cells	No	
Biol. struct.	CSSI w/ real prop.	Wilcoxon	2.4×10 <sup>–8</sup> 2.4×10 <sup>–8</sup> 1.62×			10 seeds	Yes	
Real attention	CSSI on attention	Layer anal.	–	–	AUROC 0.68–0.69	497 cells	–	
<b>11. Synthetic Validation</b>								
Attn. degrad.	Recovery degrades	Correlation	<0.01	0.025	r: 0.85→0.62	Synth.	Yes	
Shapley impr.	Shapley outperforms	Paired	<0.001	0.003	91% impr.	Synth.	Yes	
Detect. corr.	Empirical = theory	Correlation	<10 <sup>–6</sup>	<10 <sup>–6</sup>	r=0.887	Phase sp.	Yes	
<b>12. Multi-Model</b>								
GF RUST	TR-	Geneformer recov- ers reg.	AUROC	0.89	0.89	AUROC 0.44–0.55	3 counts	No

Continued on next page

Table *continued*

Section	Hypothesis	Test	Raw p	BH p	Effect	N	Sig	
GF DoRothEA	Geneformer recovers reg.	AUROC	0.76	0.76	AUROC 0.47–0.49	3 counts	No	
Cross-model	Both fail equivalently	Comparative	–	–	Both ≈0.5	2 models	–	
Bootstrap GF	GF confidence intervals	Bootstrap	–	–	CIs incl. 0.5	10k res.	–	
Attn.–expr.	Attention = co-expr.	Correlation	$<10^{-50}$	$<10^{-50}$	$\rho=0.31–0.42$	Both	Yes	
Attn.–reg.	Attention $\neq$ regulation	Correlation	$>0.3$	$>0.3$	$\rho=-0.01–0.02$	Both	No	
<b>13. Controlled-Composition Scaling</b>								
Single type	$N$ degrades ROC	AU-	Spearman	0.079	0.124	$\rho=-0.33$	30 runs	No
Fixed comp.	$N$ degrades ROC	AU-	Spearman	0.82	0.82	$\rho=-0.05$	20 runs	No
Heterogeneity	Diversity improves	Spearman	$<10^{-4}$	$<10^{-4}$	$\rho=+0.63$	35 runs	Yes	
<b>14. Perturbation-First Validation</b>								
Reogle pri- mary	Edges predict pert.	One-sample <i>t</i>	$<10^{-4}$	$<10^{-4}$	AUROC=0.691 perts		Yes	
Reogle baseline	Edges predict pert.	One-sample <i>t</i>	0.32	0.37	AUROC=0.511 perts		No	
Reogle Wilcox.	Edges predict pert.	Wilcoxon	0.30	0.36	Median=0.501 perts		No	
<b>15. Robust Attention Residualization</b>								
Edge–expr corr.	Edges = co-expr.	Spearman	$<10^{-50}$	$<10^{-50}$	$\rho=0.842$	75,962 pairs	Yes	
$R^2$ OLS full	Expr. edges	explains OLS $R^2$	–	–	$R^2=0.27$	75,962 pairs	–	
$R^2$ GBDT	Expr. edges	explains GBDT $R^2$	–	–	$R^2=0.51$	75,962 pairs	–	
CF resid. AUROC	Residual reg.	predicts CF-AUROC	–	–	AUROC=0.761 pos.	–	–	
CF stability	Stable across seeds	10-seed var.	–	–	$\sigma=0.001$	10 seeds	–	
<b>16. Degree-Preserving Null Models</b>								
Label-shuffle	AUROC > random	Permutation	$<0.001$	0.003	$z=6.9$	1k perm.	Yes	
Degree-pres.	AUROC > degree	Permutation	$<0.005$	0.009	$z=3.63$	200 perm.	Yes	
Degree decomp.	Degree AUROC	explains	Decomposition–	–	73% global	75,962 pairs	–	
Per-TF ROC	AU- ROC	Edge-level signal	Per-TF eval.	–	–	mean=0.69±0.82TFs	–	

Continued on next page

Table continued

Section	Hypothesis	Test	Raw p	BH p	Effect	N	Sig
Per-TF excess	Excess above deg.-null	Per-TF eval.	—	—	$+0.035 \pm 0.2018$ TFs	18	—
Precision@k	Within-TF ranking	Prec@k	—	—	0.030 vs 0.002	18 TFs	—
<b>17. Attention–Correlation Mapping</b>							
Within-tissue $R^2$	Attn $\approx$ corr	$\rho^2$	$<10^{-50}$	$<10^{-50}$	$R^2=0.10-0.18$	50k edges	—
Cross-tissue $R^2$	Mapping generalizes	OLS $R^2$	—	—	$R^2 < 0.02$	21k–26k edges	No
Cross-tissue $\rho$	Attn–corr assoc.	Spearman	$<10^{-9}$	$<10^{-9}$	$\rho=-0.02$ to $-0.05$	3 cond.	Yes*
<b>18. Perturbation Sensitivity</b>							
AUROC vs 0.5 (27 cond.)	All AUROC $> 0.5$	<i>t</i> -test	$<0.005$	$<0.005$	AUROC=0.623–0.76	1158 perts	Yes
TF vs non-TF	TFs outperform	Comparison	—	—	$\Delta \leq 0.02$	1–83 TFs	—
<b>19. CSSI Extended Null</b>							
Null inflation	CSSI-max inflates	$\Delta$ AUROC	—	—	$\leq -0.20$	$K=2-20$	No
CSSI vs SCENIC	CSSI $\neq$ standard	Comparative	—	—	Equivalent	3 methods	—
Per-edge FDR	FDR controlled	BH-FDR	—	—	$FDR \leq 0.11$	$K=5-15$	—
<b>20. K-Sensitivity Analysis</b>							
Cont. ROC w/ N	AUROC improves	Comparison	—	—	$0.86 \rightarrow 0.93$	9 runs	—
K-sensitivity	F1 varies with $K$	Comparison	—	—	$F1 \approx 10^{-4}$ all $K$	5 $K$ values	—
<b>21. Trivial Baseline Comparison</b>							
Var vs Corr	Variance outperforms	Paired <i>t</i>	$<10^{-24}$	$<10^{-24}$	$\Delta = 0.186$	151 perts	Yes
Mean vs Corr	Mean expr outperforms	Paired <i>t</i>	$<10^{-20}$	$<10^{-20}$	$\Delta = 0.146$	151 perts	Yes
Drop vs Corr	Dropout outperforms	Paired <i>t</i>	$<10^{-12}$	$<10^{-12}$	$\Delta = 0.113$	151 perts	Yes
TF deg vs Corr	Degree underperforms	Paired <i>t</i>	$<10^{-29}$	$<10^{-29}$	$\Delta = -0.196$	151 perts	Yes
<b>22. Bootstrap Per-TF CIs</b>							
Global CI	Global AUROC robust	Bootstrap	—	—	CI=[0.71,0.72]00 iter.	—	—

Continued on next page

Table *continued*

Section	Hypothesis		Test	Raw p	BH p	Effect	N	Sig
Per-TF boot CI	Per-TF robust	AUROC	Bootstrap	–	–	CI=[0.59,0.72]00 iter.	–	–
<b>23. Attention Perturbation-First</b>								
Attn vs Corr L13	Attn = Corr on pert.	Wilcoxon	0.726	0.726	diff=0.001	n = 280	n = 280	No
Attn vs Corr L13	Attn = Corr on pert.	Paired t	0.931	0.931	diff=0.001	n = 280	n = 280	No
<b>24. Full 18-Layer Perturbation-First</b>								
L15 vs Corr	Best layer > corr	Wilcoxon	0.0009	0.003	Δ= 0.040	+ 280	n = 280	Yes
Split-sample	Discovery validates	Wilcoxon	0.017	0.035	AUROC=0.750	= 140	n = 140	Yes
Per-layer (18)	Each layer vs corr	Wilcoxon	varies	varies	AUROC 0.47–0.74	n = 280	n = 280	1/18
<b>25. Attention-Specific Confound Decomposition</b>								
Attn resid. OLS	Residual predicts	CF-AUROC	–	–	AUROC=0.538	pos.	n = 280	–
Attn resid. GBDT	Residual predicts	CF-AUROC	–	–	AUROC=0.574	pos.	n = 280	–
Corr resid. OLS	Residual predicts	CF-AUROC	–	–	AUROC=0.622	pos.	n = 280	–
Attn deg.- null	AUROC > degree	Permutation	0.023	0.046	z=2.0	200 perm.	n = 200	Yes
Corr deg.- null	AUROC > degree	Permutation	0.018	0.037	z=2.1	200 perm.	n = 200	Yes
<b>26. Conditional Incremental Value</b>								
Gene-only CV	Gene feat. predict	5-fold CV	–	–	AUROC=0.820	perts	n = 324	–
Δ gene+attn	Attn adds value	Bootstrap	–	–	–0.0004	[–0.001,0]	100 iter.	No
Δ gene+corr	Corr adds value	Bootstrap	–	–	–0.002	[–0.005,0]	100 iter.	No
TF stratified	TF vs non-TF	Subgroup	–	–	TF 0.913, non-TF 0.895	14/266	n = 324	–
<b>27. Per-Head TRRUST Ranking</b>								
Head ranking	Heads differ in reg.	AUROC range	–	–	0.34–0.75	324 heads	n = 324	–
Top-5 heads	Best heads identified	AUROC	–	–	AUROC=0.700	0.75 cells	n = 324	–

Continued on next page

Table continued

Section	Hypothesis	Test	Raw p	BH p	Effect	N	Sig
<b>28. Cross-Context CRISPRa Replication</b>							
Attn vs Corr L13	Attn $\neq$ CRISPRa	Corr	Wilcoxon	$<10^{-6}$	$<10^{-6}$	diff= -0.106	$n = 77$ Yes
Attn vs Corr L6	Attn $\neq$ CRISPRa	Corr	Wilcoxon	$10^{-6}$	$10^{-6}$	diff= -0.098	$n = 77$ Yes
Attn vs Corr L18	Attn $\neq$ CRISPRa	Corr	Wilcoxon	$<10^{-6}$	$<10^{-6}$	diff= -0.105	$n = 77$ Yes
<b>29. Head-Level Causal Ablation</b>							
Regulatory vs baseline	Ablation $\neq$ baseline	Wilcoxon	0.244	0.260	$\Delta = -0.0002$	$n = 280$	No
Random vs baseline (rep 1)	Ablation $\neq$ baseline	Wilcoxon	0.065	0.073	$\Delta = +0.0007$	$n = 280$	No
Random vs baseline (rep 2)	Ablation $\neq$ baseline	Wilcoxon	0.069	0.076	$\Delta = +0.0004$	$n = 280$	No
Random vs baseline (rep 3)	Ablation $\neq$ baseline	Wilcoxon	$<10^{-6}$	$<10^{-6}$	$\Delta = +0.0028$	$n = 280$	Yes
Entropy-matched vs baseline	Ablation $\neq$ baseline	Wilcoxon	$<10^{-6}$	$<10^{-6}$	$\Delta = +0.0042$	$n = 280$	Yes
<b>30. Nested Layer Selection Protocol</b>							
Pooled nested CV	L15 > corr (nested)	Wilcoxon	0.0009	0.003	$\Delta = 0.040$	$n = 280$	Yes
Bonferroni corr.	18-layer search	Bonferroni	0.017	–	$d=0.22$	18 layers	Yes
Bootstrap CI	Delta CI	Bootstrap	–	–	[0.018, 0.062]	1k iter.	–
Layer stability	Same layer all folds	Stability	–	–	5/5 L15	5 folds	–
<b>31. Hard-Generalization Incremental Value</b>							
Cross-pert: gene+attn vs gene	$\Delta\text{AUROC} \neq 0$	Bootstrap	–	–	$\Delta = -0.0004$	$n = -$	
					$[-0.001, 0.005]$	59,720	
Cross-pert: gene+corr vs gene	$\Delta\text{AUROC} \neq 0$	Bootstrap	–	–	$\Delta = -0.0015$	$n = -$	
					$[-0.004, 0.005]$	59,720	
Cross-gene: gene+attn vs gene	$\Delta\text{AUROC} \neq 0$	Bootstrap	–	–	$\Delta = -0.0003$	$n = -$	
					$[-0.001, 0.005]$	59,720	
Cross-gene: gene+corr vs gene	$\Delta\text{AUROC} \neq 0$	Bootstrap	–	–	$\Delta = -0.0010$	$n = -$	
					$[-0.004, 0.005]$	59,720	

Continued on next page

Table continued

Section	Hypothesis	Test	Raw p	BH p	Effect	N	Sig
Joint: gene+attn vs gene	$\Delta\text{AUROC} \neq 0$	Bootstrap	–	–	$\Delta = -0.0003, n = 559,720$	–	–
Joint: gene+corr vs gene	$\Delta\text{AUROC} \neq 0$	Bootstrap	–	–	$\Delta = -0.0011, n = 559,720$	–	–
<b>32. Expanded Causal Ablation</b>							
Reg. top-10 vs baseline	Ablation $\neq$ baseline	Wilcoxon	0.937	0.958	$\Delta = 0.0000, n = 280$ $d = 0.00$	–	No
Reg. top-20 vs baseline	Ablation $\neq$ baseline	Wilcoxon	0.596	0.664	$\Delta = +0.0003, n = 280$ $d = 0.02$	–	No
Reg. top-50 vs baseline	Ablation $\neq$ baseline	Wilcoxon	0.100	0.122	$\Delta = +0.0021, n = 280$ $d = 0.08$	–	No
Bottom-5 vs baseline	Ablation $\neq$ baseline	Wilcoxon	0.005	0.007	$\Delta = -0.0025, n = 280$ $d = -0.16$	–	Yes
Bottom-10 vs baseline	Ablation $\neq$ baseline	Wilcoxon	0.050	0.063	$\Delta = -0.0030, n = 280$ $d = -0.14$	–	No
Composite top-5 vs baseline	Ablation $\neq$ baseline	Wilcoxon	–	–	$\Delta = 0.0000, n = 280$ $d = 0.00$	–	–
Composite top-10 vs baseline	Ablation $\neq$ baseline	Wilcoxon	–	–	$\Delta = 0.0000, n = 280$ $d = 0.00$	–	–
Layer L14 all vs baseline	Ablation $\neq$ baseline	Wilcoxon	–	–	$\Delta = 0.0000, n = 280$ $d = 0.00$	–	–
Random-10 vs baseline	Ablation $\neq$ baseline	Wilcoxon	0.009	0.012	$\Delta = +0.0029, n = 280$ $d = 0.18$	–	Yes
Random-20 vs baseline	Ablation $\neq$ baseline	Wilcoxon	$<10^{-8}$	$<10^{-8}$	$\Delta = +0.0071, n = 280$ $d = 0.33$	–	Yes
Random-50 vs baseline	Ablation $\neq$ baseline	Wilcoxon	0.351	0.406	$\Delta = +0.0002, n = 280$ $d = 0.01$	–	No
<b>33. Cross-Context T-Cell CRISPRi Replication</b>							
Attn vs Corr L6	Attn $\neq$ Corr T-cell	Wilcoxon	1.000	1.000	diff = $+0.016,$ $d = 0.08$	$n = 7$	No
Attn vs Corr L13	Attn $\neq$ Corr T-cell	Wilcoxon	0.938	0.958	diff = $-0.003,$ $d = -0.01$	$n = 7$	No

Continued on next page

Table continued

Section	Hypothesis	Test	Raw p	BH p	Effect	N	Sig
Attn vs Corr L15	Attn $\neq$ Corr T-cell	Wilcoxon	0.813	0.849	diff= +0.029, $d=0.16$	$n = 7$	No
Attn vs Corr L18	Attn $\neq$ Corr T-cell	Wilcoxon	0.938	0.958	diff= +0.030, $d=0.18$	$n = 7$	No

### 34. Orthogonal Causal Interventions

Unif. attn reg. top-5 vs baseline	Intervention baseline	$\neq$	Wilcoxon	0.004	0.006	$\Delta=-0.0004, n=280$	$d=-0.17$	= Yes
Unif. attn reg. top-10 vs baseline	Intervention baseline	$\neq$	Wilcoxon	0.052	0.065	$\Delta=+0.0002, n=280$	$d=0.07$	= No
Unif. attn random-10 vs baseline	Intervention baseline	$\neq$	Wilcoxon	$<10^{-3}$	0.001	$\Delta=-0.0032, n=280$	$d=-0.20$	= Yes
MLP zero L15 vs baseline	Intervention baseline	$\neq$	—	—	—	$\Delta=0.0000, n=280$	$d=0.00$	= —
MLP zero L13–L15 vs baseline	Intervention baseline	$\neq$	—	—	—	$\Delta=0.0000, n=280$	$d=0.00$	= —
MLP zero L8 (random) vs baseline	Intervention baseline	$\neq$	Wilcoxon	$<10^{-4}$	$<10^{-4}$	$\Delta=-0.0053, n=280$	$d=-0.27$	= Yes

### 35. Propensity-Matched Perturbation Benchmark

Raw attn AUROC (matched)	Attn > chance	—	—	—	AUROC=0.609±0.121	$n=280$	= —
Raw corr AUROC (matched)	Corr > chance	—	—	—	AUROC=0.574±0.169	$n=280$	= —
Gene+attn vs gene-only (matched)	Attn adds value	Bootstrap	—	—	$\Delta\text{AUROC}=-0.0008$ [−0.000, +0.000]	(null)	No
Gene+corr vs gene-only (matched)	Corr adds value	Bootstrap	—	—	$\Delta\text{AUROC}=-0.0008$ [−0.001, +0.001]	(null)	No
Gene+attn vs gene-only	Attn adds AUPRC	Bootstrap	—	—	$\Delta\text{AUPRC}=-0.0005$ [+0.000, +0.002]	Marginal	
TRRUST attn	Attn > chance (direct-target)	—	—	—	AUROC=0.695±0.105	6 TFs	= —

Continued on next page

Table continued

Section	Hypothesis		Test	Raw p	BH p	Effect	N	Sig
<b>36. Intervention-Fidelity Diagnostics</b>								
Unif. top-5 shift	attn hidden	Intervention turbs hidden	per-	Cosine dist	–	–	max cos=0.057, logit cos=0.005	$n = 2000$
Unif. top-10 shift	attn hid-	Intervention turbs hidden	per-	Cosine dist	–	–	max cos=0.085, logit cos=0.021	$n = 2000$
Unif. random-10 shift	attn hidden	Random perturbs	Cosine dist	–	–	max cos=0.042, logit cos=0.001	$n = 2000$	Material
MLP L15 shift	zero hidden	Intervention turbs hidden	per-	Cosine dist	–	–	max cos=0.043, logit cos=0.003	$n = 2000$
MLP L13–L15 shift	zero hidden	Intervention turbs hidden	per-	Cosine dist	–	–	max cos=0.190, logit cos=0.012	$n = 2000$
MLP random L8 shift	zero hidden	Random perturbs	Cosine dist	–	–	max cos=0.023, logit cos=0.001	$n = 2000$	Material
<b>37. Non-K562 Perturbation-First Replication</b>								
RPE1 attn vs corr	L6	Attn $\neq$ Corr RPE1	Wilcoxon	$<10^{-10}$	$<10^{-8}$	diff= +0.118, $d=0.74$	$n = 1167$	Yes
RPE1 attn vs corr	L13	Attn $\neq$ Corr RPE1	Wilcoxon	$<10^{-10}$	$<10^{-8}$	diff= +0.036, $d=0.20$	$n = 1167$	Yes
RPE1 attn vs corr	L15	Attn $\neq$ Corr RPE1	Wilcoxon	$<10^{-10}$	$<10^{-8}$	diff= +0.090, $d=0.47$	$n = 1167$	Yes
RPE1 attn vs corr	L18	Attn $\neq$ Corr RPE1	Wilcoxon	$<10^{-10}$	$<10^{-8}$	diff= +0.086, $d=0.48$	$n = 1167$	Yes
iPSC neuron L15 corr	Attn $\neq$ Corr neuron	Wilcoxon	0.078	0.083	diff= +0.058, $d=0.80$	$n = 7$	No	

### 16.3 Claim-to-evidence mapping

Table S11: **Headline claim-to-evidence mapping.**

Headline Claim	Supporting Analysis	Key Test(s)	BH Sig
Top- $K$ scaling degradation	Scaling	Sign test (TR-RUST)	Yes
Continuous AUROC improves	K-Sensitivity	Comparative	Descr.
Mediation non-additivity	Mediation Bias	Lower bound	Yes
Detectability theory validated	Detectability	Correlation $r=0.887$	Yes
Perturbation-first AUROC > 0.5	Pert.-first	$t$ -test, all 27 cond.	Yes
Attn $\approx$ Corr on CRISPRi	Attn pert.-first	Wilcoxon $p=0.73$	No (null)
L15 best layer ( $\Delta=+0.04$ )	18-layer, Nested CV	Wilcoxon, Bonf. $p=0.017$	Yes
L15 effect is small ( $d=0.22$ )	Nested Layer	Cohen's $d$ , bootstrap CI	Yes
No incremental pairwise value	Incr. value	Bootstrap $\Delta$ AUROC $\leq 0$	Descr.
Trivial baselines outperform	Trivial baselines	Paired $t$ , all $p < 10^{-12}$	Yes
CRISPRa: attn < corr	CRISPRa repl.	Wilcoxon $p < 10^{-6}$	Yes
T-cell: attn $\approx$ corr	T-cell repl.	Wilcoxon $p > 0.8$	No (null)
Ablation null (reg. heads)	Ablation	Wilcoxon $p > 0.05$	No (null)
Orthogonal interventions null	Uniform attn + MLP	All $ \Delta  < 0.005$	No (null)
Propensity-matched null	Matched benchmark	$\Delta$ AUROC $\in [-0.000, +0.000]$	No (null)
Interventions perturb repr.	Fidelity diagnostics	All max cos $> 0.02$	Descr.
RPE1: attn > corr ( $d=0.47$ )	Non-K562 repl.	Wilcoxon $p < 10^{-10}$	Yes
Random ablation causes drop	Expanded ablation	Wilcoxon $p < 10^{-8}$	Yes
Heterogeneity improves corr	Controlled comp.	Spearman $\rho=+0.63$	Yes
Edge-expression correlation	Residualization	Spearman $\rho=0.84$	Yes
Cross-species conservation	Ortholog transfer	$\rho=0.743$	Yes

## 16.4 Summary statistics

- **Total statistical tests:** 153 across 37 complementary analyses (95 confirmatory with p-values, 58 descriptive)

- **Significant after BH-FDR correction:** 63 of 95 confirmatory tests (66%)
- **Framework-level  $\alpha$ :** 0.05 with Benjamini-Hochberg correction
- **Most robust findings:** Top- $K$  scaling degradation (unanimous across runs), cross-species conservation ( $\rho = 0.743$ ,  $p < 10^{-300}$ ), CSSI synthetic validation ( $p = 2.4 \times 10^{-8}$ ), heterogeneity-AUROC correlation ( $\rho = +0.63$ ,  $p = 10^{-4}$ ), edge-expression correlation ( $\rho = 0.842$ ,  $p < 10^{-50}$ ), degree-preserving null ( $z = 3.63$ ,  $p < 0.005$ ), perturbation sensitivity (all 27 conditions  $p < 0.005$ ), RPE1 attention advantage ( $d = 0.47$ , adjusted  $p < 10^{-8}$ )
- **Key null findings:** Pseudotime directionality (adj.  $p = 0.124$ ), perturbation validation (Reprole CRISPRi baseline AUROC = 0.511,  $p = 0.32$ ; primary AUROC = 0.696,  $p < 10^{-4}$ ; all 27 sensitivity conditions AUROC = 0.62–0.76, all  $p < 0.005$ ), real-data CSSI improvement (adj.  $p = 0.053$ ), attention  $\approx$  correlation in K562 CRISPRi ( $p = 0.73$ ), no incremental pairwise value ( $\Delta$ AUROC  $\leq 0.002$ )

**Notes:**

1. All p-values reflect framework-level Benjamini-Hochberg FDR correction across 95 confirmatory tests (153 total across 37 analyses) unless explicitly noted as raw values for methodological transparency.
2. Effect sizes include Cohen's  $d$ , correlation coefficients ( $\rho$ ), fold-changes, AUROC values, and percentage improvements as appropriate.
3. Sample sizes vary by analysis: from individual run-pairs (mediation bias) to tens of thousands of cells (cross-species transfer) to bootstrap resamples (uncertainty quantification).
4. “—” indicates not applicable or not reported in original analysis.
5. A machine-readable version of the full registry (CSV format, one row per test) is provided in the supplementary materials.

## Supplementary Methods

The following methodological details supplement the condensed Methods section in the main text.

### Mediation bias analysis

We formalize the bias problem in activation patching following the causal mediation framework of Pearl [2001] and Imai et al. [2010]. Analysis was performed on a frozen cross-tissue mediation archive (6 runs across immune, kidney, and lung tissues from Tabula Sapiens, with head and MLP granularities, 16 run-pairs total) derived from scGPT attention patching experiments.

### Detectability theory

Two signal classes are compared: *attention-like* signals derived from raw attention weight aggregation, and *intervention-like* signals obtained through activation patching. Phase diagrams were constructed by systematically varying signal-to-noise ratios and tail inflation factors across biologically realistic parameter ranges.

### Cross-context consistency analysis

Cross-tissue consistency was assessed using invariant causal discovery principles [Peters et al., 2016] applied to matched TF-target panels across immune, kidney, and lung tissues from Tabula Sapiens. Bootstrap uncertainty intervals (10,000 resamples) and permutation-based significance testing (5,000 permutations) were used.

### Cross-species ortholog transfer analysis

We performed a systematic stress test of correlation-based TF-target edge transfer between human lung (Tabula Sapiens, 65,847 cells) and mouse lung (Krasnow Smart-seq2, 9,409 cells) [Travaglini et al., 2020]. Using 53,482 one-to-one orthologs and 61 shared transcription factors, we computed Spearman correlation-based edge scores independently in each species. Human data were subsampled to 10,000 cells. Edges with  $|\rho| < 0.05$  were discarded, yielding 25,876 matched edges.

### Pseudotime directionality audit

We audited 56 well-characterized TF-target regulatory pairs spanning three immune lineages in the Tabula Sapiens immune subset (20,000 cells). Diffusion pseudotime [Haghverdi et al., 2016] was computed per lineage using 2,000 HVGs, 30 PCA components, and  $k = 15$  nearest neighbors.

### Batch and donor leakage audit

TF-target edge scores were computed as Pearson correlations for  $\sim 8,000$  TF-target pairs per tissue. An Artifact Sensitivity Index (ASI) was defined as  $ASI = |r_{full} - r_{balanced}| / \max(|r_{full}|, 0.01)$ . Edges with  $ASI > 0.5$  were flagged.

### Uncertainty calibration of edge scores

We evaluated the calibration of six edge-scoring methods against Perturb-seq ground truth from CRISPRi experiments. Post-hoc calibration used Platt scaling [Platt, 1999] and isotonic regression [Niculescu-Mizil and Caruana, 2005]. Split conformal prediction sets [Vovk et al., 2005] were constructed with finite-sample coverage guarantees.

### Synthetic ground-truth validation

Ground-truth networks had sparse connectivity ( $\rho = 0.15$ ) with hierarchical TF-regulator-target structure. Synthetic attention matrices were generated as  $A_{attention} = \tanh(A_{true} + \epsilon_{structured} + \epsilon_{expression-bias})$ .

## Multi-model validation

We tested scVI [Lopez et al., 2018] (latent-distance edges) and C2S-Pythia (405M-parameter causal LM), which showed qualitatively similar near-random GRN recovery (AUROC 0.48–0.53). Full results are reported in Supplementary Note 13.

## Attention residualization on expression covariates

To avoid overfitting, we used cross-fitted residualization (5-fold). We tested robustness across: multiple covariate sets, OLS vs. GBDT residualizers, signed vs. absolute correlation, and 10 random seeds.

## Degree-preserving null models

We implemented two null models: (i) label-shuffling null ( $n = 1,000$  permutations) and (ii) degree-preserving null ( $n = 200$  permutations) using the curveball algorithm [Strona et al., 2014].

## Attention–correlation mapping

Cross-tissue analysis matched Geneformer attention edges (DLPFC brain) against Spearman correlations (Tabula Sapiens immune, 20,000 cells).

## Supplementary Note 17 Biological Characterization of Attention Patterns

To characterize what biological relationships attention patterns encode beyond co-expression, we evaluated Geneformer V2-316M attention edges (2,000 K562 control cells, 2,000 HVGs) against six reference databases: TRRUST (transcriptional regulation; 175 pairs in HVG), STRING  $\geq 700$  (protein–protein interactions; 2,747 pairs), STRING  $\geq 900$  (high-confidence PPI; 1,675 pairs), Reactome (pathway co-membership; 238,640 pairs), KEGG (pathway co-membership; 24,812 pairs), and GO Biological Process (functional co-annotation; 135,596 pairs). For each database, we computed AUROC of attention edges at all 18 layers against the reference edge set, and compared to Spearman correlation edges.

### Layer-specific biological specialization

Attention patterns show clear layer-specific specialization. Protein–protein interaction signal peaks at the earliest layer (STRING  $\geq 700$ : AUROC = 0.640 at L0) and decreases monotonically with depth (Spearman  $\rho = -0.608$ ,  $p_{\text{raw}} = 0.0075$ ,  $q_{\text{BH}} = 0.011$ ). STRING  $\geq 900$  shows the same pattern ( $\rho = -0.581$ ,  $q_{\text{BH}} = 0.014$ ). Conversely, transcriptional regulatory signal (TRRUST) increases with depth ( $\rho = +0.511$ ,  $q_{\text{BH}} = 0.030$ ), peaking at L15 (AUROC = 0.750). Functional co-annotation signals (KEGG:  $\rho = +0.831$ ,  $q_{\text{BH}} < 10^{-4}$ ; GO BP:  $\rho = +0.846$ ,  $q_{\text{BH}} < 10^{-4}$ ) and Reactome ( $\rho = +0.731$ ,  $q_{\text{BH}} = 0.001$ ) also increase with depth but with weaker absolute signal (AUROC 0.52–0.56 at best layers). All six Spearman trend tests survive Benjamini-Hochberg correction at  $\alpha = 0.05$ .

The cross-layer profiles for PPI and regulation are anti-correlated: STRING  $\geq 900$  vs. TRRUST  $\rho = -0.546$  ( $p = 0.019$ ); STRING  $\geq 700$  vs. TRRUST  $\rho = -0.445$  ( $p = 0.064$ , marginal). Meanwhile, KEGG, GO BP, and Reactome profiles are strongly positively correlated with each other ( $\rho = 0.75$ –0.89, all  $p < 0.001$ ) and with TRRUST ( $\rho = 0.35$ –0.45, marginal), forming a coherent “functional/regulatory” cluster distinct from the PPI signal.

Table S12: AUROC of Geneformer attention edges against six biological reference databases across all 18 layers. Correlation baseline shown in last row.

Layer	STRING $_{\geq 700}$	STRING $_{\geq 900}$	TRRUST	Reactome	KEGG	GO BP
L0	<b>0.640</b>	<b>0.644</b>	0.558	0.505	0.530	0.526
L1	0.517	0.501	0.691	0.501	0.484	0.501
L4	0.546	0.530	0.686	0.516	0.525	0.515
L8	0.530	0.519	0.631	0.509	0.531	0.534
L13	0.574	0.559	0.708	0.523	0.548	0.530
L15	0.525	0.500	<b>0.750</b>	0.521	0.555	0.541
L16	0.475	0.457	0.733	0.516	<b>0.564</b>	<b>0.544</b>
L17	0.485	0.460	0.664	0.516	0.539	0.541
Corr.	0.562	0.559	0.649	0.514	0.541	0.513

### Partial correlation controlling for expression similarity

To test whether attention captures biological structure beyond expression similarity, we computed partial correlations controlling for Spearman expression correlation (using matched positive and negative reference pairs). TRRUST signal is robust: 97% of the attention–membership correlation is retained after controlling for expression (partial  $r = 0.353$ ,  $p = 1.1 \times 10^{-11}$ ; raw  $r = 0.363$ ). GO BP retains 89% and KEGG retains 72%. Reactome signal, however, is non-significant after expression control (partial  $r = 0.015$ ,  $p = 0.12$ ), confirming Reactome pathway co-membership as a null result.

## Top-edge enrichment analysis

Fisher's exact tests for overlap between the top-1,000 highest-attention edges and each reference database (TRRUST excluded due to 0.009% base rate yielding 0 overlap at all layers). After BH correction across 30 tests (5 layers  $\times$  3 databases  $\times$  2 tails):

- **L0 (early, PPI-related):** Significant enrichment for KEGG (OR = 3.38,  $q < 10^{-10}$ ), GO BP (OR = 1.47,  $q = 0.001$ ), and Reactome (OR = 1.25,  $q = 0.028$ ).
- **L17 (late, regulation-related):** Strongest enrichment across all databases: Reactome (OR = 1.99,  $q < 10^{-16}$ ), KEGG (OR = 3.71,  $q < 10^{-12}$ ), GO BP (OR = 2.12,  $q < 10^{-13}$ ).
- **L10 (mid-depth):** No significant enrichment for any database (all OR  $\approx 1.0$ ).

The concentration of enrichment at the periphery (L0 and L17) with a dead zone at mid-depth supports the layer-specialization interpretation.

## Interpretation

Attention patterns in Geneformer capture a hierarchy of biological signals with layer-specific organization: the input layer (L0) preferentially encodes physical protein–protein interactions, while deeper layers progressively encode transcriptional regulation and functional co-annotation. This hierarchy is real—it survives pairwise expression control (97% of TRRUST signal retained) and is statistically robust across all six databases. However, acknowledging this hierarchy does not contradict the main finding that attention provides no incremental value over gene-level features for perturbation prediction (main text, Section 2.3). The key distinction is between the confound controls: the partial correlations here remove pairwise expression similarity, whereas the incremental-value analysis in the main text controls for gene-level features (variance, mean expression, dropout rate). Gene-level features, not pairwise co-expression, are the dominant confound. Thus, the title's claim—that attention captures co-expression rather than causal regulation—is more precisely stated as: attention captures biologically structured signals, including regulatory ones, but these signals are entirely redundant with gene-level features and provide no unique information for predicting the functional consequences of genetic perturbations.

## Supplementary Note 18 Value-Weighted Edge Extraction

The main paper shows that ablating TRRUST-ranked attention heads has no effect on perturbation prediction, while ablating random heads does ( $d = 0.33$ ,  $p < 10^{-8}$ ). This suggests that perturbation-predictive computation resides in the value/FFN pathway rather than in the attention pattern itself. We tested whether *value-weighted* edge scores—computed from the context layer  $\text{softmax}(QK^\top/\sqrt{d}) \cdot V$  rather than the raw attention pattern  $\text{softmax}(QK^\top/\sqrt{d})$ —better capture regulatory structure.

### Methods

Using forward hooks on each `BertSelfAttention` module in Geneformer V2-316M, we extracted the context layer  $A_{vh} = \text{softmax}(QK^\top/\sqrt{d}) \cdot V$  (shape:  $n_{\text{genes}} \times d_{\text{head}}$ ) for each layer and head across 2,000 K562 control cells. Pairwise edge scores were computed as cosine similarity between gene representations:  $\text{edge}(i, j) = \cos(A_{vh}[i, :], A_{vh}[j, :])$ , averaged across heads within each layer. We also tested centroid cosine similarity (computing similarity on the mean context vector across cells rather than averaging per-cell similarities) and dot product. A total of 1,941 genes (of 2,000 HVGs) were in the Geneformer vocabulary; 269 of 280 perturbations were evaluable.

### Results

Value-weighted cosine similarity significantly *underperforms* both raw attention and Spearman correlation at every layer:

Table S13: Edge score comparison: value-weighted vs. raw attention.

Metric	Best VW Cosine	Best Raw Attn	Correlation	Variance
Pert-first AUROC	0.587 (L12)	0.787 (L14)	0.706	0.887
TRRUST AUROC	0.606 (L12)	0.718 (L15)	0.638	—

Paired Wilcoxon tests ( $n = 269$  perturbations): VW cosine vs. raw attention  $\Delta = -0.200$ ,  $p = 4.9 \times 10^{-39}$ ,  $d = -1.68$ ; VW cosine vs. correlation  $\Delta = -0.120$ ,  $p = 2.4 \times 10^{-14}$ ,  $d = -1.00$ . Centroid cosine and dot product variants also underperform raw attention (best TRRUST AUROC: centroid = 0.623 at L5, dot = 0.589 at L14).

In the incremental-value test (5-fold GroupKFold logistic regression), adding VW cosine to gene-level features slightly *hurts* performance ( $\Delta\text{AUROC} = -0.009$ ; gene-only = 0.865, gene + VW = 0.856). VW edges alone achieve AUROC = 0.587, well below both raw attention (0.707) and correlation (0.637).

### Interpretation

The context layer  $\text{softmax}(QK^\top/\sqrt{d}) \cdot V$  mixes information from all attended genes, collapsing the pairwise structure that even raw attention preserves. Cosine similarity between context vectors measures whether two genes receive similar blends of information from the attention mechanism—“information-receipt similarity”—which is a fundamentally different quantity from direct gene-to-gene attention coupling. This negative result, combined with the ablation finding that random heads are more causally important than regulatory heads, indicates that perturbation-predictive computation is distributed across the network in a form not recoverable from any simple attention-derived edge score—neither the attention pattern nor the value-weighted context.

## Supplementary Note 19 Per-TF Characterization (Exploratory)

We examined whether the per-TF AUROC for attention-derived edge scores varies systematically with TF biology. Among 18 evaluable TFs in the Tabula Sapiens immune dataset, manually annotated master regulators ( $n = 9$ : GATA1, PPARG, WT1, NKX2-5, FOXA1, KLF1, PAX3, TAL1, LEF1) had higher mean AUROC ( $0.80 \pm 0.18$ ) than other TF categories (signal-dependent, lineage-specific, housekeeping;  $n = 9$ :  $0.58 \pm 0.18$ ; permutation  $p = 0.011$ , 10,000 label shuffles). However, this comparison did not survive Benjamini-Hochberg correction across all 11 tests performed ( $q = 0.12$ ).

**Severe power limitation.** 13 of 18 TFs had only a single evaluable TRRUST target in the HVG set, meaning their AUROC reflects the rank of one gene among  $\sim 2,000$  rather than a regulon-level assessment. When restricted to the 5 TFs with  $\geq 3$  evaluable targets (GATA1, PPARG, EGR1, WT1, FOXF2), the master regulator advantage was not significant (permutation  $p = 0.30$ ).

Table S14: **Per-TF AUROC and characterization.** 18 evaluable TFs.

TF	Category	Targets in HVG	AUROC	Successful
LEF1	master regulator	1	0.997	Yes
KLF1	master regulator	1	0.995	Yes
PPARG	master regulator	10	0.900	Yes
FOXA1	master regulator	2	0.874	Yes
MAL	signal-dependent	1	0.860	Yes
EGR1	signal-dependent	9	0.852	Yes
GATA1	master regulator	18	0.842	Yes
PAX3	master regulator	1	0.802	—
WT1	master regulator	5	0.675	No
KLF3	lineage-specific	1	0.644	No
YBX1	housekeeping	1	0.640	No
PA2G4	housekeeping	1	0.630	No
NKX2-5	master regulator	2	0.572	No
TAL1	master regulator	1	0.556	No
FOXF2	lineage-specific	3	0.500	No
TBX5	lineage-specific	1	0.401	No
RXRA	signal-dependent	2	0.359	No
NCOA4	signal-dependent	1	0.349	No

No tested TF property—including mean expression ( $\rho = -0.14$ ,  $q = 0.66$ ), expression variance ( $\rho = -0.20$ ,  $q = 0.58$ ), nonzero fraction ( $\rho = -0.01$ ,  $q = 0.97$ ), or full regulon size ( $\rho = 0.26$ ,  $q = 0.53$ )—significantly predicted AUROC after BH correction. The evaluable regulon size showed the strongest raw trend ( $\rho = -0.46$ ,  $p = 0.06$ ,  $q = 0.33$ ), suggesting that TFs with more evaluable targets tend to have AUROC closer to 0.5, consistent with regulon-level AUROC being a harder test than single-gene rank.

We treat the master regulator association as hypothesis-generating: the pattern is consistent with attention more reliably capturing regulatory relationships for master regulators with large, well-characterised regulons, but the small sample ( $n = 18$ ) and severe single-target problem preclude definitive conclusions. Larger TF databases with greater regulon coverage (e.g., DoRothEA, ChIP-Atlas) would be needed to test this rigorously.

## References

Haotian Cui, Chloe Wang, Hassaan Maan, Kuan Pang, Fengning Luo, and Bo Wang. scGPT: toward building a foundation model for single-cell multi-omics using generative AI. *Nature Methods*, 21(8):1470–1479, 2024.

Christina V Theodoris, Ling Xiao, Anant Chopra, Mark D Chaffin, Zeina R Al Sayed, Matthew C Hill,

Helene Mantineo, Elizabeth M Brydon, Zexian Zeng, X Shirley Liu, et al. Transfer learning enables predictions in network biology. *Nature*, 618(7965):616–624, 2023.

Fan Yang, Wei Wang, Fang Wang, Yuan Fang, Duyu Tang, Junzhou Huang, Hui Lu, and Jianhua Yao. scBERT as a large-scale pretrained deep language model for cell type annotation of single-cell RNA-seq data. *Nature Machine Intelligence*, 4(10):852–866, 2022.

Minsheng Hao, Jing Gong, Xin Zeng, Chiming Liu, Yixuan Guo, Xingyi Cheng, Taifeng Xu, Le Song, and Xuegong Zhang. Large-scale foundation model on single-cell transcriptomics. *Nature Methods*, 21(8):1481–1491, 2024.

Yiqun Chen, Kaushik Bhatt, et al. GenePT: a simple but effective foundation model for genes and cells built from ChatGPT. *bioRxiv*, 2024. doi: 10.1101/2023.10.16.562533.

Yanay Rosen, Yusuf Roohani, Ayush Agrawal, Leon Samotorcan, Tabula Sapiens Consortium, Stephen R Quake, and Jure Leskovec. Universal cell embeddings: a foundation model for cell biology. *bioRxiv*, 2024. doi: 10.1101/2023.11.28.568918.

Rui Zheng, Songqin Gao, et al. Benchmarking computational methods for single-cell gene regulatory network reconstruction from multimodal data. *Nature Methods*, 2024. doi: 10.1038/s41592-024-02410-x.

Kevin Meng, David Bau, Alex Andonian, and Yonatan Belinkov. Locating and editing factual associations in GPT. *Advances in Neural Information Processing Systems*, 35:17359–17372, 2022.

Nicholas Goldowsky-Dill, Chris MacLeod, Lucas Sato, and Aryaman Arora. Localizing model behavior with path patching. *arXiv preprint arXiv:2304.05969*, 2023.

Arthur Conmy, Augustine N Mavor-Parker, Aengus Lynch, Stefan Heimersheim, and Adrià Garriga-Alonso. Towards automated circuit discovery for mechanistic interpretability. *Advances in Neural Information Processing Systems*, 36, 2023.

Nelson Elhage, Neel Nanda, Catherine Olsson, Tom Henighan, Nicholas Joseph, Ben Mann, Amanda Askell, Yuntao Bai, Anna Chen, Tom Conerly, et al. A mathematical framework for transformer circuits. *Transformer Circuits Thread*, 2021.

Catherine Olsson, Nelson Elhage, Neel Nanda, Nicholas Joseph, Nova DasSarma, Tom Henighan, Ben Mann, Amanda Askell, Yuntao Bai, Anna Chen, et al. In-context learning and induction heads. *arXiv preprint arXiv:2209.11895*, 2022.

Kevin Wang, Alexandre Variengien, Arthur Conmy, Buck Shlegeris, and Jacob Steinhardt. Interpretability in the wild: a circuit for indirect object identification in GPT-2 small. *arXiv preprint arXiv:2211.00593*, 2022.

Heonjong Han, Jung-Woong Cho, Sangyoung Lee, Ayoung Yun, Hyojin Kim, Dasom Bae, Sunmo Yang, Chan Yeong Kim, Muyoung Lee, Eunbeen Kim, et al. TRRUST v2: an expanded reference database of human and mouse transcriptional regulatory interactions. *Nucleic Acids Research*, 46(D1):D380–D386, 2018.

Luz Garcia-Alonso, Christian H Holland, Mahmoud M Ibrahim, Denes Turei, and Julio Saez-Rodriguez. Benchmark and integration of resources for the estimation of human transcription factor activities. *Genome Research*, 29(8):1363–1375, 2019.

Aditya Pratapa, Amogh P Jalihal, Jeffrey N Law, Aditya Bharadwaj, and T M Murali. Benchmarking algorithms for gene regulatory network inference from single-cell transcriptomic data. *Nature Methods*, 17(2):147–154, 2020.

Sarthak Jain and Byron C Wallace. Attention is not explanation. *arXiv preprint arXiv:1902.10186*, 2019.

Sofia Serrano and Noah A Smith. Is attention interpretable? *arXiv preprint arXiv:1906.03731*, 2019.

Adrien Bibal, Rémi Cardon, Thomas Demeester, et al. Is attention explanation? An introduction to the debate. *arXiv preprint arXiv:2204.12710*, 2022.

Atray Dixit, Oren Parnas, Biyu Li, Jenny Chen, Charles P Fulco, Leander Jerber, Alla Laptenko, Joseph D Phelan, Rishi Jain, Ethan B Krall, et al. Perturb-seq: dissecting molecular circuits with scalable single-cell RNA profiling of pooled genetic screens. *Cell*, 167(7):1853–1866, 2016.

Joseph M Replogle, Reuben A Saunders, Angela N Pogson, Jeffrey A Hussmann, Alexander Lenail, Alina Guna, Lauren Mascibroda, Eric J Wagner, Karen Adelman, Jennifer A Doudna, and Jonathan S Weissman. Mapping information-rich genotype-phenotype landscapes with genome-scale Perturb-seq. *Cell*, 185(14):2559–2575, 2022.

Elena Voita, David Talbot, Fedor Moiseev, Rico Sennrich, and Ivan Titov. Analyzing multi-head self-attention: Specialized heads do the heavy lifting, the rest can be pruned. In *Proceedings of the 57th Annual Meeting of the Association for Computational Linguistics*, pages 5797–5808, 2019.

Kevin Clark, Urvashi Khandelwal, Omer Levy, and Christopher D Manning. What does BERT look at? An analysis of BERT’s attention. In *Proceedings of the 2019 ACL Workshop BlackboxNLP*, pages 276–286, 2019.

Britt Adamson, Thomas M Norman, Marco Jost, Min Y Cho, James K Nuñez, Yuwen Chen, Jacqueline E Villalta, Luke A Gilbert, Max A Horlbeck, Marco Y Hein, et al. A multiplexed single-cell CRISPR screening platform enables systematic dissection of the unfolded protein response. *Cell*, 167(7):1867–1882, 2016.

Eric Shifrut, Julia Carnevale, Victoria Tober, Ron A Greenstein, Molly Deitch, Jeanette Haliburton, Nichelle Graham, D Ray, Helena M Berns, and Alexander Marson. Genome-wide CRISPR screens in primary human T cells reveal key regulators of immune function. *Cell*, 175(7):1958–1971, 2018.

Sarah Wiegrefe and Yuval Pinter. Attention is not explanation. *arXiv preprint arXiv:1908.04626*, 2019.

Damian Szkłarczyk, Annika L Gable, Katerina C Nastou, David Lyon, Rebecca Kirsch, Sampo Pyysalo, Nadezhda T Doncheva, Marc Legeay, Tao Fang, Peer Bork, et al. The STRING database in 2021: customizable protein–protein networks, and functional characterization of user-uploaded gene/measurement sets. *Nucleic Acids Research*, 49(D1):D483–D489, 2021.

Vladimir Vovk, Alexander Gammerman, and Glenn Shafer. *Algorithmic Learning in a Random World*. Springer, 2005.

The Tabula Sapiens Consortium. The Tabula Sapiens: a multiple-organ, single-cell transcriptomic atlas of humans. *Science*, 376(6594):eabl4896, 2022.

Kristen R Maynard, Leonardo Collado-Torres, Lukas M Weber, Cedric Uytingco, Brianna K Barry, Stephen R Williams, Joseph L Catallini II, Matthew N Tran, Zachary Besich, Maddy Tippani, et al. Transcriptome-scale spatial gene expression in the human dorsolateral prefrontal cortex. *Nature Neuroscience*, 24(3):425–436, 2021.

F Alexander Wolf, Philipp Angerer, and Fabian J Theis. SCANPY: large-scale single-cell gene expression data analysis. *Genome Biology*, 19:15, 2018.

Yoav Benjamini and Yosef Hochberg. Controlling the false discovery rate: a practical and powerful approach to multiple testing. *Journal of the Royal Statistical Society: Series B*, 57(1):289–300, 1995.

Vân Anh Huynh-Thu, Alexandre Irrthum, Louis Wehenkel, and Pierre Geurts. Inferring regulatory networks from expression data using tree-based methods. *PloS One*, 5(9):e12776, 2010.

Thomas Moerman, Sara Aibar Santos, Carmen Bravo Gonzalez-Blas, Jaak Simm, Yves Moreau, Jan Aerts, and Stein Aerts. GRNBoost2 and Arboreto: efficient and scalable inference of gene regulatory networks. *Bioinformatics*, 35(12):2159–2161, 2019.

Jesse Vig, Sebastian Gehrmann, Yonatan Belinkov, Sharon Qian, Daniel Nishi, Raquel Alhama, Stuart Shieber, Ali Sucak, and Elena Voita. Investigating gender bias in language models using causal mediation analysis. *Advances in Neural Information Processing Systems*, 33:12388–12401, 2020.

Judea Pearl. Direct and indirect effects. In *Proceedings of the Seventeenth Conference on Uncertainty in Artificial Intelligence*, pages 411–420, 2001.

Kosuke Imai, Luke Keele, and Dustin Tingley. A general approach to causal mediation analysis. *Psychological Methods*, 15(4):309–334, 2010.

Lloyd S Shapley. A value for n-person games. *Contributions to the Theory of Games*, 2(28):307–317, 1953.

Scott M Lundberg and Su-In Lee. A unified approach to interpreting model predictions. *Advances in Neural Information Processing Systems*, 30, 2017.

David Donoho and Jiashun Jin. Higher criticism for detecting sparse heterogeneous mixtures. *Annals of Statistics*, 32(3):962–994, 2004.

Peter J Huber. *Robust estimation of a location parameter*. Stanford University, 1964.

Kyle J Travaglini, Ahmad N Nabhan, Lolita Penland, Rahul Sinha, Astrid Gillich, Rene V Sit, Stephen Chang, Stephanie D Conley, Yasuo Mori, Jun Seita, et al. A molecular cell atlas of the human lung from single-cell RNA sequencing. *Nature*, 587:619–625, 2020.

Laleh Haghverdi, Maren Büttner, F Alexander Wolf, Florian Buettner, and Fabian J Theis. Diffusion pseudotime robustly reconstructs lineage branching. *Nature Methods*, 13:845–848, 2016.

Jonas Peters, Peter Bühlmann, and Nicolai Meinshausen. Causal inference by using invariant prediction: identification and confidence intervals. *Journal of the Royal Statistical Society: Series B*, 78(5):947–1012, 2016.

John C Platt. Probabilistic outputs for support vector machines and comparisons to regularized likelihood methods. *Advances in Large Margin Classifiers*, pages 61–74, 1999.

Alexandru Niculescu-Mizil and Rich Caruana. Predicting good probabilities with supervised learning. In *ICML*, pages 625–632, 2005.

Romain Lopez, Jeffrey Regier, Michael B Cole, Michael I Jordan, and Nir Yosef. Deep generative modeling for single-cell transcriptomics. *Nature Methods*, 15(12):1053–1058, 2018.

Giovanni Strona, Domenico Nappo, Francesco Boccacci, Simone Fattorini, and Jesús San-Miguel-Ayanz. A fast and unbiased procedure to randomize ecological binary matrices with fixed row and column totals. *Nature Communications*, 5(1):4114, 2014.